Syracuse University

SURFACE

May 2016

MULTILAYER COMPOSITE SOLID ELECTROLYTES FOR LITHIUM ION BATTERIES

Wei Liu
Syracuse University

Follow this and additional works at: https://surface.syr.edu/etd

Part of the Engineering Commons

Recommended Citation

Abstract

MULTILAYER COMPOSITE SOLID ELECTROLYTES FOR LITHIUM ION BATTERIES

By

Wei Liu

Lithium ion batteries (LIBs) are becoming the standard energy storage option for an increasingly diverse range of applications from mobile phones to cars. The conventional liquid electrolytes based LIBs are prone to failure in conditions such as high operating temperature, solvent leakage, lithium dendrites formation and thermal runaway, etc. All-solid-state lithium ion batteries (ASSLIBs) provide a promising power strategy to overcome the drawbacks of liquid electrolyte by substituting the highly flammable organic liquid electrolyte with solid electrolytes (SEs). However, up to the present time, the SEs fabrication for practical ASSLIB construction is still a significant challenge. The existing problems include 1) lower ionic conductivity compared to liquid electrolyte, 2) poor solid-solid contact interface between electrode and electrolyte, 3) volume change of the electrode and 4) the unstable interface of lithium metal/polymer electrolytes causes further capacity fading. With the aim of fabricating SEs which possess optimal properties, a novel SE was developed by forming a multilayer structure. The multilayer SE was fabricated using polymeric and ceramic electrolytes, which can integrate the merits from different layers and materials and optimize its overall performance.

In order to choose an ideal ceramic material for the multilayer electrolyte fabrication, three different types of ceramic electrolyte material were synthesized, characterized and evaluated, including $Li_{1.3}Ti_{1.7}Al_{0.3}(PO_4)_3$ (LATP), $Li_7La_3Zr_2O_{12}$ (LLZO) and $Li_{0.5}La_{0.5}TiO_3$ (LLT). Their

mechanical strength, ionic conductivity, ease of fabrication and synthesis, and economic expenses of synthesis were evaluated experimentally. The influence of sintering temperature, synthesis route, working temperature and pressure to the overall conductivity were evaluated. From experimental observation and analysis, it was concluded that LATP was an ideal candidate for multilayer electrolyte fabrication for its high conductivity, ease of fabrication and synthesis, etc.

The electrochemical properties of polymer electrolyte PEO_{10}-$LiN(CF_3SO_2)_2$, which was fabricated through hot pressing and solvent casting methods respectively, and also gel-polymer electrolyte $PVdF$-HFP-$LiN(CF_3SO_2)_2$ were characterized. The lithium ion transference number, ionic conductivity and thermo-stability were evaluated and discussed.

Based on the characterized ceramic and polymer electrolytes, the multilayer electrolyte was fabricated through various lamination protocols, which include hot pressing, dip coating and spray coating methods. It was found that negligible interfacial resistance exist at LATP/LLT and SPE material. Also, an enhanced ionic conductivity was found for the bilayer of LATP/solvent casted SPE. This phenomenon was attributed to the formation of a composition region at the polymer/ceramic electrolyte interface. It was suggested that the boundary of polymer body and ceramic grains may induce a pathway for enhanced ionic transportation. The porous LATP was fabricated using PMMA/PVA/PVB as the pore maker. The influencing factors of sintering temperature, material selection of ceramic and pore makers and fabrication methods deserve further investigation.

All-solid-state lithium ion coin cell was successfully fabricated and characterized using the as-prepared multilayer electrolyte and lithium metal anode. The coin cell demonstrated satisfactory charge/discharge capability and cyclability at an elevated temperature of 70 °C. The thickness of SE, operating temperature, material types were important factors in the overall resistance of the

multilayer solid electrolyte. The unstable lithium/polymer electrolyte interface at high temperature and high potential is the critical problem for developing ASSLIBs with better cyclability in practice.

In the end, future work was proposed and discussed based on the existing work, including 1) multilayer fabrication using glass-ceramic material; 2) optimization of porous ceramic electrolyte; 3) multilayer composite electrolyte using ceramic stabilizer at the lithium/electrolyte interface.

**MULTILAYER COMPOSITE SOLID ELECTROLYTES FOR LITHIUM ION
BATTERIES**

By
Wei Liu

B.S., Chongqing University, 2006
M.S., Chongqing University, 2009

DISSERTATION
Submitted in partial fulfillment of the requirements for the Degree of Doctor of Philosophy in
Mechanical Engineering in the Graduate School of Syracuse University
May 2016

Acknowledgements

This research work was conducted at the Combustion & Energy Research Laboratory (COMER) in the Department of Mechanical and Aerospace Engineering at Syracuse University. It took about 4 years (2012 ~ 2016) to complete the research works and this dissertation. I would like to thank many people who helped to make it possible.

First of all and foremost, I would like to express my special appreciation and thanks to my advisor Prof. Jeongmin Ahn, you have been a tremendous mentor for me. I would like to thank you for encouraging my research and for allowing me to grow as a research scientist. Your advice on my research has been invaluable.

I would also like to thank my committee members, Dr. Benjamin Akih-Kumgeh, Dr. Dacheng Ren, Dr. Jianshun Zhang, Dr. Shalabh C. Maroo, and Dr. Thong Dang for serving as my committee members even at hardship.

Finally, I would like to thank all my families for their continuous encouragement and support.

Wei Liu

Syracuse, March, 2016

List of Symbols

A	Electrode Area
C_i	Capacity of Item i
D_0^T	Pre-exponential Factor
D^{dc}	dc Diffusion Coefficient
D^T	Tracer Diffusion Coefficient
D^{uc}	Uncorrelated Jumps Diffusion Coefficient
e_0	Area Normalized Capacitance
E_A	Activation Energy
F	Correlation Factor
H	Thickness
H_R	Haven Ratio
I	Current
J_i	Mass Flux of Species i
K_b	Boltzmann Constant
L	Inductance
N_A	Avogadro's Number
n_c	Coordination Number
N_C	Number of Atoms in Unit Cell
R_i	Resistance of Item i
R_t	Decoupling Ratio
T	Temperature
t	Time

T_i	Transference Number of Species i
V	Voltage
V_C	Volume of Unit Cell
W_A	Atomic Weight
Z	Valence Number
$\dot{p}_i(t)$	Probability of Observing a Ion at Site i at Time t
$w_{i\to j}$	Probability per Unit Time of Hopping from Site i to Site j
ε_∞	Dielectric constant
$\langle r^2(t) \rangle$	Mean Square Displacement of Particles after Time t
τ	Mean Residence Time
τ_σ	Structural Relaxation Time
τ_s	Conductivity Relaxation Time
$\bar{\tau}_{hop}$	Average Waiting Time for a Hop to Occur
$\bar{\tau}_{ren}$	Renewal Time of Polymer Host
σ_{dc}	dc Conductivity
ρ_{th}	Theoretical Density
ρ_{rd}	Relative Density
ρ_{exp}	Experimental Density
σ_0	Pre-exponential Factor
σ_e	Electronic Conductivity

Acronyms

ACN   Acetonitrile

ASSLIB   All-solid-state Lithium Ion Battery

BBP   Butyl Benzyl Phthalate

c-LLZO   Cubic $Li_7La_3Zr_2O_{12}$

DBP   Dynamic Bond Percolation

DEC   Diethyl Carbonates

DMC   Dimethyl Carbonates

EC   Ethylene Carbonate

EIS   Electrochemical Impedance Spectroscopy

EMC   Ethyl-methyl Carbonates

EV   Electric Vehicle

GPE   Gel-type Polymer Electrolyte

HBP   Hyperbranched Polymer

HEV   Hybrid Electric Vehicle

HFP   Hexafluoropropylene

LAGP $Li_{1.5}Al_{0.5}Ge_{1.5}(PO_4)_3$

LATP $Li_{1.3}Al_{0.3}Ti_{1.7}(PO_4)_3$

LBLTO $Li_6BaLa_2Ta_2O_{12}$

LCLTO $Li_6CaLa_2Ta_2O_{12}$

LIB   Lithium Ion Battery

LiDMSI   Lithium-cyclo-difluoromethane-1,1-bis(sulfonyl)imide

LiTFSI   Bis(trifluoromethane)sulfonimide

LLBO	$Li_5La_3Bi_2O_{12}$
LLNIO	$Li_{5.5}La_3Nb_{1.75}In_{0.25}O_{12}$
LLT	$Li_{0.5}La_{0.5}TiO_3$
LLTO	$Li_5La_3Ta_2O_{12}$
LMO	Lithium Manganese Oxide
LSLBO	$Li_6SrLa_2Bi_2O_{12}$
MD	Molecular Dynamics
MEMS	Micro Electromechanical Systems
MS	Mechanical Strength
NASICON	Na Super Ionic Conductor
NMP	N,N-dimethylformamide
NMR	Nuclear Magnetic Resonance
PAN	Polyacrylonitrile
PC	Propylene Carbonate
PE	Polyethylene
PEG	Poly(ethylene glycol)
PEG	Polyethylene Glycol
PEGDA	Polyethylene Glycol Diacrylate
PEMFCs	Proton Exchange Membrane Fuel Cells
PEO	Poly(ethylene oxide)
PHEV	Plug-in Hybrid Electric Vehicle
PMMA	Poly(methyl methacrylate)
PP	Polypropylene

PPO	Poly(phenylene oxide)
PSt	Polystyrene
PVA	Poly(vinyl alcohol)
PVB	Polyvinyl Butyral
PVC	Poly(vinyl chloride)
PVdF	Poly(vinilidene fluoride)
PVP	Polyvinylpyrrolidone
PVS	Poly(vinyl sulfonate)
SE	Solid Electrolyte
SEI	Solid Electrolyte Interface
SOFCs	Solid Oxide Fuel Cells
SPE	Solid Polymer Electrolyte
SS	Stainless Steel
THF	Tetrahydrofuran
t-LLZO	Tetragonal $Li_7La_3Zr_2O_{12}$
XRD	X-ray diffraction

List of Tables

List of Figures

Table of Contents

Chapter 1 Introduction

1.1   Lithium Ion Batteries Introduction

Attempts to develop rechargeable lithium ion batteries (LIBs) started in the 1980s since researchers discovered the reversible intercalation of lithium ion in graphite and cathodic oxides. In 1991, SONY released the first commercial lithium ion battery. Since then, the lithium ion battery R&D has become the most attractive and promising technology in the battery industry. Due to its outstanding performance, LIBs soon edged out many other types of batteries, and became dominant in the battery market. Now LIBs are the standard power source for increasingly diverse range of applications, from Micro Electromechanical Systems (MEMS), to medium sizes of consumer portable electronics like mobile phones and tablets, to electric automobiles and large energy storage systems. Though the current existing technology and market of lithium ion batteries are sophisticated, the demand for lighter, safer, and shape-flexible rechargeable batteries continuously grows [1-3].

One of the most inspiring applications of LIBs is providing a power source for electrified vehicles, such as hybrid electric (HEV), plug-in hybrid electric (PHEV) and all-electric vehicles (EVs) [4]. Compared with conventional vehicles with gas engines, HEVs, PHEVs, and EVs have much less or even zero tailpipe emissions (though emissions are still generated by the production process of electricity). However, the higher energy efficiency of conventional fossil fuel power plants combined with increasing renewable and clean energy resources (e.g. wind, solar, biomass and nuclear energy), HEVs, PHEVs, and EVs have significantly reduced the production of greenhouse gases and air pollutants. Table 1-1 provides the emission and fuel costs of the electric powered vehicles versus conventional vehicles.

Table 1-1 Comparison of CO_2 emissions and fuel cost between different vehicle types

Emissions and Fuel Cost for a 100-Mile Trip			
Vehicle (compact sedans)	Greenhouse Gas Emissions	Energy Utility Efficiency	Total Fuel Cost (U.S. Dollars)
Conventional	99 lb CO_2	24.3 MPG	$11.60
Hybrid Electric	51 lb CO_2	47.3 MPG	$5.96
Plug-in Hybrid Electric	61 lb CO_2	39.3 MPG 0.41 kWh/mi	$6.78
All-Electric	54 lb CO_2	0.324 kWh/mi	$3.56

Source: US department of energy (March/2016). http://www.afdc.energy.gov/vehicles/electric_emissions.php

For any cars of HEVs, PHEVs or EVs, the power sources of batteries are the key component means for substituting for a gasoline engine. Today, those batteries are mainly nickel-metal hydride batteries (NiMHs) and lithium ion batteries. Compared with NiMHs, LIBs are the ultimate solution for the future due to the following advantages: 1). higher power density; 2). higher energy density; 3). cost-effectiveness; 4). good cycleability; 5). environmental friendliness. Figure 1 provides a historic and predicted trend of LIBs needed by the automobile industry. We can see a rapidly increasing need for LIBs in the foreseeable future.
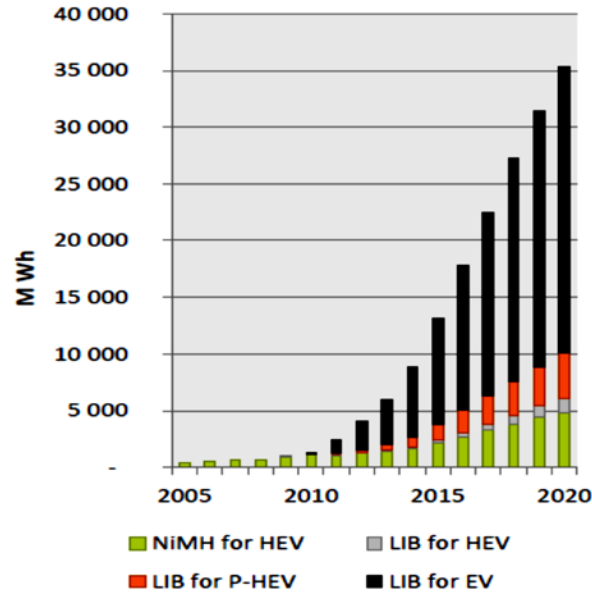
Figure 1-1 EV, HEV and PHEV Battery needs [5]

Like other types of rechargeable batteries, rechargeable lithium ion batteries (LIBs) are devices which can store and release electric energy at charging and discharging respectively. A typical rechargeable LIB has three components: cathodes, anodes, and electrolytes. Cathodes (positive electrode) are based on oxidant materials. Typical cathode materials include lithium oxide chemical compounds (LiMO), (e.g., $LiCoO_2$, $LiNiO_2$, spinel $LiMn_2O_4$) or phosphates ($LiMPO_4$) with an olivine structure (e.g., $LiFePO_4$, $LiMnPO_4$, $LiCoPO_4$) [6].

Anodes (negative electrode) are based on reductant materials. Lithium metal is an optimum anode material, but due to the lithium dendrite problem, insertion compounds are used as substitutes. Thanks to the highly reversible lithium ion intercalation-deintercalation ability of carbonaceous material [7], SONY's high performance LIB was constructed using graphite as anode material and LiCoO2 as cathode material [2]. Nowadays, the commercial LIBs still use graphite as the anode material.

The electrolyte is the medium that separates the anode and cathode, and provides a flow route for the lithium ions. Conventional liquid electrolytes are composed of lithium salt (e.g., $LiPF_6$,

LiClO₄) dissolved in organic solvent. A typical solvent includes ethylene carbonate (EC) as a necessary component, and dialkyl carbonates from dimethyl, diethyl, ethyl–methyl carbonates (DMC, DEC, and EMC), etc. [8].

At charging, the lithium ions de-intercalate from the cathode material and intercalate into the anode material across the electrolyte, thus storing energy. At discharging, the process reverses and the ions move back from anode to cathode, while electrons move in the outer circuit in an opposite direction from cathode to anode.
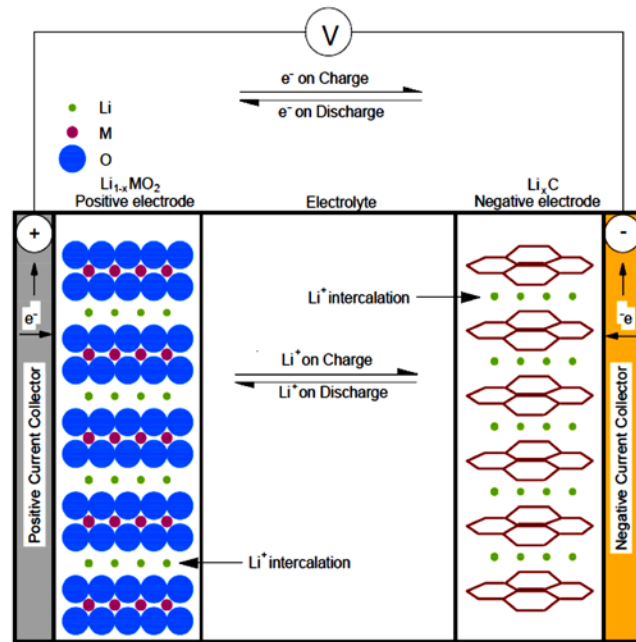
Figure 1-2 Schematic of the electrochemical process in a LIB

The working mechanism of a lithium ion battery is described in Figure 1-2. In the scheme, LiMO₂ represents the metal oxide positive material, C is carbonaceous negative materials. The chemical reactions can be described by the following formula.

Reaction at positive electrode: $LiMO_2 \xleftrightarrow{charge/discharge} Li_{1-x}MO_2 + xLi^+ + xe^-$

Reaction at positive electrode: $C + xLi^+ + xe^- \xleftrightarrow{charge/discharge} Li_xC$

Overall reaction: $LiMO_2 + C \xleftrightarrow{charge/discharge} Li_xC + Li_{1-x}MO_2$
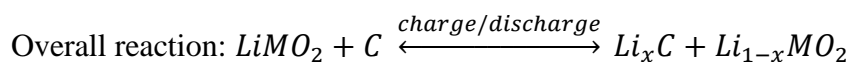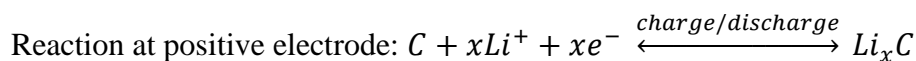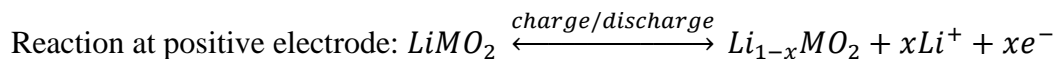
1.2　Advantages of All-Solid-State Lithium Ion Battery

Today, researchers endeavor to improve the performance of LIBs to meet the stringent requirements for EVs. However, there are several inherent disadvantages of the traditional commercial LIBs, all of which are related to properties of the liquid electrolyte.

Firstly, the safety and durability of traditional LIBs are unacceptable. The self-ignition or explosion of the batteries in cell phones or laptops has aroused much of the public's attention. For batteries of electrified road vehicles, which need to be operated mostly under aggressive conditions, reliability and abuse tolerance become more critical. Due to the occasional assembly defect or under some specific abuse conditions, including but not limited to mechanical abuse (crush, penetration, shock), electrical abuse (internal short circuit, overcharge, over discharge) or thermal abuse (overheating from external/internal sources), failure of the battery may occur [9, 10]. Those conditions are especially dangerous for a conventional battery due to the existence of the highly flammable liquid electrolyte. Those batteries have a tendency to undergo a dangerous state of 'thermal runaway', where abuse environments trigger the internal heat generated by the battery and accumulates to a threshold temperature to make it begin a chain of exothermic reactions and cause spontaneous combustion [11, 12]. Also, to prevent leakage, the highly combustible liquid electrolyte need to be well-sealed in a rigid battery container, which is commonly made of stainless steel. This may cause the pressure to build up; thus, when the thermal runaway happens, the explosion may happen in the end [13].
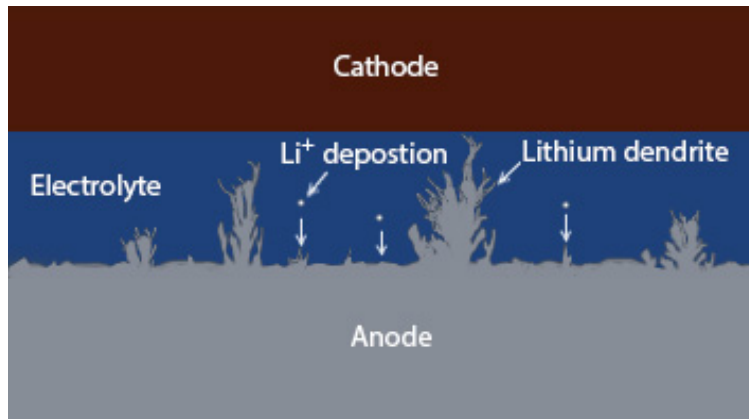
Figure 1-3 Schematic structure of lithium dendrite growth
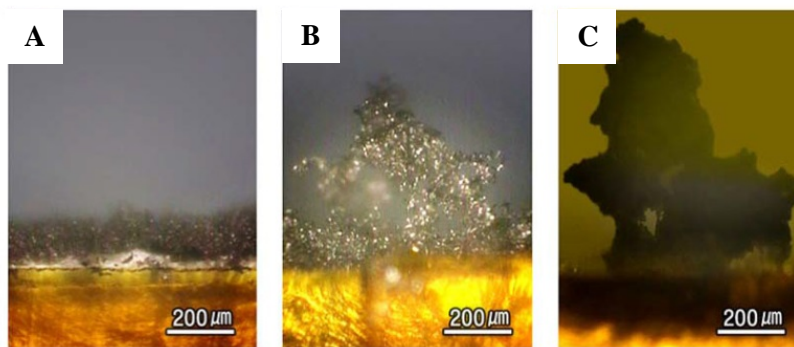
Figure 1-4 In-situ SEM observation of the lithium dendrites growth

Secondly, liquid electrolyte limits the application of lithium metal as anode material. Lithium metal is considered as the "ultimate anode material" because it is the most electropositive element vs. standard hydrogen electrode. Moreover, it can provide a capacity of 3800 mAh g^{-1}, which is about 10 times higher than that of carbon-based anode (372 mAh g^{-1}) [14]. However, the dendrite growth of the lithium metal potentially hampers this replacement for liquid electrolyte LIBs. In commonly used liquid electrolyte systems, the formation of lithium dendrites results from the interfacial instability and inhomogeneity between liquid electrolyte and lithium metal, where the lithium ion deposition-dissolution processes are observed in a non-uniform pattern [15]. The lithium dendrite nucleate is then generated from the lithium anode and the dendrite continues to grow in a tree-like pattern at a charging stage, until penetrating the polypropylene (PP) and

polyethylene (PE) separator and contacts with the positive electrode. In this situation, a short circuiting of the battery occurs, which causes the battery to fail, generating a lot of heat, and igniting the liquid organic electrolyte or causing the battery to explode. Figure 1-3 is the schematic lithium dendrites growth. Figure 1-4 is the in-situ macroscopic observation of lithium dendrites growth at various liquid electrolyte systems: A) $LiN(CF_3SO_2)_2$ (1M) in DME, B) $LiN(CF_3SO_2)_2$ (1M) in tetraglyme, C) LiI(1M) in tetraglyme [16].

All-solid-state lithium ion batteries (ASSLIBs) provide a promising strategy to overcome the drawbacks of liquid electrolyte by substituting the highly flammable organic liquid electrolyte with a solid electrolyte (SE). There are two main types of SE materials that have been investigated: solid inorganic electrolyte (e.g., $Li_{0.5}La_{0.5}TiO_3$ (LLT), $Li_{1+x}Al_xTi_{1-2x}(PO_4)_3$ (LATP), $Li_7La_3Zr_2O_{12}$ (LLZO), etc.) and polymeric electrolyte (e.g., lithium salt dissolved in poly(ethylene oxide) (PEO) polymer matrix). Those SE materials has several advantages compares with liquid electrolyte.

Unlike the PP and PE separators soaked with liquid electrolyte, the inorganic ceramic electrolyte can stop or suppress the lithium dendrite growth in two aspects. On the one hand, the glass ceramic or ceramic electrolyte has high mechanical strength (MS), so as to physically block the growth path of the lithium dendrites [17]. One the other hand, most inorganic ceramic electrolytes have a large electrochemical stability window, which makes it compatible with the lithium metal anode or the oxidizing agent in the cathode [18]. For example, LLZO is a novel ceramic electrolyte possessing high ionic conductivity and high stability at the same time [19]. Since most solid state electrolytes have electrochemical windows greater than 5V, a higher voltage of cathode can be used to further increase the voltage and power density of the battery [20].

Furthermore, solid electrolyte-based LIBs can also increase the power density by simplifying the design of the battery container; that is, the battery weight can be decreased by replacing the

traditional rigid metal container with a vacuumed 'soft plastic' pouch cell stack design. This also reduces battery cost, improves shape design flexibility, and increases durability in aggressive environments [21]. This pouch cell design also prevents the build-up of pressure inside the container, thus eliminating the possibility for explosion [22].

Last but not least, the solid electrolyte also enables the application of organic and aqueous electrolytes on the anode and cathode side. This is the design principle of the so-called lithium-air battery, which significantly improves the theoretical power density [23]. The solid electrolyte enables 1) the use of lithium metal as anode, which can maximize the battery voltage and power density, and 2) the use of oxidant gases (e.g., air) or liquid-flow oxidant reactant cathode material which has significant increased capacity [2]. However, compared to conventional LIBs, the performance of lithium-air batteries are still very limited due to several issues regarding both the electrode and electrolyte [24].

To sum up, by replacing flammable liquid electrolytes with solid electrolytes, ASSLIBs can widen their operating parameters (e.g. higher temperature, higher voltage) with enhanced safety reliability and durability. Also, ASSLIBs can suppress lithium dendrite growth, improve battery design flexibility, and therefore increase power density. Ultimately, ASSLIBs can provide a promising power strategy for electrified vehicle applications [14].

1.3   Challenge to Solid Electrolyte

Though the solid electrolyte is a promising alternative to constructing all-solid-state lithium ion batteries, there are several major issues hampering its application and commercialization.
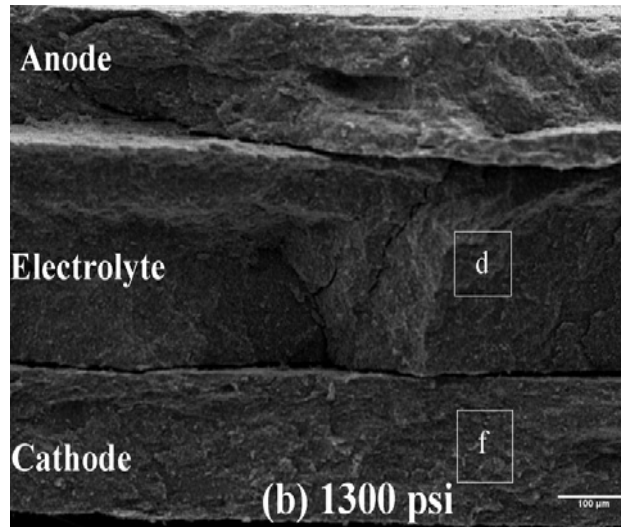
Figure 1-5 Scanning electron microscope (SEM) image at the solid-solid contact interface [25]

Firstly, solid electrolytes are not as conductive as liquid electrolytes. Before any new lithium ion conductive material can be discovered, there are several solutions to this problem. First, the conductivity of the electrolyte can be compensated by making it thinner without losing the mechanical stress to stop the lithium dendrite. Ohara has developed a solid glass ceramic lithium ion conductor with a minimized thickness less than ~30 µm [26]. Second, the solid electrolyte has an acceptable conductivity at higher temperatures [18]. This is compatible with the plug-in hybrid powered vehicles, where a higher temperature can be provided by a regular engine.

Secondly, the poor solid-solid contact is the main challenging issue for those stiff glass ceramic or ceramic electrolytes. Figure 1-5 shows the SEM structure at the solid-solid interface, where we can see the existing gaps [25]. To achieve favorable solid-solid interfacial contact, different methods were investigated, which include depositing an intermedia layer [27-29], hetero-epitaxial growth of the electrolyte [30], or interfacial nano-architectonics modification [31].

Third, how to effectively accommodate the volume changes of electrodes during cycling remains problematic. Volume change is a phenomenon for the host material of graphite and silicon anodes, as the lithiation/delithiation process produces volume changes of ~10% and ~400%

9

respectively. For the "hostless" lithium metal anode, the relative volume change is virtually infinite [32].
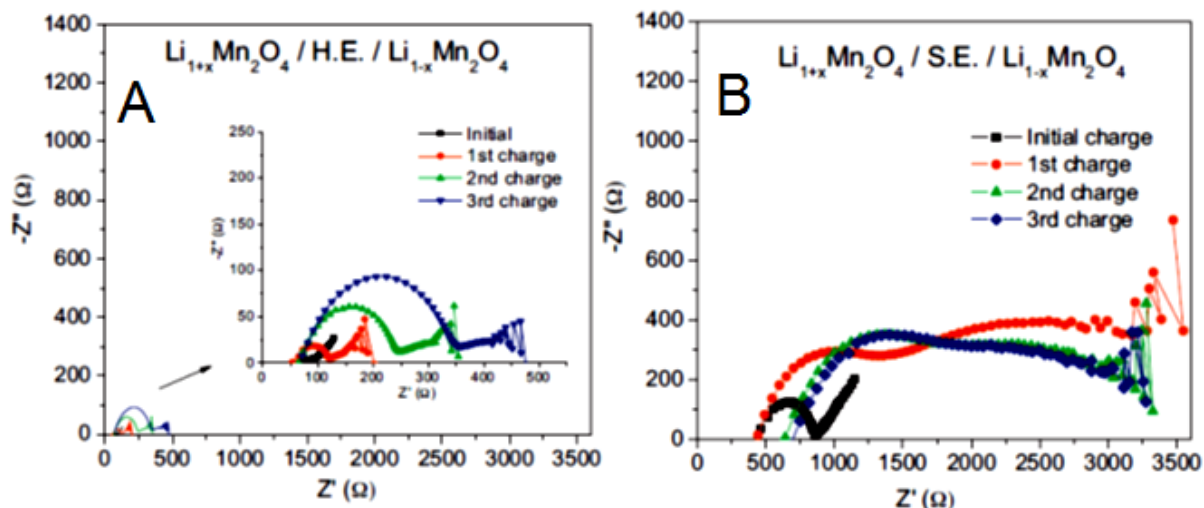
Figure 1-6 Impedance profiles at and after initial charging of (A) a hybrid electrolyte cell and (B) a solid electrolyte (S.E.) cell [25]

Figure 1-6 reveals the impedance profiles at and after initial charging of a hybrid electrolyte cell and a solid electrolyte cell [25]. A hybrid electrolyte LIB was fabricated by adding liquid electrolytes at the electrode/electrolyte interface, which can significantly improve the performance versus pure solid electrolyte LIBs. Using a scanning electron microscope (SEM), it was found that the volume change of the electrode created empty space (or cracks) in the electrode/electrolyte interface, thus inducing additional interfacial resistance, and deteriorating the cycling performance of the solid electrolyte cell. It was shown that by using the nanoscale engineering approach, for example, coating the lithium metal anode with a monolayer of interconnected amorphous, hollow carbon nano-spheres can accommodate the volumetric change during lithium deposition and dissolution [32].

To sum up, the chemical, electrochemical, and mechanical stability of the interfaces is essential to minimize interfacial impedance. An intimate contact with stable electrochemical

properties at the solid/solid interface between the electrode and electrolyte is key to improving

battery performance [25].

Chapter 2 Literature Review

2.1   Introduction

The solid electrolyte, according to its chemical composition or configuration, can be classified into the following types: 1) solid polymer electrolytes, 2) inorganic electrolytes, and 3) gel-type polymer electrolytes. These types of solid electrolytes vary with conductivity, mechanical strength, and stability versus electrodes, etc. These discrepancies enable those different solid electrolytes, with individual advantages and disadvantages, to function as solid electrolytes in a practical ASSLIBs. The current development status and highlights of these different types of solid electrolytes are presented in the following.

2.2   Solid Polymer Electrolytes

The solid polymer electrolytes (SPEs) are typically formed by dissolving a lithium salt (LiX) in a solid polymer matrix. The polymer substrate includes polyacrylonitrile (PAN), polyethylene oxide (PEO), poly(vinyl chloride) (PVC), poly(methyl methacrylate) (PMMA), and poly(phenylene oxide) (PPO), etc. PEO-LiX-based electrolytes are the most widely investigated solid electrolyte system.
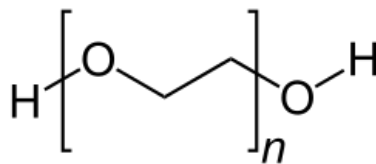
Figure 2-1 Molecular structure of PEO

Polyethylene oxide is a polyether compound that is widely used in biochemistry, medicine synthesis and many other industrial manufacturing processes. The chemical formula of PEO is $C_{2n}H_{4n+2}O_{n+1}$. Figure 2-1 is the chemical structure of PEO. Varying in chain length, PEO is also referred to as PEG (polyethylene glycol), which has a molecular mass below 20,000 g/mol.

Generally, PEO refers to polymers with a molecular mass above 20,000 g/mol. The ionic conduction of PEO ionic conductivity in alkali metal salt complexes was discovered by Fenton, Parker and Wright in 1973 [33]. Since then, a large number of polymer electrolyte systems have been investigated, involving a variety of transportation ions, e.g., H^+, Li^+, Na^+, K^+, Ag^+, etc.[34].

Wright characterized the variation of the ionic conductivity with temperature in 1975 [35]. Armand et al. recognized the potential of these materials in lithium batteries in 1978 [36]. Also, a large variety of lithium salts have been investigated, which include Li_2SO_4, $LiNO_3$, $LiAsF_6$, $LiClO_4$, $LiCF_3SO_3$, $LiPF_6$, $LiBF_4$, LiBOB, $LiN(CF_3SO_2)_2$ (or LiTFSI) and LiDMSI, etc. Those lithium salts were experimentally examined from many aspects, including conductivity, thermal stability, moisture tolerance, safety and etc. These chemical properties are important for a PEO-LiX system, and they vary a lot from each other. For example, the conductivity in solutions is a very critical parameter when lithium salt is used as an electrolyte. A comparison of the degree of dissociation in 1:1 PC: DME is $LiPF_6 \sim LiAsF_6 > LiClO_4 \sim LiN(CF_3SO_2)_2 \gg LiBF_4 \gg LiCF_3SO_3$ [37]. Table 2-1 is a summary of the properties of common lithium salts from literature review.

Table 2-1 Summary of properties of different lithium salts

Lithium salt	Properties
Li_2SO_4,	Aqueous Electrolytes [38]
$LiNO_3$, LiCl	High power density due to high ionic conductivity [39]
	Low energy density due to narrow stability window of water [40]
$LiAsF_6$	Toxicity of salt degradation products [40]
	Effects of the disposal to environments [40]
$LiClO_4$	Safety issue [40]
$LiCF_3SO_3$	Low conductivity [40]
	More Stable, more safer lithium salt [37]
$LiPF_6$	Provide stable SEI with graphite anode.

	Poor thermal stability (decomposition at 125 °C)
	poor in terms of hydrolysis
	Dominant salt in commercial LIBs due to its balanced properties [40]
LiBF$_4$	Better thermal stability and moisture tolerance than LiPF$_6$ [41, 42]
	Performance well at high (50-80°C) and low temperatures (-20 °C)
	Main disadvantage is moderate conductivity[40]
LiBOB	Low cost, high thermal stability, mild chemical decomposition product [43]
	Lower conductivity than LiPF$_6$
	Can form stable SEI with graphite material [44]
LiTFSI	Aluminum corrosion [40]
	High stability against hydrolysis [45]
	Increase the PEO plasticization [46]
	High electrochemical stabilities [47]
LiDMSI	Used as electrolyte additive to LiPF$_6$ electrolyte, can form stable SEI on a
	Graphite anode and passivate an Al current collector [48]

It is widely accepted that ionic conductivity is related to the segmental motion and local relaxation of the polymer chains in amorphous regions of the PEO polymer host above the glass transition temperature Tg [49, 50]. The ionic dynamic motion in a PEO-LiX system has been proposed to be described as follows [51, 52, 53]: 1) the cation is temporarily attached to polymer chains by electrostatic bonds; 2) there is a cooperative motion of ions and polymer segments, the ions use the chains as vehicles; 3) there is motion of the ions along a chain, and finally 4) there are jumps between different chains (percolation mechanism). The most critical issue for SPEs that aim for practical application is how to improve the ionic conductivity, which requires a conductivity of about 10^{-4} S cm^{-1} [49].

Researchers have found that many factors can affect the conduction of cations in PEO. It was found that the solubility parameters are strongly influenced by certain types of metal salts [36]. It

seems the bulky anions of lithium salt can lower the melting temperature of the PEO-LiX system [46].

The ratio of ether oxygens to the lithium salt was also found to be important for the mechanical and transportation properties of the system [54, 55]. G. S. MacGlashan et al. [56, 57] found that in a PEO-LiAsF$_6$ SPE system, the ratio difference can affect the structure of the polymer system, whereas in the 3:1(EO: Li) complexes the polymer chains form helices. Those in the 6:1 complex form double non-helical chains that interlock to form a cylinder, and the lithium ions reside inside these cylinders. This structural difference brings a significant improvement in conductivity when the polymer content changes from 3:1 to 6:1.

However, in contrast, Z.Gadjourova et al. [58] claim that ionic conductivity in the static, ordered environment of the crystalline phase can be greater than that in the equivalent amorphous material above Tg.

In fact, not only the ionic conductivity, but other physiochemical properties, e.g., the mechanical strength and compatibility of the SPE material to the lithium metal anode, are also important properties for consideration for practical application in all-solid-state batteries. To improve the comprehensive performance of SPEs, lots of research has been carried out so far. This research includes: 1) using other host polymer materials [59-62], 2) EO:Li ratio optimization [63-65], 3) synthetization of block copolymers [66,67], grafted polymers [68], cross-linked polymers [69], and comb-like polymers [70], 4) adding plasticizer [71], 5) adding ceramic fillers [72], and 6) adding liquids [73]. Molecular dynamics (MD) simulations have also drawn a lot of attention recently in an effort to better understand the transportation mechanisms [74, 75].

Table 2-2 lists the conductivities of various solid polymer electrolytes using different polymer materials with different lithium salts. We can see the range of the conductivities is from $\sim10^{-9}$ to $\sim10^{-3}$ in room temperatures.

Table 2-2 Comparison of conductivity of different solid polymer electrolytes

Polymer system	Conductivity(S cm-1)	T (°C)	Reference
PEO_{16}-$LiCF_3SO_3$	2×10^{-7}	25	[46]
PEO_{10}-$LiN(CF_3SO_2)_2$	1×10^{-6}		
$(PEO$-$HBP)_{10}$ - $LiPF_6$	9×10^{-5}	25	[54]
PEO_6:$LiSbF_6$	2×10^{-8}(amorphous region)	25	[58]
	8×10^{-8}(crystalline region)		
PEO_{10}-$LiN(CF_3SO_2)_2$	4×10^{-5}	25	[55]
PEO_8-$LiN(CF_3SO_2)_2$	2.5×10^{-5}		
$(P(MEO_{16}$-$AM))$-$LiClO_4$	4×10^{-4}	R.T.	[59]
PEI-$LiN(CF_3SO_2)_2$	8.5×10^{-7}	R.T.	[60]
PVC-PAN- $(30$ wt%$)LiN(CF3SO_2)_2$	4.39×10^{-4}	R.T.	[61]
$(PSt$-b-$PPME$-b-$PSt)_{20}$-$LiClO_4$	2×10^{-4}	30	[66]
$(PEO$-$PMMA)_{16}$-LiI	$\sim10^{-4}$	60	[67]
$PEGMEM$-$(GMA$-$IDA)$	5×10^{-6}	30	[70]
$(PDMAEMA$-$PEO)$-$LiN(CF_3SO_2)_2$	4.74×10^{-4}	25	[71]
$(PEO$-$PMA)_{16}$-$LiClO_4$	5×10^{-6}	30	[72]
$(PEO$-$PMA)_{32}$-$LiClO_4$	4×10^{-6}		
PEO_8-$LiClO_4$	5×10^{-6}	25	[76]

16

(PEO)$_{4.5}$-LiSCN	2×10^{-8}	30	[77]
(PEO)$_8$-LiClO$_4$	1×10^{-7}	27	[78]
(PEO)$_{12}$-LiBF$_4$	1×10^{-6}	25	[79]
(PPO)$_8$-LiCF$_3$SO$_3$	2×10^{-5}	70	[80]
(PEO$_{400}$)$_{25}$-LiSCN	5×10^{-4}	25	[81]
(PPO$_{425}$)$_{25}$-LiClO4	6×10^{-5}		
(PEO)$_6$-LiCF$_3$SO$_3$	1.5×10^{-7}	30	[82]
PEO$_{20}$LiN(CF$_3$SO$_2$)$_2$+ PYR$_{13}$TFSI	10^{-5}-10^{-3} (PYR$_{13}$:Li$^+$: 0.66-3.24)	30	[73]
(PEO)n- LiCF$_3$SO$_3$	~2×10^{-7} (n=4, 8, 12, 20, 50)	25	[83]
α-CD-PEO/LiAsF$_6$	5×10^{-9}	25	[84]
PEO-ENR$_{50}$-(20 wt%)LiCF$_3$SO$_3$	1.4×10^{-4}	R.T.	[85]

The lithium ion transport in solid polymer electrolyte is very complex process considering the multiphase structure at macroscopic/microscopic level of the polymer electrolyte system, which include the local motion of polymer segment and the ion hopping on the same polymer chain or to different chains [86]. The ionic motion and relaxation of the polymer host was formalized using the decoupling ratio [87],

$$R_\tau = \frac{\tau_s}{\tau_\sigma} \qquad \text{Eq. (2-1)}$$

τ_s is the structural relaxation time refers to viscosity or segment relaxation (sec), τ_σ is the conductivity relaxation time (sec) which can be calculated by dc conductivity of the material by,

$$\tau_\sigma = \frac{\varepsilon_\infty e_0}{\sigma_{dc}} \approx 9 \times 10^{-13}/\sigma_{dc} \qquad \text{Eq. (2-2)}$$

Where e_0 is area normalised capacitance, ε_∞ is dielectric constant, and $e_0 = 8.5 \times 10^{-14} F/cm$, $\varepsilon_\infty \approx 12$, while $\tau_s = 200s$ at glass transition temperature. From Eq. (2-2), we can see the ionic conductivity increases when the host polymer relaxes more rapidly.

Various ion transport mechanisms has been discussed. One theoretic model which related the ion diffusion behavior with the segment motion of the polymer chains is dynamic bond percolation (DBP) theory proposed by Druger, Ratner and et al. [88, 89].

DBP model describes the motion of ions between sites in the dynamically disordered polymer. Since the actual amorphous polymer motion is complicated, so a dynamic lattice model is developed. First, a space lattice is imposed on the system, such that the lattice sites hold the stable positions for the moving ions. Then a master equation is set up in the following form,

$$\dot{p}_\iota(t) = \sum_{j \neq i}'\{p_j(t)w_{j \to i} - p_i(t)w_{i \to j}\} \qquad \text{Eq. (2-3)}$$

where $\dot{p}_\iota(t)$ is the probability of observing a ion at site i at time t, $w_{i \to j}$ is the probability per unit time of hopping from site i to site j. Also,

$$n_c \bar{\tau}_{hop} w = 1 \qquad \text{Eq. (2-4)}$$

$\bar{\tau}_{hop}$ is the average waiting time for a hop to occur, n_c is the coordination number, which equal to 2 for one-dimensional case,

$$w_{i \to j} = \begin{cases} 0, & when\ i\ and\ j\ are\ not\ neighbors \\ 0, & when\ i\ and\ j\ are\ neighbors\ but\ the\ bond\ (i,j)is\ unavailable \\ w, & when\ i\ and\ j\ are\ neighbors\ and\ bond\ (i,j)is\ available \end{cases} \qquad \text{Eq. (2-5)}$$

A renewal time $\bar{\tau}_{ren}$ is introduced which indicates the time of renewal process of the polymer host resulting from polymer chain motion. So that the chain motion can reassign the values of $w_{i \to j}$ in time of $\bar{\tau}_{ren}$. It was suggested the DBP model can provide important experimental realized behavior when the observation time t $>> \bar{\tau}_{ren}$.

18

2.3 Inorganic Electrolytes

Inorganic electrolytes include ceramic and glass-ceramic electrolytes. The main differences between the glass-ceramic and ceramic materials is the extent of their crystallization. Unlike ceramic materials that have a high crystallinity, glass-ceramics not only have a crystalline phase, but they also have an amorphous phase region. Compared to SPEs, GPEs, or CPEs, most ceramic/glass-ceramic electrolytes have a higher mechanical strength to prevent dendrite formation. Also, like SPEs, the ionic conductivity of a ceramic solid electrolyte increases with the increasing of temperature. Due to the elimination of combustible liquid, ceramics are more suitable for high temperatures or other aggressive environments. Typical ceramic electrolytes include NASICON-type (e.g., $Li_{1+x}Ti_{2-x}Mx(PO_4)_3$ (M=Al, Ga, In, Sc)), garnet-type (e.g., $Li_5La_3M_2O_{12}$ (M = Al, Ga, In, Sc), $Li_3Ln_3Te_2O_{12}$ (Ln = Y, Pr, Nd, Sm and Lu), $Li_6ALa_2Ta_2O_{12}$ (A= Sr, Ba), and etc.), and LISICON-type (e.g., Li_2S-Li_2O-P_2S_5) [18, 90, 91], etc. Table 2-3 is a brief summary of the different types of inorganic lithium ion conductors by literature review.

Table 2-3 Literature review on the different types of inorganic lithium ion conductors

Composition Formula	Short name	Conductivity	T (°C)	Ref.
$Li_{3.3}PO_{3.9}N_{0.17}$	LiPON	2×10^{-6}	R.T.	[92]
$Li_{1.3}Al_{0.3}Ti_{1.7}(PO_4)_3$	LATP(ceramic)	7×10^{-4}	R.T.	[93]
$Li_{1.4}Al_{0.4}Ti_{1.6}(PO_4)_3$	LATP(glass-ceramic)	5.16×10^{-4}	R.T.	[94]
$14Li_2O$-$9Al_2O_3$-$38TiO_2$-$39P_2O_5$	LATP(glass-ceramic)	1.3×10^{-3}	R.T.	[95]
$Li_{1.3}Al_{0.3}Ti_{1.7}(PO_4)_3$	LATP(glass-ceramic)	6.53×10^{-4}	30	[96]
$LiTi_2(PO_4)_3$	LTP	2×10^{-5}	R.T.	[97]
$Li_{1.3}Al_{0.3}Ti_{1.7}(PO_4)_3$	LATP	6×10^{-5}	R.T.	[97]
$Li_{1.3}Al_{0.2}Y_{0.1}Ti_{1.7}(PO_4)_3$	LAYTP	1.2×10^{-4}	23	[98]

Li_2O-Al_2O_3-SiO_2-P_2O_5-TiO_2-GeO_2	LiC-GC(Melted)	1×10^{-4}	R.T.	[26]
Li_2O-Al_2O_3-SiO_2-P_2O_5-TiO_2	LiC-GC(Tape casted)	3×10^{-4}	R.T.	[26]
$Li_{1.5}Al_{0.5}Ge_{1.5}(PO_4)_3$	LAGP(glass-ceramic)	5.08×10^{-3}	27	[99]
$17.5Li_2O$-$5Al_2O_3$-$40GeO_2$-$37.5P_2O_5$	LAGP(glass ceramic)	3.99×10^{-4}	30	[97]
$Li_{1.4}Al_{0.4}(Ge_{0.67}Ti_{0.33})_{1.6}(PO_4)_3$	LAGTP(glass ceramic)	6.21×10^{-4}	R.T	[100]
$Li_{0.34}La_{0.51}TiO_{2.94}$	LLT	2×10^{-5}	R.T.	[101]
$La_{0.57}Li_{0.3}TiO_3$	LLT	$\sim 10^{-5}$	R.T.	[102]
$Li_5La_3Ta_2O_{12}$	LLTO	1.3×10^{-4}	R.T.	[103]
$Li_{0.45}La_{0.48}TaO_3$	LLTO	8.75×10^{-4}	R.T.	[104]
$Li_6SrLa_2Ta_2O_{12}$	LSLTO	7.0×10^{-6}	22	[105]
$Li_6BaLa_2Ta_2O_{12}$	LBLTO	4.0×10^{-5}	22	[105]
$Li_5La_3Bi_2O_{12}$	LLBO	1.9×10^{-5}	22	[106]
$Li_6SrLa_2Bi_2O_{12}$	LSLBO	2.0×10^{-5}	22	[106]
$Li_6CaLa_2Ta_2O_{12}$	LCLTO	2.2×10^{-6}	27	[107]
$Li_6BaLa_2Ta_2O_{12}$	LBLTO	1.3×10^{-5}	R.T.	[107]
$Li_5La_3Ta_2O_{12}$	LLTO	1.2×10^{-6}	R.T.	[91]
$Li_6BaLa_2Ta_2O_{12}$	LBLTO	4×10^{-5}	R.T.	[91]
Cubic $Li_7La_3Zr2O_{12}$	c-LLZO(solid state)	2.44×10^{-4}	R.T.	[108]
Cubic $Li_7La_3Zr_2O_{12}$	c-LLZO(sol-gel)	1.39×10^{-4}	R.T.	[109]
Tetragonal $Li_7La_3Zr_2O_{12}$	t-LLZO	1.63×10^{-6} (bulk) 5.59×10^{-7} (grain boundary)	R.T.	[110]
$Li_7La_3Zr_2O_{12}$	LLZO	$\sim 10^{-4}$ (c-LLZO) $\sim 10^{-7}$ (t-LLZO)	25	[111] [112]
$Li_7La_3Zr_2O_{12}$	LLZO(thin film)	1.67×10^{-6}	R.T.	[113]
$(Al_2O_3$ 1.25 mol%)-$Li_7La_3Zr_2O_{12}$	LLZO Al_2O_3 added	1.4×10^{-4}	30	[19]

$Li_{14}ZnGe_4O_{16}$	LZGO	6.21×10^{-6}	R.T.	[114]
$45Li_2S-35Li_2O-20P_2S_5$	$Li_2S-Li_2O-P_2S_5$ system	6.5×10^{-5}	R.T.	[90]
$Li_{5.5}La_3Nb_{1.75}In_{0.25}O_{12}$	LLNIO	1.8×10^{-4}	48	[115]
$0.48LiI-0.52Al_2O_3-0.44H_2O$	Li ion conductor-mesoporous oxide	2.1×10^{-4}	R.T.	[116]
$74.4Li2S-2.4GeS2-23.2P2S5$	$Li_2S-GeS_2-P_2S_5$ system	1.2×10^{-3}	R.T.	[117]
$67.5Li_2S-7.5Li_2O-25P_2S_5$	$Li_2S-Li_2O-P_2S_5$ system	2.7×10^{-4}	R.T.	[118]
$70Li_2S-30P_2S_5$	$Li_2S-P_2S_5$ system	3.2×10^{-3}	R.T.	[119]

The NASICON (Na Super-Ionic Conductor) type crystallographic structure $NaA_2^{IV}(PO_4)_3$ (A^{IV} = Ge, Ti and Zr) was identified in 1968 [18]. NASICON type materials (e.g., $LiTi_2(PO_4)_3$ (LTP))are promising candidates for lithium ion conduction because of their three-dimensional diffusion network [120]. It was found the lithium conduction can be enhanced by partial substitution of tetravalent cations (Ti^{4+}) by trivalent ones (Al^{3+}, Fe^{3+}, Y^{3+}, etc.) [121]. The compound family with general formula $Li_{1+x}Ti_{2-x}M_x(PO_4)_3$ (M = Al, Ga, In, Sc) was investigated [122]. Figure 2-2 is the lithium ionic conductivities of various ceramic conductors with a NASICON-type structure.
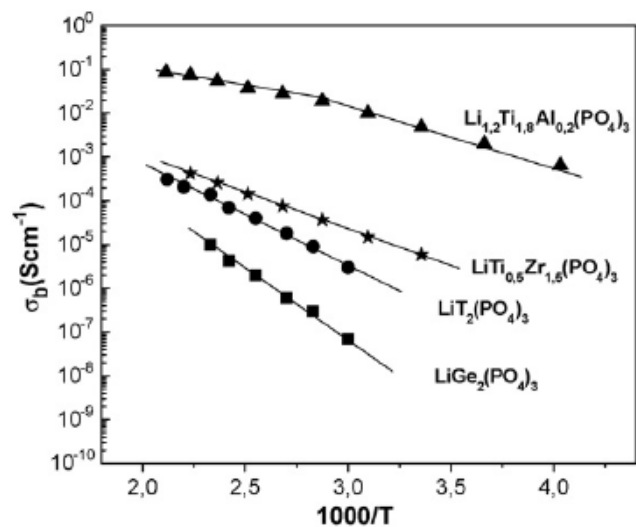
Figure 2-2 Arrhenius plot of ionic conductivity of various solid lithium ion conductors with

NASICON structure [122]
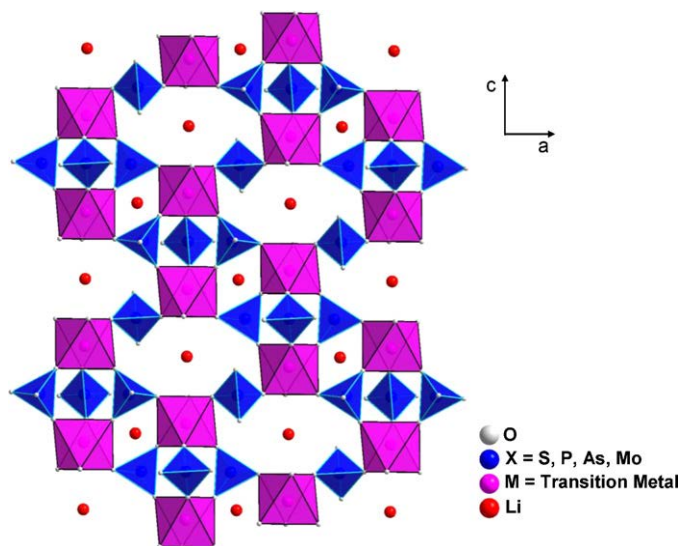
Figure 2-3 Crystal structure of $Li_{1.3}Ti_{1.7}Al_{0.3}(PO_4)_3$ [14]

Among the NASICON-type lithium ion conductors, $Li_{1+x}Al_xTi_{1-2x}(PO_4)_3$ has recently been widely investigated due to its high ionic conductivity, high electrochemical stability window, and stability in air and water [123, 124]. When x=0.3, the composition $Li_{1.3}Al_{0.3}Ti_{1.7}(PO_4)_3$ was reported to have the highest Li ionic conductivity [18]. Figure 2-3 is the crystal structure of

$Li_{1.3}Ti_{1.7}Al_{0.3}(PO_4)_3$ materials. Most of the research on LATP focuses on the different effects of the parameters for its conductivity; for example, the microstructure [125], the different element ratio [123], and the synthesis route [126-129], etc. Despite its manifold advantages compared with other inorganic conductors, it was reported that these NASICON-type materials of LATP are unstable with Li metal due to facile Ti^{4+} reduction [19]. Therefore, a Ti^{4+} free NASICON ceramic electrolyte was developed and attracted much attention [130-134].
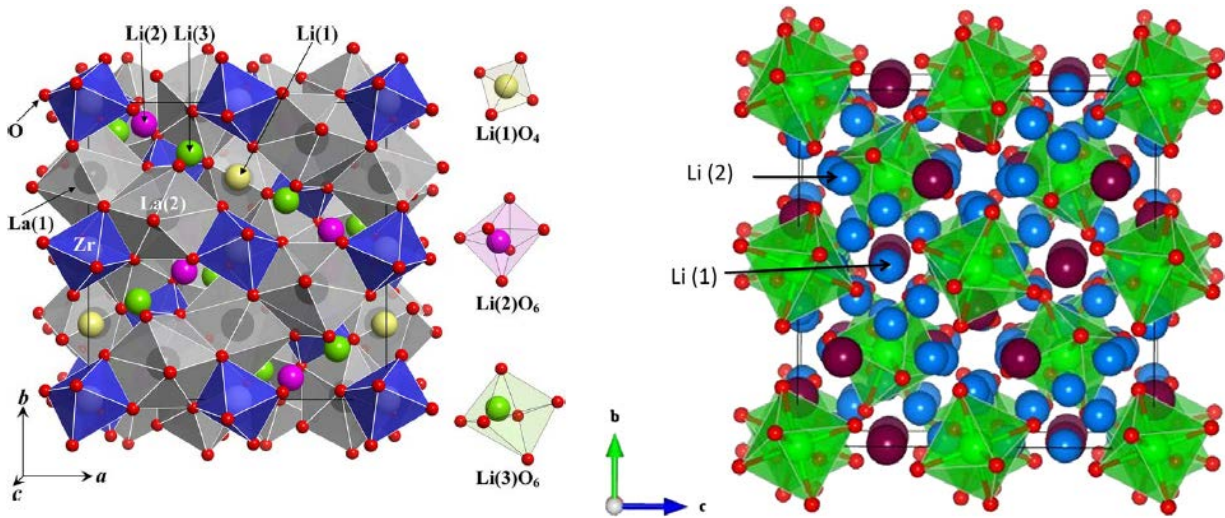
Figure 2-4 Crystal structure of A) tetragonal $Li_7La_3Zr_2O_{12}$ [111] and B) cubic $Li_7La_3Zr_2O_{12}$

(Blue balls represents Li, purple balls Zr, green balls La, red balls oxygen atoms) [134]

The garnet-like structured solid electrolyte material LLZO has also attracted much attention due to its high Li ionic conductivity ($> 10^{-4}$ S cm^{-1} at room temperature), and more importantly, the stability versus lithium anode [19, 135, 136]. It was found that there is no visual and XRD pattern change when LLZO pellets come in contact with molten Li metal for 72 hours [19]. LLZO has two types of crystallization structure by different modifications at different temperatures, a tetragonal form (t-LLZO) and a cubic form (c-LLZO) [111, 137, 138]. The cubic form has a significantly higher conductivity compared with the tetragonal structure LLZO, which is ~10^{-4}S cm^{-1}. Figure 2-4 is the crystal structure of tetragonal LLZO.
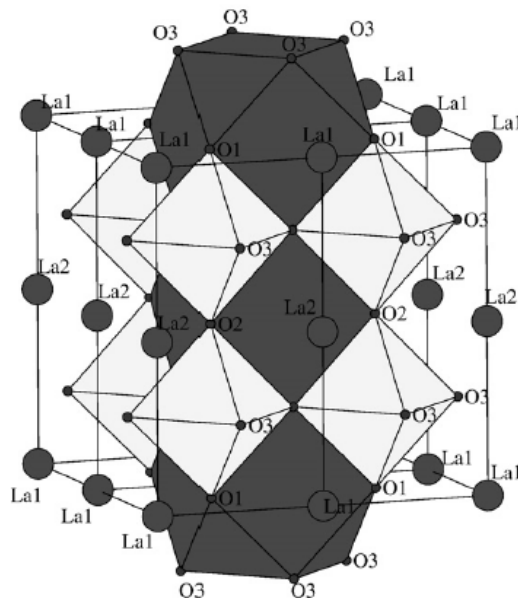
Figure 2-5 Crystal structure of tetragonal $Li_{3x}La_{2/3-x}TiO_3$ [139]

The perovskite $La_{0.51}Li_{0.34}TiO_{2.94}$ was first synthesized by Inaguma [101]. It has potential as a candidate for bulky type or thin-film all-solid-state lithium ion batteries. Researchers find it has good bulk conductivity and compatibility with cathode materials [139-142]. Its main drawback is its relatively low grain-boundary resistance. Figure 2-5 is the crystal structure of $Li_{3x}La_{2/3-x}TiO_3$.

Compared to NASCON and garnet-type electrolytes, the lithium sulfide electrolytes seem to have higher conductivity. A high conductivity of $\sim 10^{-3}$ S cm^{-1} was reported. Those inorganic electrolytes have great potential for ASSLIBs fabrication. However, they are unstable when in contact with moisture or oxygen [143], so special care should be taken during synthesis and storage of those electrolytes.

Ionic migration in crystal is driven by thermal activated hopping of ions between interstitial and vacant sites [120]. For vacancy diffusion, atom interchanges from a normal lattice position to an adjacent vacant lattice site. The extent of vacancy diffusion is controlled by the concentration of these defects and the direction of the vacancy motion is opposite to the direction of the diffusing

atoms. The atoms must have enough energy to overcome the activation energy barrier to reach the vacancy. For interstitial diffusion, the interstitial atoms which has enough energy can squeeze past neighbor atoms and reach a new interstitial site. The magnitude of the diffusion coefficient D^T is the indictor of the rate at which the atoms diffuse. Normally temperature has a profound effect on the diffusion coefficient magnitude, and this was empirically expressed using Arrhenius relation as follows [144],

$$D^T = D_0{}^T \exp(-\frac{E_A}{k_B T})$$
Eq. (2-6)

where D^T is the tracer diffusion coefficient (m^2 s^{-1});

E_A is the activation energy for the mass transport (j mol^{-1});

$D_0{}^T$ is the pre-exponential factor;

k_B is the Boltzmann constant (J K^{-1});

T is the temperature (K);

From the microscopic point of view, the tracer diffusion coefficient can be defined using Einstein-Smoluchowski relation,

$$D^T = \lim_{t \to \infty} \frac{\langle r^2(t) \rangle}{2dt}$$
Eq. (2-7)

where $\langle r^2(t) \rangle$ is the mean square displacement of the particles after the time t and d is the dimensionality of the movement. The atom jumps between the minima in a potential landscape, which are lattice sites or interstitial sites. The mean jump time is much short compared to the mean residence time τ. D^T can be expressed by,

$$D^T = fD^{uc} = f\frac{l^2}{2d\tau}$$
Eq. (2-8)

D^{uc} is the uncorrelated jumps diffusion coefficient, f is the correlation factor, which equals unity if the jump behavior is uncorrelated. The relationship between ionic dc conductivity and the diffusion coefficient can be related by Nernst-Einstein equation,

$$D^\sigma = \frac{\sigma_{dc} k_b T}{N q^2}$$
Eq. (2-9)

where N is the particle density of the charge carriers, q is their charge. $D^T = H_R D^\sigma$, H_R is the Haven ratio, which reflects the ratios of various charge carriers contributing to the total conductivity. Considering that for most lithium ion conductive ceramic (e.g., LATP), lithium ion is the only charge carrier which jump randomly, so $D^\sigma = D^T = D^{uc}$[144].

The lithium ion transport mechanism in $LiTi_2(PO_4)_3$ at atomic scale was examined experimentally [145] and modeled using density functional theory [120]. The lithium ion mobility was also analyzed in $Li_{1+x}Ti^{4+}_{2-x} R^{3+}_x(PO_4)_3$ compounds (x = 0.2 and R^{3+} = Al^{3+}, Ga^{3+}, Sc^{3+}, and In^{3+}) by nuclear magnetic resonance technique (NMR) and impedance spectroscopy. It was found that all of the compounds display the rhombohedral symmetry, and in all cases the trivalent cations were incorporated into the NASICON framework [146]. Lithium ion transportation was also analyzed using the difference bond-valence approach and experimental 3D lithium diffusion pathway in LATP was extracted from the negative nuclear density maps reconstructed by the maximum entropy method [121].

The mathematic modeling of the all-solid-state lithium ion batteries which involves the microscope mass and charge transport in solid electrolytes was also carried out [147]. The Nernst-Planck equation was used to describe the motion of ions in the solid electrolyte. The general form of the Nernst-Planck equation is:

$$J_{Li^+} = -D_{Li^+} \frac{\partial a_{Li^+}}{\partial y} + D_{Li^+} \frac{F z_{Li^+}}{RT} a_{Li^+} E$$
Eq. (2-10)

where

J_{Li^+} (y, t) is the flux of Li^+ at a distance y from the surface of the anode at time t (mol m^{-2}s^{-1})

(y=0 at the interface of anode and electrolyte);

a_{Li^+} is the activity of Li^+ (mol m^{-3});

D_{Li^+} is the diffusion coefficient of Li^+ (m^{2}s^{-1});

$\frac{\partial a_{Li^+}}{\partial y}$ is the concentration gradient (mol m^{-4});

E is the potential gradient (V m^{-1});

z_{Li^+} is the valence of Li^+.

The two terms at the R.H.S of Eq. (2-10) is the diffusion and migration of lithium ion flux. Combining with the charge transfer kinetics, diffusion of lithium ion in the intercalation electrodes, the charge/discharge properties of the batteries can be modeled.

2.4   Gel-type Polymer Electrolyte

The gel-type polymer electrolytes (GPEs) were also called plasticized polymer electrolytes. GPEs are made by the impregnation of a liquid electrolyte plasticizer (e.g., propylene carbonate (PC), ethylene carbonate (EC), diethyl carbonate (DEC) and polyethylene glycol (PEG)) and lithium salt in the polymeric host materials. Its ionic conductivity is comparable to the conductivity of a liquid electrolyte at room temperature. Various types of GPEs were explored in the literature, generally based on poly(vinilidene fluoride) (PVdF) [148], PMMA[149,150], PVdF-HFP [151], PAN/PEGDA/PVP [152], PVC [153], and PVS [154]. It was found that the conductivity of those GPE systems can be affected by lithium salt types and content [155-157], host polymer materials, solvent types and ratios [158, 159]. The copolymer poly(vinylidene fluorideco-hexafluoropropylene) (PVdF-HFP) has been widely investigated due to its appealing comprehensive properties. For example, it provides greater ionization of salt, liquid electrolyte entrapping abilities, good mechanical strength, high solubility, and a lower crystallinity and glass

transition temperature, etc. [50, 148, 160]. However, because of the leaching of liquid from the membrane and the chemical reaction of fluorinated polymers with lithium, which results in the formation of LiF, the PVdF-based GPEs still suffer from a lack of stability with time [161]. Table 2-4 is a literature review of the different types of gel-type polymer electrolytes.

Table 2-4 Literature review on the different types of gel-type polymer electrolytes

Host polymer	Solvent (plasticizer)	Lithium salt	Conductivity	T (°C)	Ref.
PVdF-HFP	PC+EC	$LiN(CF_3SO_2)_2$	1.74×10^{-3}	R.T.	[148]
PMMA	PC+EC	$LiClO_4$	6.08×10^{-3}	R.T.	[149]
PMMA	PC+EC	$LiN(CF_3SO_2)_2$	6.16×10^{-3}	R.T.	[149]
PVdF-HFP + PVP	DMC+EMC+EC	$LiPF_6$	0.49×10^{-3}	R.T.	[152]
PvDF	PC	$LiN(CF_3SO_2)_2$	1.74×10^{-3}	30	[154]
PVS	PC	$LiN(CF_3SO_2)_2$	1.94×10^{-4}	30	[154]
PVdF-HFP	PC+EC	$LiCF_3SO_3$ $LiClO_4$ $LiBF_4$	$\sim 1 \times 10^{-3}$	R.T.	[156]
PMMA	γ-butyrolactone	Mixed $LiClO_4$ and $LiCF_3SO_3$	9.02×10^{-3}	R.T.	[157]
PVC	PC	$LiClO_4$	0.9×10^{-3}	20	[158]
PVC	PC	$LiN(CF_3SO_2)_2$	1.2×10^{-3}	20	[158]
PVdF-HFP	PC	$LiBF_4$	2.1×10^{-3}	R.T.	[160]
P(AN-*co*-LiMA)	EC	$LiClO_4$	1.9×10^{-3}	R.T.	[162]

2.5   Solid Electrolyte Optimization

2.5.1   Ceramic in Polymer Composite Electrolytes

An ideal electrolyte layer should satisfy the following rigorous demands: 1) High Li+ ion conductivity and transference number; 2) High electrochemical stability with lithium metal anode; 3) Sufficient mechanical strength to suppress lithium dendrite formation; and, 4) The ability to accommodate the volume change of electrodes, especially for lithium metal anodes, to minimize the capacity drop during cycling. Using the existing electrolyte materials, many researchers have tried different ways to develop novel kinds of composite electrolytes in order to optimize their performance.

One composite electrolyte developed is the ceramic-in-polymer electrolyte. It has been claimed that adding ceramic fillers to SPEs or GPEs could stabilize the interface between electrolytes and lithium metal [163], enhance the mechanical properties [76] and also improve the conductivity and lithium ion transference number [49, 164]. Different types of fillers, the particle size of fillers, and the wt% content of the filler were widely investigated by several research groups. It was also found that the existence of ceramic filers was not only beneficial for SPEs [165-173], but they also improve the overall performance of GPEs [161, 174-176].

The investigated ceramic fillers include metal oxides (Al_2O_3 [49, 167, 177], SiO_2 [172, 177], TiO_2 [49,173], CeO_2 [169], ZrO_2 [168], Y_2O_3 [165], Sm_2O_3 [170], and MgO_2 [178], etc.), inorganic lithium salts (γ-$LiAlO_2$, Li_2TiO_3, Li_2SiO_3, Li_2ZrO_3, Li_3PO_4, and $LiBO_2$, etc.) [165], ferroelectric ceramics ($BaTiO_3$, $PbTiO_3$, $CaTiO_3$, $SrTiO_3$, and $(LiLa)TiO_3$, etc.) [165], carbon powders [165, 171], shape selective molecular sieves ZSM-5 [166], aluminum oxyhydroxide ($AlO[OH]n$) [151], and lithium ion conductor LATP powers [179], etc.

29
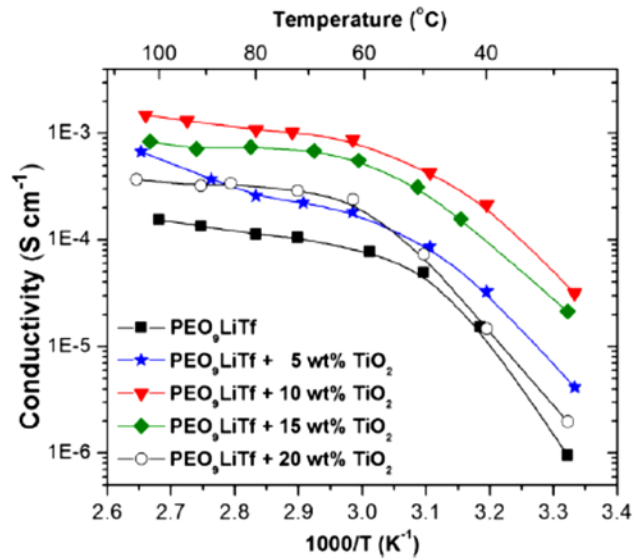
Figure 2-6 Variation of conductivity with inverse temperature for composite polymer electrolytes

(PEO)$_9$-LiCF$_3$SO$_3$ + x wt% TiO$_2$ (x = 0, 5, 10, 15 and 20) [173]

Figure 2-6 is the conductivity variation with an inverse temperature for the composite polymer electrolytes of PEO-LiCF$_3$SO$_3$. We can see that the conductivity of the SPE was enhanced by the TiO$_2$ additive, and when the weight ratio of TiO$_2$ is 10%, the highest conductivity was achieved as 4.9×10^{-5} S cm^{-1}.
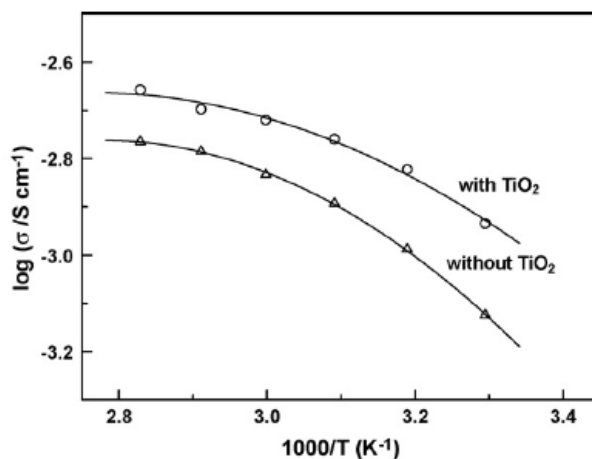
Figure 2-7 Temperature dependence of ionic conductivity on the PVDF-HFP-based polymer

electrolytes without and with TiO$_2$ [176]

Figure 2-7 is the temperature dependence of ionic conductivity on the PVDF-HFP-based polymer electrolytes without and with TiO_2. We can see the addition of TiO_2 fillers is not only effective for SPE systems, but it also obviously improved the conductivity of the PVDF-HFP gel polymer electrolytes.

The ceramic filler's effective role in promoting ion transport was explained by the lewis-acid characters and the high surface area of the fillers [180, 181]. The following assumptions may contribute to enhancing the ionic conductivity of the composite electrolytes system [49, 151, 170, 171]:

1). Lewis-acid type interaction between the polar surface of ceramic fillers with the electrolytic species, can lower the ionic coupling and promote the salt dissociation via an "ion-filler complex" formation;

2). The filler groups can provide physical cross-linking centers for the PEO segments and for the anions, and reduce the tendency for polymer reorganization after the polymer electrolyte experienced the crystalline-to-amorphous transition. Thus, establish the conducting pathways on the surface of the filler particles.
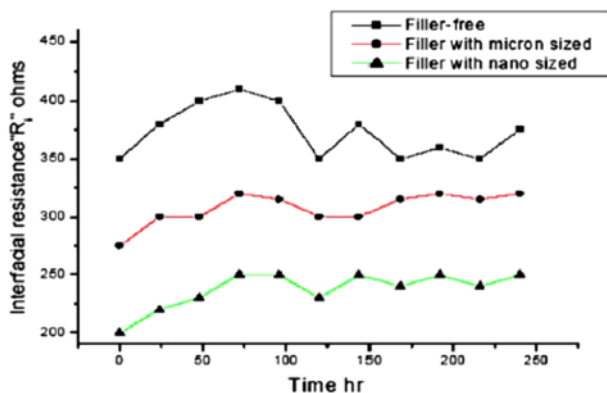
Figure 2-8 The effect of ceramic filler of AlO[OH]n with different size of 7 µm/14 nm on the interfacial resistance between electrolytes [151]

The existence of ceramic fillers can not only improve the ionic conductivity of the bulky composite electrolytes, but also benefit the interface between the lithium metal and composite electrolytes by: 1) decreasing the interfacial resistance and 2) improving the interfacial stability.

Figure 2-8 shows the effect of a ceramic inert filler of AlO[OH]n on the interfacial resistance between lithium metal and PVDF-HFP-LiN(CF$_3$SO$_2$)$_2$ gel-polymer electrolyte. It is obvious that the interfacial resistance values have been reduced upon the addition of an inert filler, and the nano-sized filler exhibits better performance than the micron-sized filler.
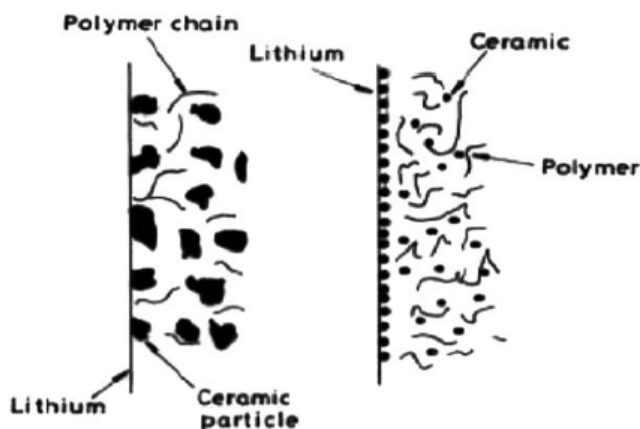
Figure 2-9 Schematic diagram of the interface of lithium with polymer/gel polymer composite electrolyte [182]

The passivation layer on the surface of the lithium anode with an organic liquid electrolyte has been recognized and well-studied by many researchers. Similar to this passive layer, there is also a passivation interface between the lithium metal and solid electrolyte. Figure 2-9 shows the schematic diagram of this lithium-composite electrolyte interface [182]. The inert ceramic particles can minimize the exposed area of lithium metal to the polymer phase, which contains O, OH-species and thus reduce the passivation process. This presumption also explains the better improvement by the nano-sized fillers, since the smaller size particles cover more surface area on the lithium surface.

However, interestingly, some researchers have found that the fillers cannot enhance the conductivity or even bring a counter effect [183-186].

2.5.2 Polymer in Ceramic Composite Electrolytes

Another concept that has been developed in recent years is polymer in ceramic composite electrolytes. It is composed of non-conducting porous material, which is used for mechanical integrity and strength, and a PEO polymer phase interpenetrated with the porous matrix, which is responsible for the ion conduction. The possible explanation for the ionic conductivity enhancement and other interesting phenomena was: 1) The increased interfacial zone of the polymer phase with the non-conducting phase, which is similar to the behaviors of a polymer electrolyte with the nano-size ceramic filler [187], 2) The aligning effect of the anisotropic conducting polymer chains at a molecular level [188], and 3) The effects of the decrease in the glass transition temperature [189]. It was found that the properties of the whole composite electrolyte were related to the material in use, the porosity of the substrate matrix, the pore size, and fabrication method [190].

2.6   Multilayer Solid Electrolyte
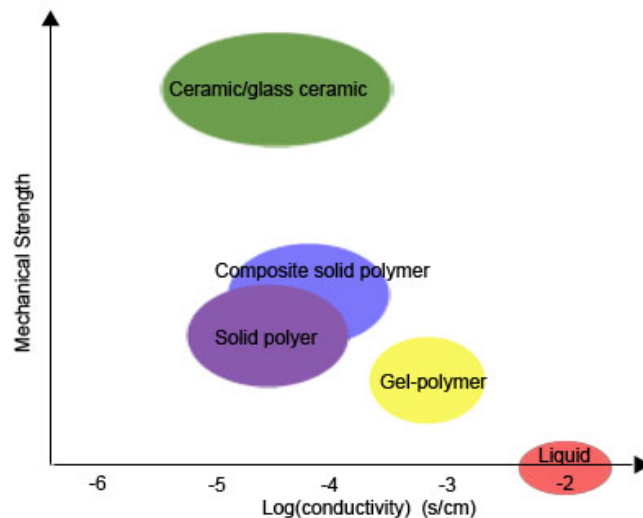
Figure 2-10 Comparison of the conductivity and mechanical strength of different electrolytes

It is not hard to see that the current methods of fabricating composite solid electrolytes have their own limitations. On the one hand, the overall performance improvement of composite electrolytes by a ceramic-in-polymer configuration is still controversial. On the other hand, the polymer-in-ceramic electrolyte needs nano-scale fabrication technology, which will limit its application in industry mass production.

So, we tried to develop a novel solid electrolyte with a multi-layered configuration, which can integrate the benefits of different materials, be fabricated conveniently, and also simultaneously meet the following requirements: 1) Can block, prevent or suppress the lithium dendrite growth when lithium metal is applied as an anode material, 2) Has adequate conductivity, and 3) Can alleviate the volume change effect of the electrode.

Based on the current polymeric/glass-ceramic/ceramic materials, the multi-layer concept will utilize a manifold fabricating method, for example, dip-coating, hot-pressing, and spray-coating, etc., to produce a solid self-standing electrolyte film to maximally optimize its physiochemical and electrochemical performance and address the current problems mentioned previously.

Among the properties of a multi-layer solid electrolyte, the interface resistance between the ceramic and polymeric phase is one of the most critical issues. Very limited research has been carried out in this area, and the results are contradictory.
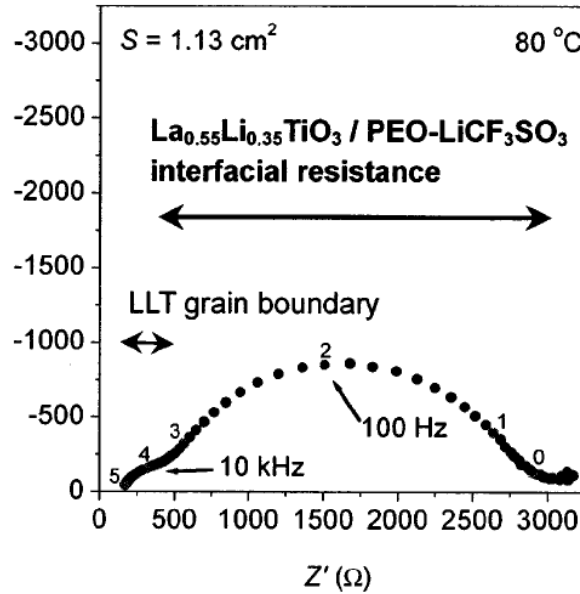
Figure 2-11 Impedance characterization at the interface of $La_{0.55}Li_{0.35}TiO_3/PEO_{10}$-$LiCF_3SO_3$

[191]

In order to understand the lithium ion transportation mechanism at the interface of the polymer electrolyte with ceramic phase filler particles, Takeshi Abe et al. [191] investigated the lithium ion transfer at the interface of the ceramic $Li_{0.35}La_{0.55}TiO_3$ and polymer PEO_{10}-$LiCF_3SO_3$ polymer electrolyte. Figure 2-11 shows the interfacial resistance between $La_{0.55}Li_{0.35}TiO_3/PEO_{10}$-$LiCF_3SO_3$, which was dominant for the total resistance. The activation energy barrier at the interface was as high as 97.6 kJ/mol, which was much higher than the activation energy of the lithium ion transport in PEO_{10}-$LiCF_3SO_3$ polymer and $La_{0.55}Li_{0.35}TiO_3$ bulk grain or grain boundary. And also, the activation energy remained the same at the temperature region above and below the melting point of polymer electrolytes. The author concluded that the polymer electrolyte may have a different structure at the solid/solid interface compared with the bulk region.

35
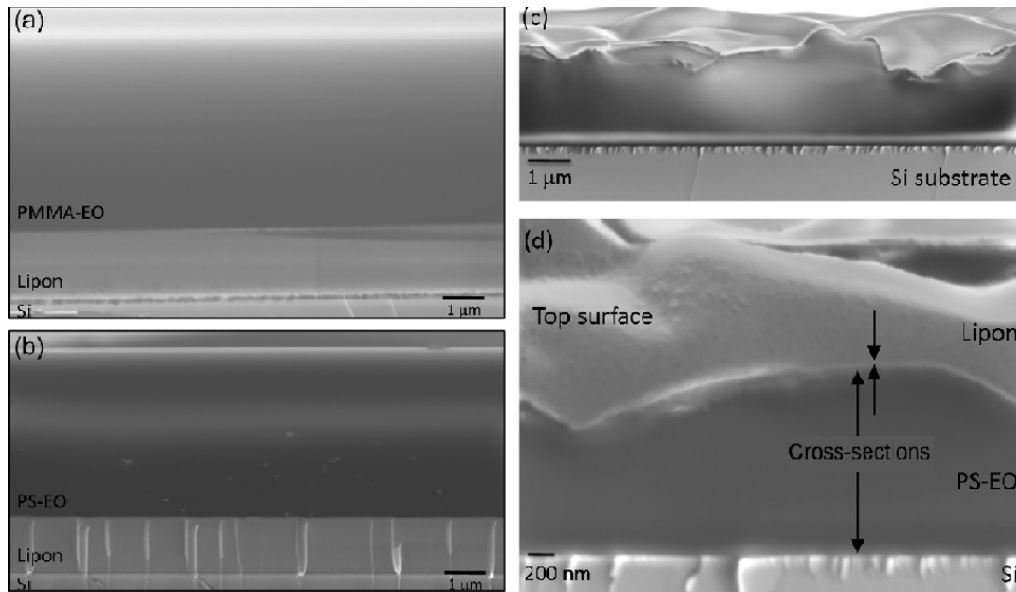
Figure 2-12 SEM image of cross-section of a) PMMAEO-on-Lipon, (b) PS-EO-on-Lipon and c,

d) Lipon-on-PS-EO [46]

Tenhaeff et al. [46] investigated the interfacial resistance between glass-type lithium phosphorous oxynitride (Lipon) and a polymer system of poly(methyl methacrylate-co-poly(ethylene glycol) methyl ether methacrylate) (PMMA-EO) and poly(styrene-co-poly(ethylene glycol) methyl ether methacrylate) (PS-EO), where $LiClO_4$ was applied as lithium salt. They found that the bilayer fabrication method played a determinative role for the interfacial resistance. When the polymer phase was coated on a pre-deposited Lipon layer, a significant interfacial resistance, which dominates the ionic transport of the multi-layer electrolyte, can be observed. However, when Lipon was deposited on top of the polymer electrolyte, the interfacial resistance was eliminated. Figure 2-12 is the SEM image of cross-section of a) PMMAEO-on-Lipon, (b) PS-EO-on-Lipon and c, d) Lipon-on-PS-EO. We can see the contact between polymer and Lipon is intimate, and no obvious gap or void was observed. The author concluded that the interfacial resistance may not solely related to contact issue. Though the origin of the interfacial resistance was not identified, it was suggested that the polymer structure modification might play

36

an important role. The author also found that exposure of Lipon to the solvent mixtures of acetonitrile/N,N-Dimethylformamide (NMP) and acetonitrile/anisole did not affect its conductivity.
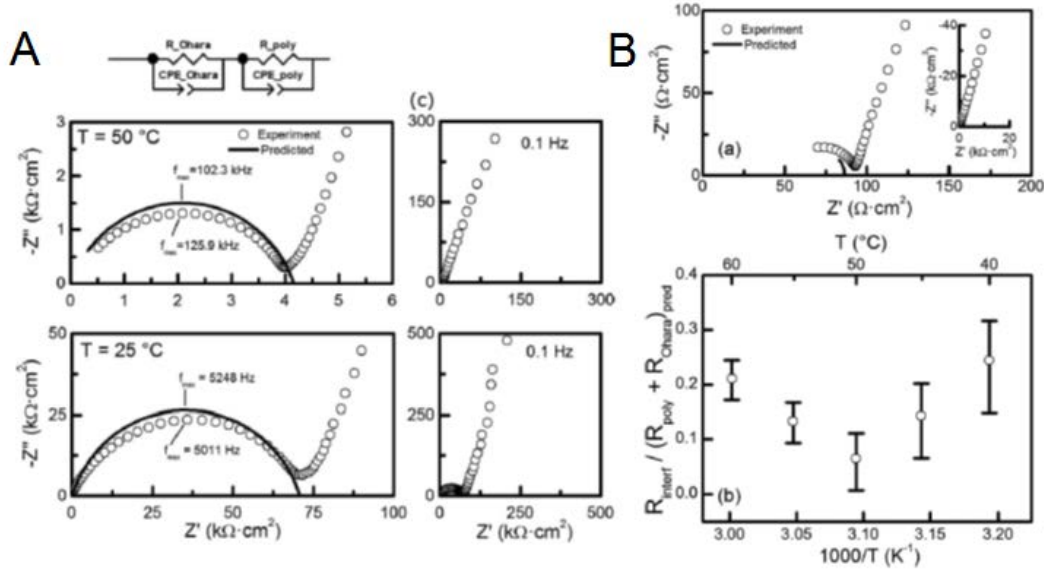
Figure 2-13 Impedance characterization of between A) PEO_{16}-$LiCF_3SO_3$ B) PEO_{10}-LiTFSI and Ohara glass ceramic [17]

In the other paper by Tenhaeff et al. [17], the impedance characterization was carried out at the interface between PEO_{16}-$LiCF_3SO_3$, PEO_{10}-LiTFSI and lithium ion conductive Ohara glass ceramic ($Li_{1+x+y}Al_xTi_{2-x}Si_yP_{3-y}O_{12}$). The polymer electrolyte was fabricated by hot pressing. It was found that the resistance existing at the interface is negligible. At 40 °C, the interfacial resistance provides the largest relative contribution of 24% of the total resistance of Ohara and PEO_{10}-LiTFSI electrolyte. Figure 2-13 shows the impedance characterization at interface of A) PEO_{16}-$LiCF_3SO_3$ B) PEO_{10}-LiTFSI and Ohara glass ceramic respectively [17].

2.7   Conclusion and Research Goals

The objective of the project is to investigate the feasibility of constructing a multi-layer structure composite solid electrolyte for all-solid-state lithium ion batteries. The detailed research goals include the following:

1).Before the multi-layered all solid electrolytes are built, the physiochemical and electrochemical properties of the single phase solid electrolyte must be investigated. The PEO based polymer electrolyte and the gel-type polymer electrolyte (e.g., PVdF-HFP-based GPEs) with commonly used lithium salt (e.g., LiTFSI) and a ceramic (or glass ceramic) electrolyte (e.g., LATP, LLZO, LLT) will be synthesized, fabricated, and characterized. This study will experimentally investigate the fabrication method or synthesis route of the polymer or ceramic ion conductor materials with the aim to improve or optimize those processes.

2). From the literature review, we found that there is a specific ionic transport mechanism that exists at the interface of polymer electrolyte and ceramic fillers. Also, the controversial viewpoint of the existence of an interfacial impedance at the laminated bilayer suggests that the interfacial impedance may be related to material selection (ceramic material, and also polymer-LiX material), fabrication method, lamination protocol and environmental factors (e.g., temperature). Obviously, more experimental research has to be conducted to find how those parameters can influence the interfacial resistance of the laminated solid electrolyte. Our research will fabricate, construct and examine the multilayer solid electrolyte based on various materials, to seek the optimal solution for a versatile electrolyte layer that is able to satisfy the multiple requirements of ASSLIBs.

3). Based on all of the previous work, our final goal is to develop, characterize and optimize the all-solid-state lithium ion batteries of coin cell type with multilayer composite electrolyte

architecture. The cell impedance, charge/discharge properties at various temperatures should be characterized and analyzed.
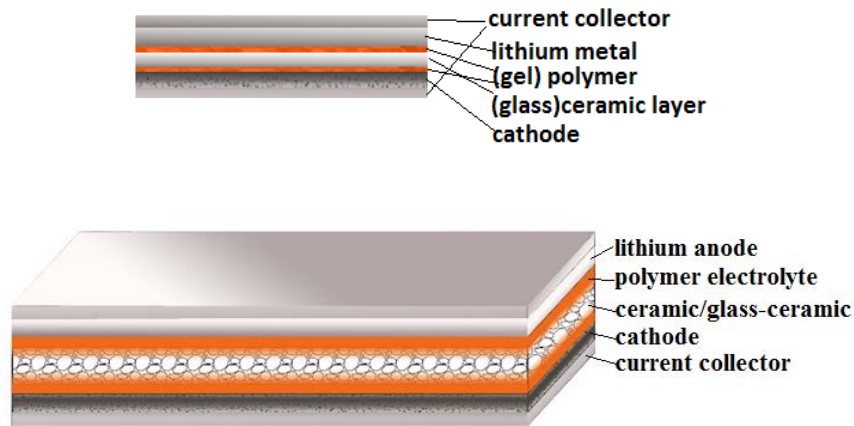
Figure 2-14 Schematic structure of the ASSLIBs with multilayer/composite electrolyte

Figure 2-14 is the schematic structure of the ASSLIBs using multilayer/composite electrolyte which will be fabricated using the existing ceramic/polymer material. Lithium metal will be used as anode. The ceramic electrolyte can be fabricated with/without the pore-makers at different temperature, thus different density and porosity can be achieved.
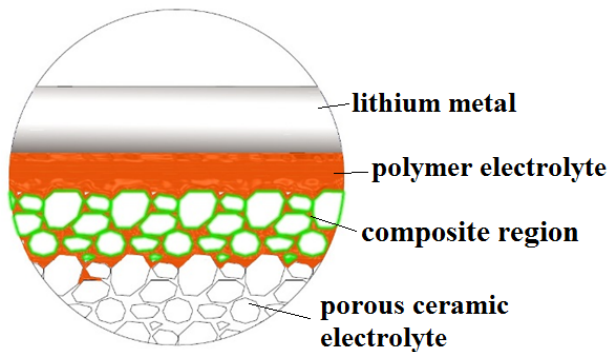
Figure 2-15 Configuration of the polymer-in-ceramic structure electrolyte with ceramic bulk body filled with polymer electrolyte in micro-channels

Figure 2-15 is the schematic configuration of the polymer-in-ceramic structure composite electrolyte, which is composed of two phases, 1). Lithium ion conducting ceramic with micro or nano-scale pores or channels geometry; 2). Flexible polymer phase penetrated in the pores or

channels. The previous works all relied on the non-conducting ceramic material for building the porous matrix. Here we propose a possible fabrication route with conductive ceramic material. By designing with the structure and fabrication method, a composite or hybrid electrolyte by confining polymer electrolyte in the pores of the ceramic substrate may be developed.

Chapter 3 Ceramic Electrolyte Synthesis and Characterization

3.1   Introduction

To fabricate a multilayer electrolyte with ceramic electrolyte and polymer electrolyte, we have to synthesize, fabricate and characterize the ceramic electrolyte first. From the literature review, we have chosen the LATP, LLT and LLZO ceramic electrolyte as our research objective. Based on the existing knowledge on those different types of ceramic electrolyte, we tried to experimentally explore the complete processes, including material synthesis, sample preparation and electrochemical characterizations of those different ceramic electrolytes. Our goal also includes the possible improvement and optimizations.

Although there are already many researches on those ceramic electrolytes as we have discussed in Chapter 2, the synthesis of those ceramic materials varies by different start materials, sintering temperature, synthesis route and so on. So far, we did not see report on the effect of sintering temperature on the relative density/conductivity of LATP through solid-state reaction method. We have tried to synthesize the same material by different methods, and sintering temperature, and then comprehensively compared the performances in different aspects, for example, their relative density variation, conductivities under different temperature and pressure, and also their stabilities in organic solutions.

To verify the feasibility of polymer-in-ceramic concept composite electrolyte, porous LATP pellets were fabricated and sintered using different pore maker agent. The microstructure of porous LATP was observed through SEM images.

3.2   Experimental Methods

3.2.1   Material Synthesis

3.2.3.1 LATP Synthesis

$Li1_{.3}Ti_{1.7}Al_{0.3}(PO_4)_3$ has superior conductivity among the NASICON-type lithium ion conductors. The synthesis route of LATP material can be classified as solid-state reaction [179, 192] and sol-gel [124-126, 193] method, which varies with starting materials and process factors. It was reported that the conductivity was $\sim 10^{-4}$ S cm^{-1} and 1.5×10^{-5} S cm^{-1} for the solid-state reaction and sol-gel made materials [123]. In our experiments, LATP material was synthesized using solid-state reaction method as follows:

Stoichiometric mixture of high purity chemicals were used, including Li_3PO_4 (Sigma-Aldrich, >99.9%; 10 wt% excess was added to compensate for the loss of lithium during annealing), Al_2O_3 (Sigma-Aldrich, >99.99%), and TiO_2 (Aldrich, >99%), $(NH_4)H_2PO_4$ (Sigma-Aldrich, >99.7%). The starting material mixture was heated at 120 °C in a vacuum oven for three hours to remove all the moisture.

Then the mixture of powder was mixed with pure ethyl alcohol (Sigma-Aldrich, >99.5%), the slurry was poured into zirconia jars and was grounded for 18 hours in a high-energy planetary ball mill with zirconia balls as grinding material. The well-prepared slurry was then air-dried and sintered inside aluminum crucible at 900 °C for 2 hours. Then the ceramic product was ball milled again for another 12 hours. After a dry-process in oven at 150°C, fine white powder was finally obtained finally. The powder was pressed to pellets at 450 MPa, and then sintered at temperature from 850 -1150 °C for 6 hours. The heating rate is 3°C /min.

3.2.3.2 LLZO Synthesis

$Li_7La_3Zr_2O_{12}$ was synthesized in solid-state reaction route. First, a stoichiometric mixture of reagent grade starting materials Li_2CO_3 (Fisher, >99.9%), La_2O_3 (Sigma-Aldrich, >99.9%), ZrO_2 (Sigma-Aldrich, >99%) powders was dried to remove any moisture or other absorbents. The La_2O_3 was dried at 1150 °C for 6 hours to remove absorbed H_2O and CO_2, Li_2CO_3 and ZrO_2 was dried at 600°C for 6 hours. After the mixture of powder was ball milled with zirconia balls in ethanol in air for 24 hours, the slurry was dried in oven at 250 °C to obtain fine white powder, which was then pressed at 250 MPa to obtain pellets. Then the pellets were sintered in an oven at 900 °C for 6 hours and then at 1150°C for another 6 hours in a zirconia crucible. After that, the pellets were crushed to powder in an agate mortar and then ball milled again for 8 hours. After another dry treatment in a forced air convection oven at 250 °C, the obtained fine powder was pressed as pellets and annealed at 1230 °C for 36 hours.

3.2.3.3 LLT Synthesis

$Li_{0.5}La_{0.5}TiO_3$ was prepared from reagent grade of La_2O_3 (Sigma-Aldrich, >99.5%), Li_2CO_3 (Sigma-Aldrich, >99.5%, 10 wt% excess was added to compensate for the loss of lithium during annealing), and TiO_2 (Sigma-Aldrich, >99%) molar ratio of 1.1:1:2. The La_2O_3 was dried at 1150 °C, TiO_2 and Li_2CO_3 was dried at 600 °C for 6 hours respectively before use. The mixture of powder was ball milled in ethanol with zirconia balls for 18 hours with a high energy planetary ball mill machine. The slurry then was dried in the oven at 250 °C to obtain fine white powder, which was further pressed at 250 MPa to obtain pellets. Those pellets were sintered at 800 °C for 4 hours and at 1180 °C for 6 hours. After that the pellets was ball milled again for 8 hours in ethanol. After dried again, the powder was pressed at 450 MPa and obtained pellets were annealed at 1050 -1350 °C for 6 hours.

3.2.2 Sample Fabrication

Using the synthesized ceramic materials, the samples of ceramic ion conductor were fabricated in different ways: 1) dry pressing, 2) tape casting.

Dry pressing is an economic and more efficient method to fabricate the laminated thin layers by ceramic powders in both simple and complex geometries. It is widely used in manufacturing insulating parts, capacitors, electro-ceramics, electrodes of fuel cells, and other functional ceramic substrate. The common dry pressing operation is performed on a hydraulic pressing machine with a die. The powder can be placed inside a die between two rigid punches of the pressing machine, and the uniaxial pressure was applied on the die, thus the powders can be pressed tightly.

If the pressing process is conducted at increased temperature it is called hot pressing. Hot pressing permits obtaining better compaction, higher green compact density and higher strength of the part. In our ceramic solid electrolyte sample fabrication, the die pressing was carried out at room temperature. For the polymer solid electrolyte sample fabrication, hot pressing was applied since the polymer material is easier to shape at elevated temperature.
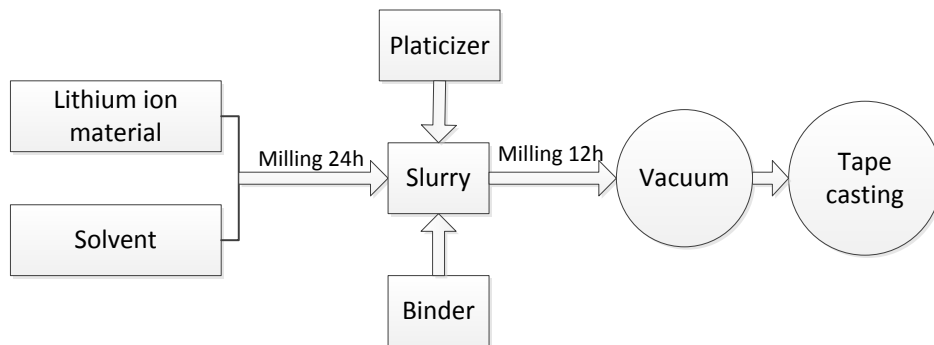
Figure 3-1 Schematic process of tape casting of lithium ion ceramic conductors

Tape casting is a widely used production process in the manufacture of thin tapes from slurry. Due to its low cost, high reliability and ability of mass production, tape casting technology has been widely used to prepare thin film planar ceramics or polymer membranes, for example, solid

oxide fuel cells (SOFCs) and electrode/electrolyte of lithium ion battery, lithium-air battery, etc. In a tape casting process, the slip or slurry is poured into a puddle or reservoir behind the doctor blade, and the carrier to be cast upon is set in motion. The doctor blade gap between the blade and the carrier defines the wet thickness of the tape being cast. Other variables that play roles include: reservoir depth, speed of carrier movement, viscosity of the slop, and shape of the doctor blade. The wet film of slip passes into a drying chamber of some sort and the solvents are evaporated from the surface, leaving a dry tape on the carrier surface. The electrode/electrolyte fabrication of LIB through tape casting is illustrated in the figure 3-1.

The feasibility of fabricating LATP ceramic plates with tape casting method was also investigated. In our research, ethanol and toluene as the solvent, polyvinyl butyl (PVB) as the binder, blown menhaden fish oil as the surfactant, butyl benzyl phthalate (BBP) and polyethylene glycol 400 (PEG400) as plasticizers. The slurry was prepared by two ball milling stages. Firstly, the LATP powders was dissolved in ethanol and toluene solvent with blown menhaden fish oil added as surfactant. This slurry was then ball milled for at least 24 hours. Then, at the second stages, more solvent of ethanol was added, PVB, BBP and PEG400 was also added to form the final slurry. This slurry was then ball milled again for another 12 hours. In the table 3-1, the ratio (wt%) of each composition at stage 1 and stage 2 was listed.

Table 3-1 Ratio of composition (wt%) at different stages for LATP ceramic fabricated by tape-casting

Stages	Slurry Component	Composition	Ratio (wt%)
Stage 1	Ceramic powder	LATP powder	64.0
	Solvent	Ethanol	1.6
		Toluene	16.0

	Surfactant	Blown Menhaden Fish Oil	1.2
	Binder	Polyvinyl Butyral (PVB)	3.8
Stage 2	Solvent	Ethanol	9.6
	Plasticizer 1	Butyl Benzyl Phthalate (BBP)	1.9
	Plasticizer 2	Polyethylene Glycol (PEG400)	1.9

The height of the doctor blade was controlled as 400 μm. The thickness of the green tape is ~1-1.5mm. After tape casting, the green tape is left at room temperature to evaporate the volatile solvents. Sample plates with different shape and dimension are cut by a punch cutter. Then the plates were sintered at 1050 °C for 6 hours.

The porous LATP was fabricated through adding different pore maker materials with various ratios. Before drying pressing, the LATP fine powder was thoroughly mixed with pore maker in an agate crucible. In this study, the pore maker materials were explored including PMMA, PVA, and PVB powders.

3.2.3 Phase Structure and Morphology

The structure characterization is performed using X-ray diffraction (XRD) with Cu Kα radiation over a 2θ range from 10-80º at room temperature. The increment angle was 0.04° and dwell time was 5 seconds. The morphological features of the prepared membranes were examined using the Scanning Electron Microscopy (SEM, QUANTA-2000).

3.2.4 Relative Density Measurement

The density of the pellets ρ_{exp} was determined via Archimede's method on high accurate balance. The theoretical density of a material ρ_{th} was calculated from the atomic weight and crystal structure.

$$\rho_{th} = \frac{N_c W_A}{V_c N_A}$$ Eq. (3-1)

where N_c is number of atoms in unit cell, W_A is Atomic Weight [kg mol^{-1}], V_c is Volume of unit cell [m^3], N_A is Avogadro's number [atoms mol^{-1}]. Here, a theoretical density of 2.92 g cm^{-3} was calculated for LATP when x = 0.3, assuming a phase-pure material [127].

The relative density was calculated by $\rho_{rd} = \rho_{exp}/\rho_{th}$.

3.2.5 Electrochemical Impedance Spectroscopy Characterization

Electrochemical Impedance Spectroscopy (EIS) is a powerful tool to study the complex electrochemical processes at electrodes and interface. EIS is usually measured by applying a small amplitude ac potential perturbation to an electrochemical cell, changing the AC frequency and measuring the current through the cell. The EIS analysis can qualitatively determine the information such as electronic/ionic conduction in electrode/electrolyte, charge transfer kinetics at interface, interfacial charging effect at the surface films or the interfacial double layer. The EIS was widely applied on electrochemistry studies of lithium ion batteries, proton exchange membrane fuel cells (PEMFCs) and SOFCs and etc. [194-198].
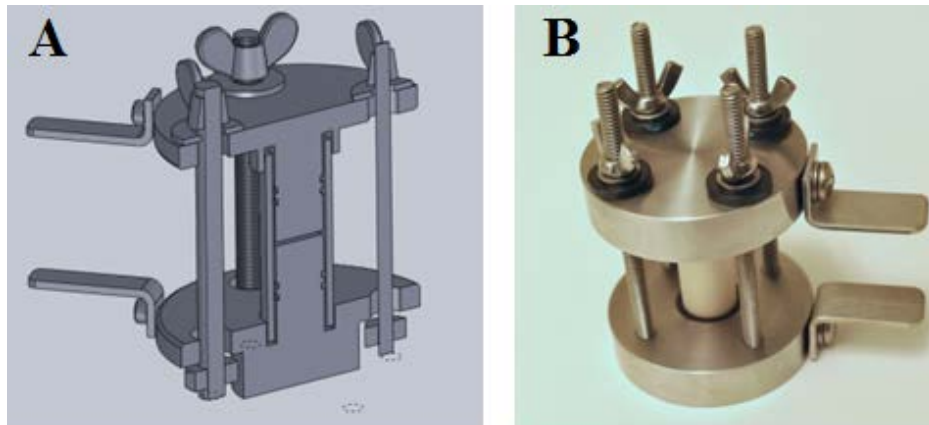
Figure 3-2 Testing cell with SS blocking electrode: A) 3D model; B) Physical view

To characterize the ionic conductivity and the interfacial resistance of electrolyte by EIS, first, a testing cell for the ionic conductivity measurement was designed and assembled. Figure 3-2 is

the testing cell design with 2D design drawing, 3D model and physical view. The diameter of the stainless steel (SS) rod is 13 mm; the inner diameter of the Al_2O_3 tube is 14.29 mm. The tube was sealed by two O-rings and vacuum grease. The four threaded rods can provide uniform force to make sure of the intimate contact of the blocking electrode and the sample.

The electrochemical properties were characterized by AC impedance spectroscopy using a Solartron impedance/gain-phase analyzer 1260 and an electrochemical interface 1287. The analysis of impedance spectra is performed in terms of Nyquist plots where the imaginary part of the impedance is plotted as a function of the real part over a wide range of frequencies, for example, a frequency from 0.1 Hz-1 MHz at the AC voltage of 10 mV.

First, a symmetric cell was fabricated by sandwiching Pt (or gold) coated electrolyte samples between the SS blocking electrodes. To measure the impedance at different temperature, the testing cell was placed inside a tube furnace. Prior to each impedance measurement, the testing device was equilibrated for 1h at each temperature.

3.2.6   Stability of LATP Ceramic Electrolyte

The stability of LATP in the aqueous solution with various lithium salt, include LiOH, LiCl, $LiNO_3$ and $LiCOOCH_3$, was investigated by Spencer, et al [124]. Since our aim is to fabricate multi-layer electrolyte with LATP ceramic, so the stability of LATP material with the organic solvent was explored in this research.

We use the EIS measurement as the indicator of the electrochemical stability of LATP. The EIS plot was compared with the same LATP ceramic sample before and after it was soaked in organic solvent for a specific time. ACN and lithium ion conductive solvent which is composed of LiTFSI + DMC + EC as the solvent was used respectively.

3.3 Results and Discussion

3.3.1 Phase Structure and Morphology
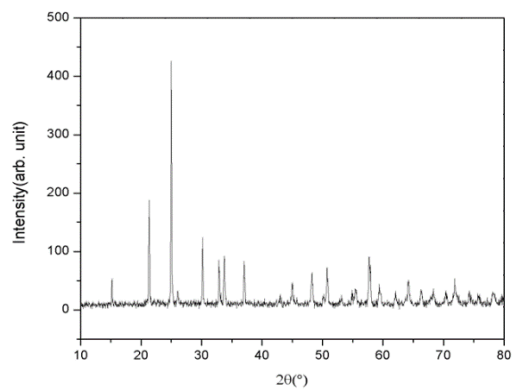
Figure 3-3 XRD pattern of $Li_{1.3}Al_{0.3}Ti_{1.7}(PO_4)_3$
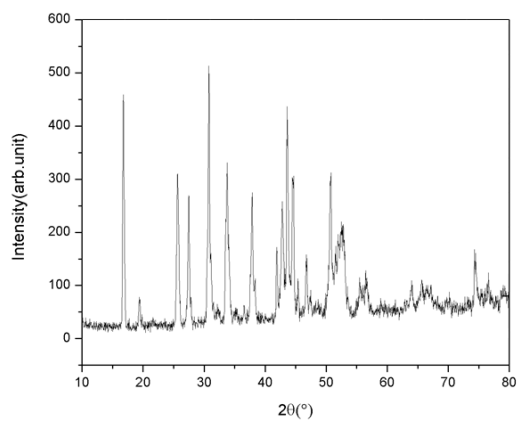
Figure 3-4 XRD pattern of $Li_7La_3Zr_2O_{12}$
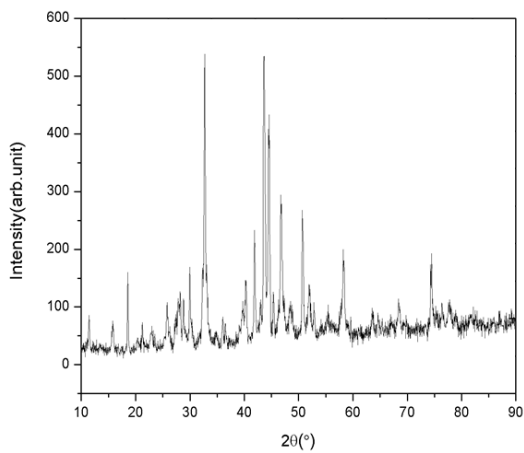
Figure 3-5 XRD pattern of $Li_{0.5}La_{0.5}TiO_3$

Figure 3-3, figure 3-4 and figure 3-5 are the XRD pattern of $Li_{1.3}Al_{0.3}Ti_{1.7}(PO_4)_3$, $Li_7La_3Zr_2O_{12}$, and $Li_{0.5}La_{0.5}TiO_3$ respectively. Compared with the reference, we can find good agreement of the synthesis materials.
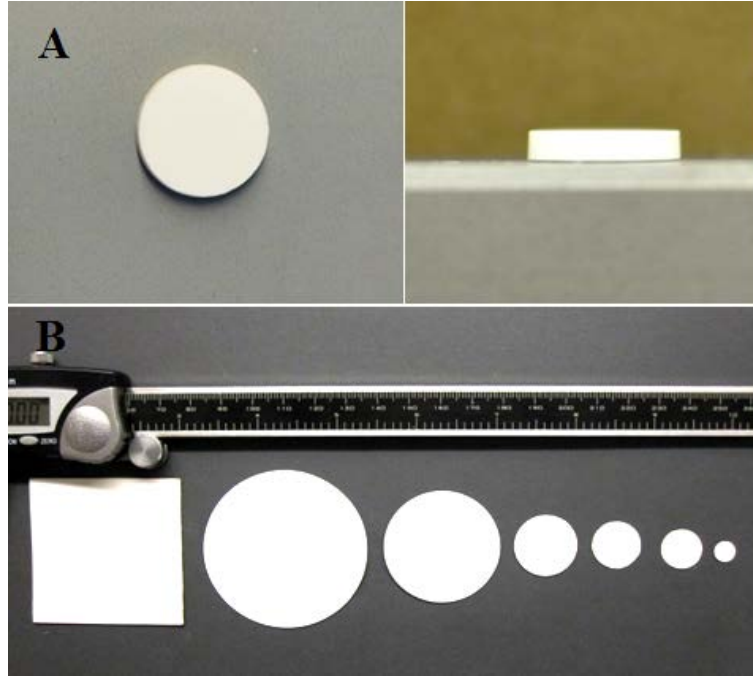
Figure 3-6 LATP plates fabricated A) by dry-pressing and B) by tape casting

Figure 3-6 shows the photos of as-prepared LATP plates fabricated by A) dry pressing and B) green tape fabricated by tape-casting method with various sizes. Compared with die pressing method, the main advantage of tape casting includes 1) it can fabricate the ceramic plates with various dimensions and shapes; 2) tape casting has higher efficiency than die pressing. But since the green tape is thin, so after sintering, the ceramic plates have poor mechanical strength. From figure 3-6A, we can see the side view of the sintered LATP pellets. From observation, we found there was almost no deformation of the pellets after sintering.
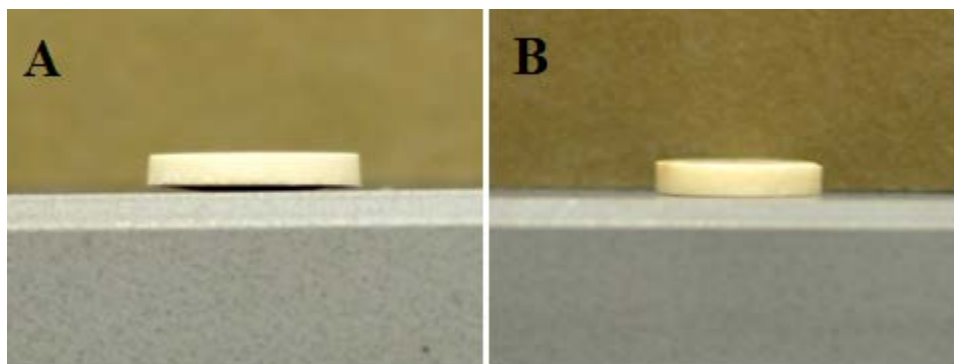
Figure 3-7 Appearance of A) LLZO pellets B) LLT pellets with solid-state reaction synthesis

route

Figure 3-7A is the photo of LLZO pellets with solid-state reaction synthesis route. From the photo, we can observe that LLZO slightly warped after sintering. Figure 3-7B is photo of LLT pellets fabricated with solid-state reaction synthesis route. The pellets have a light yellow color. From observation, we also found that the mechanical strength of LLT pellets are better than LATP and LLZO pellets.
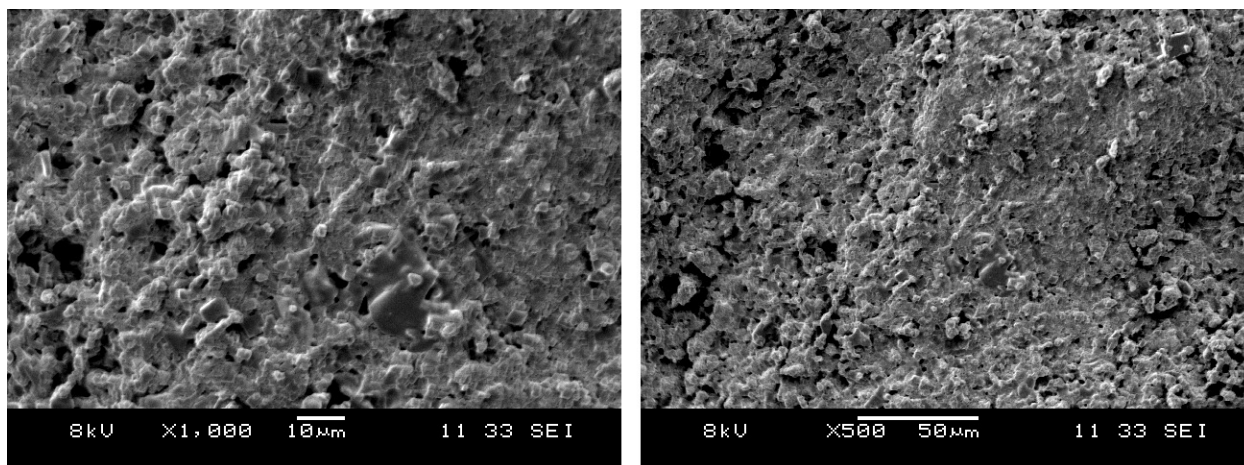
Figure 3-8 SEM of cross section of LATP pellets sintered at 850 °C for 6 hours
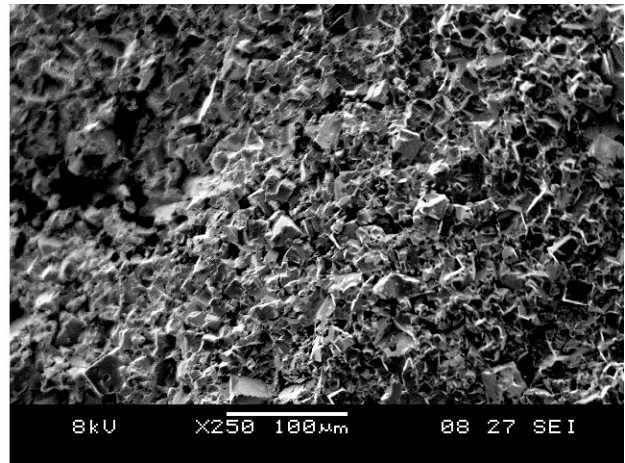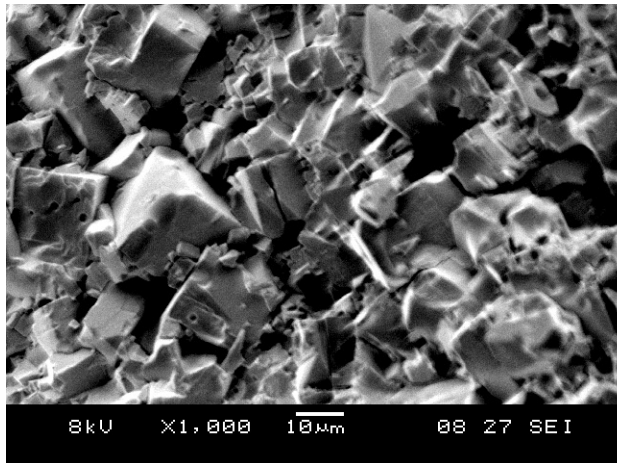
Figure 3-9 SEM of cross section of LATP pellets sintered at 950 °C for 6 hours
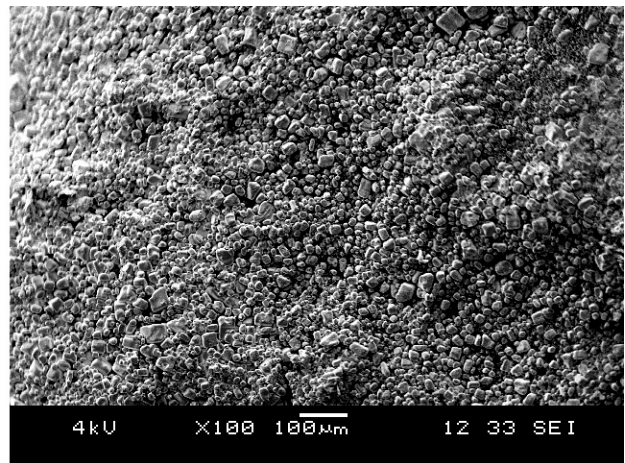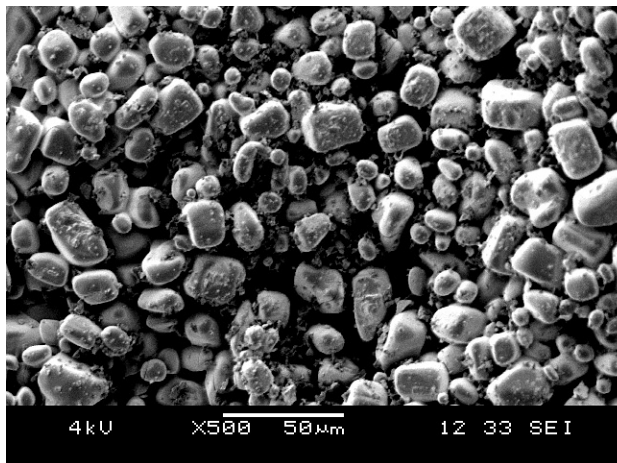
Figure 3-10 SEM of cross section of LATP pellets sintered at 1050 °C for 6 hours
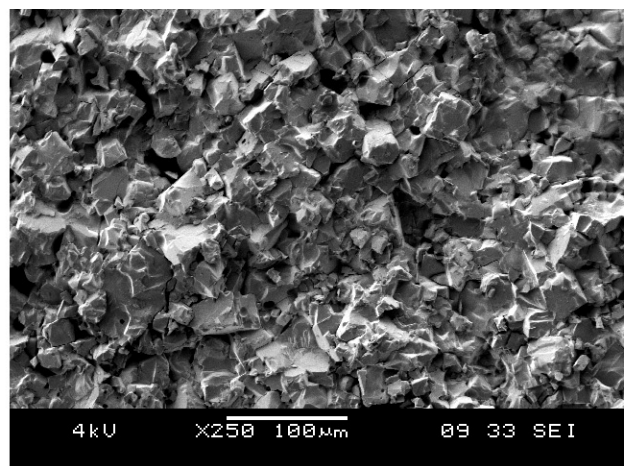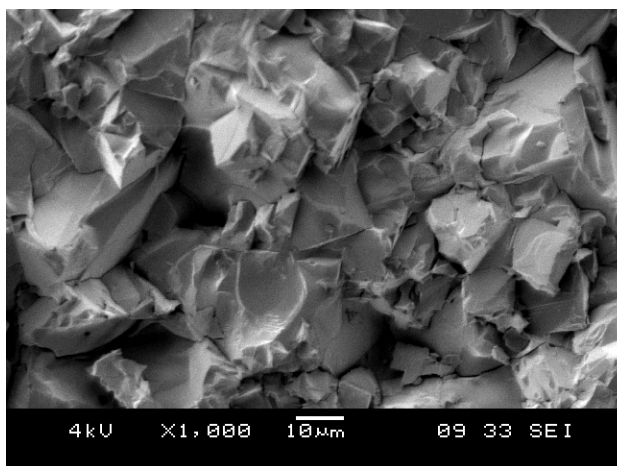
Figure 3-11 SEM of cross section of LATP pellets sintered at 1150 °C for 6 hours

Figure 3-8, 3-9, 3-10 and 3-11 are the SEM images of LATP pellets which were sintered at 850 °C, 950 °C, 1050 and 1150 °C for 6 hours with fast cooling rate. The sintering temperature was increased 3°C/min for all samples. From the pictures, we can see different sintering temperature can significantly affect the crystalline structure and morphology of the LATP ceramic. The crystalline size was increased at higher temperature. Interspace between the grains can be observed inside the pellets.
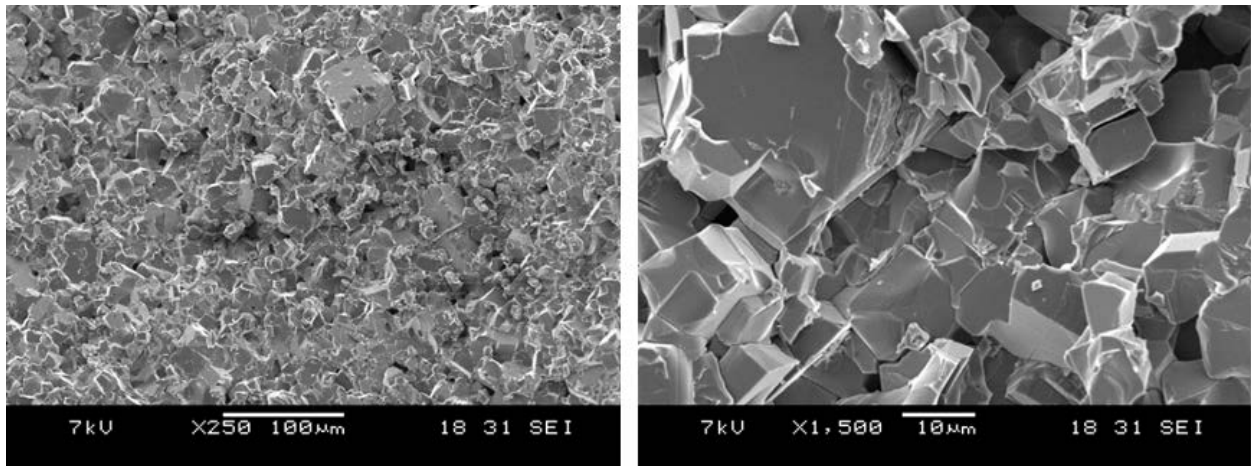
Figure 3-12 SEM of cross section of LATP pellets sintered at 1050 °C for 6 hours, with slow cooling down rate

Figure 3-12 is the SEM image of LATP sample which was sintered at 1050 °C for 6 hours and cooled down at slow rate. We can the cooling rate also plays an important role in forming different micro-structure of the crystal grains. Compares with figure 3-10, we can see the crystalline in figure 3-12 are almost cubic-like. There are also interspace and clear boundary between the grains.

We also explored the method of increasing the porosity of the LATP pellets through adding PVB pore-making agents. Figure 3-13 is the surface morphology of dry-pressed ceramic LATP pellets by SEM, when the weight ratio of PVB varies as A) 0 wt%; B) 5 wt%; C) 10 wt%; D) 40 wt%. We can see the open porosity increases with the PVB ratio. The cavity or pores induced by

the PVB is much greater than the interspace between the grains. We also observed that higher PVB

ratio can decrease the strength of the sintered sample.
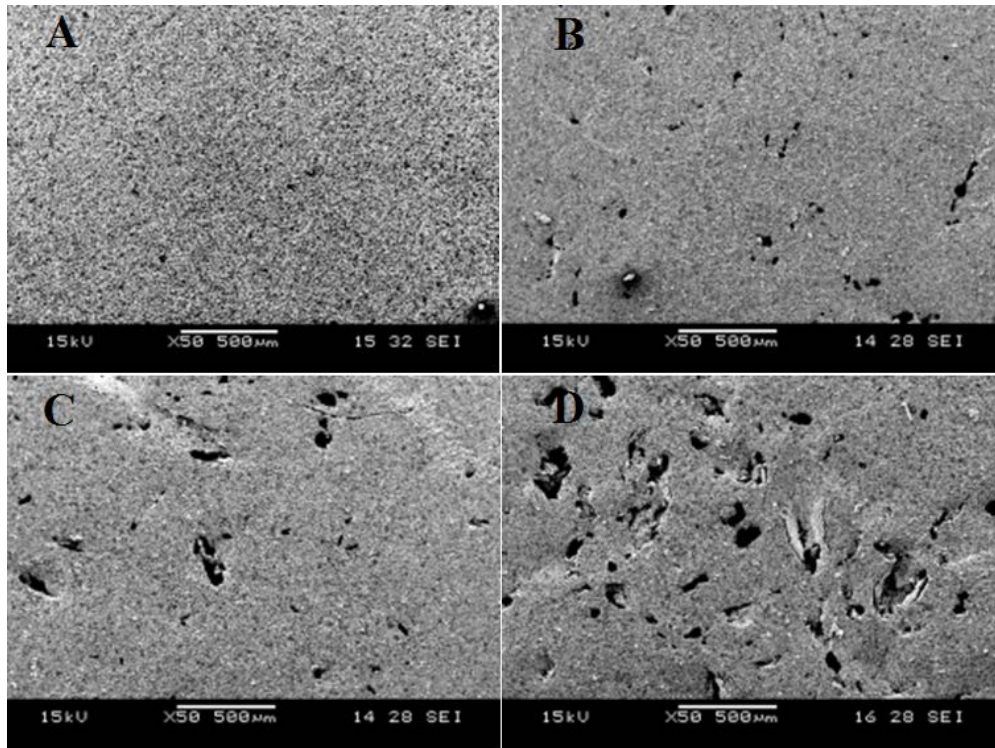
Figure 3-13 SEM image of the porous LATP pellets with different wt% pore maker of PVB
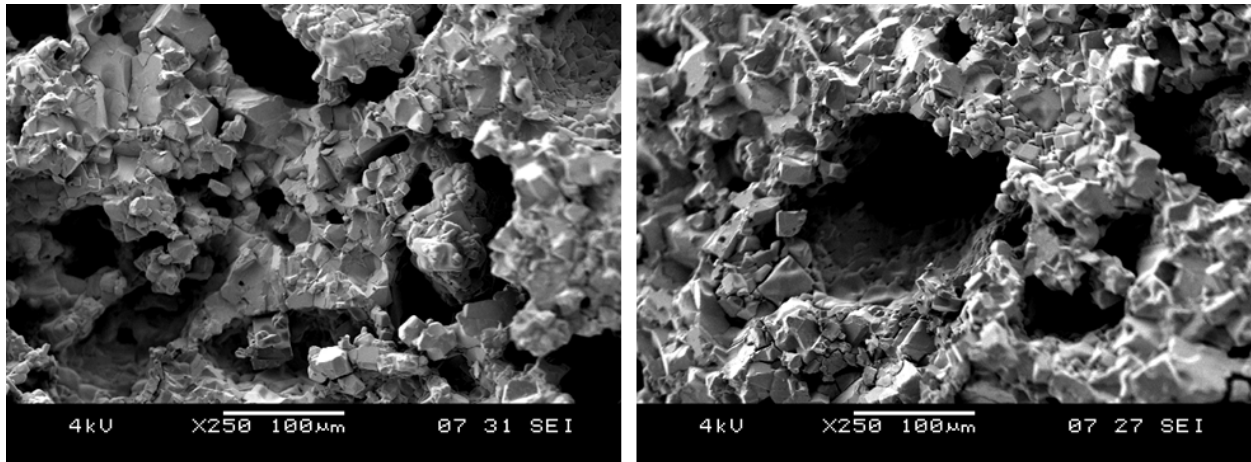
Figure 3-14 SEM image of porous LATP pellets with 30 wt% pore maker of PMMA
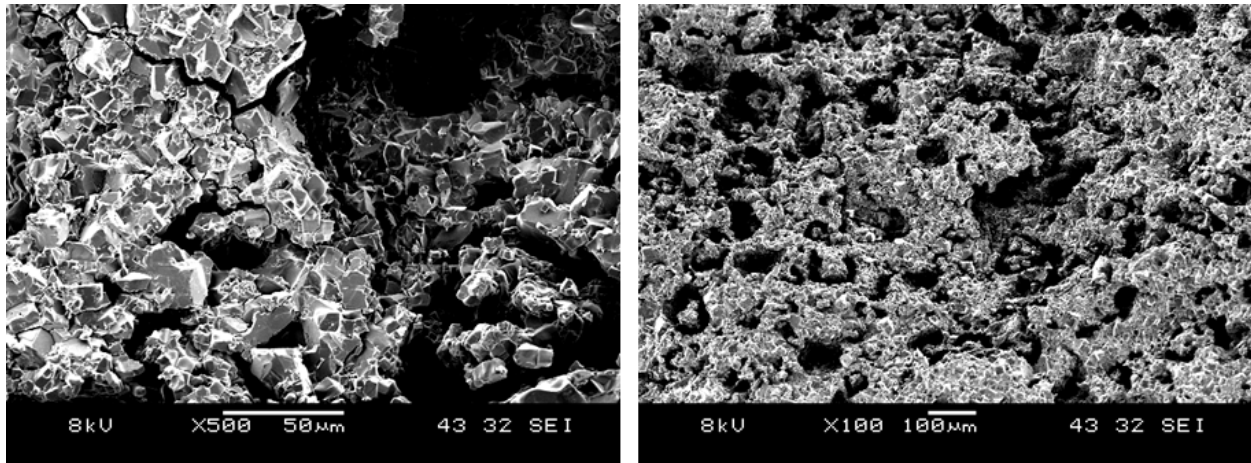
Figure 3-15 SEM image of porous LATP pellets with 30 wt% pore maker of PVA

Figure 3-14 and figure 3-15 are the SEM images of porous LATP pellets with 30 wt% pore-making agent of PMMA and PVA respectively. From the images, we can observed that the pore making agents can significantly affect the micro-structure of ceramic LATP. PMMA can produce more uniformly distributed pores with smaller diameters than PVA. The pores made by PMMA is ~2-10 µm, and pores generated by PVA are 10-100 µm. The pore sizes and distributions can affect the mechanical strength, and the overall conductivity when forming a composite electrolyte with "polymer-in-ceramic" concept structure.
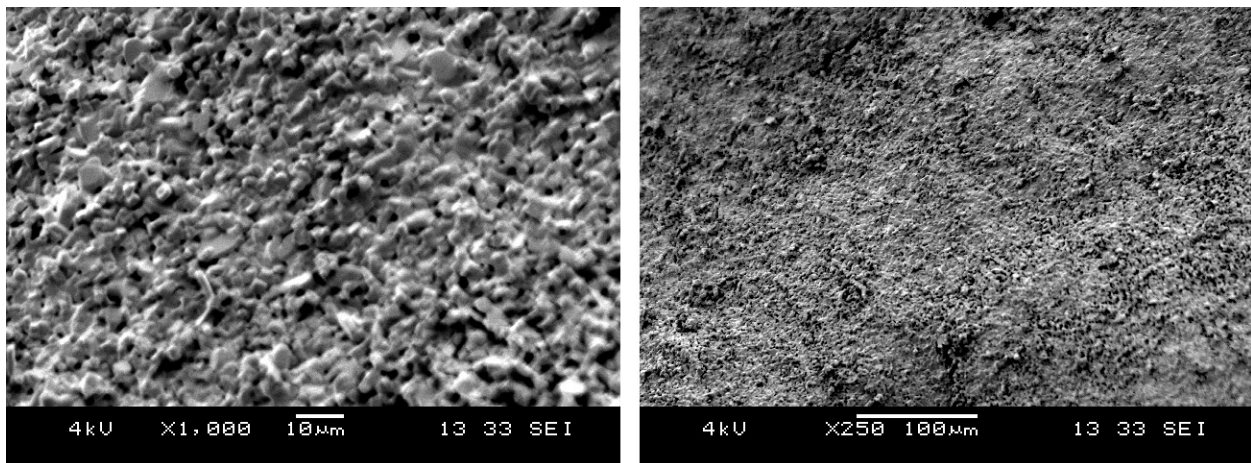
Figure 3-16 SEM image of LLT ceramic pellets which was sintered at 1150 °C for 6 hours
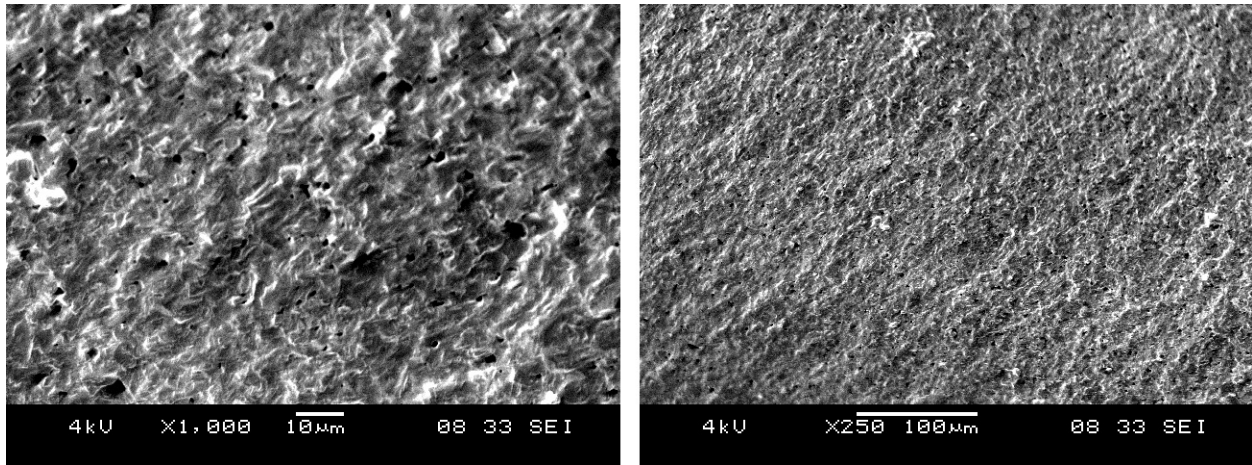
Figure 3-17 SEM image of LLT ceramic pellets which was sintered at 1250 °C for 6 hours
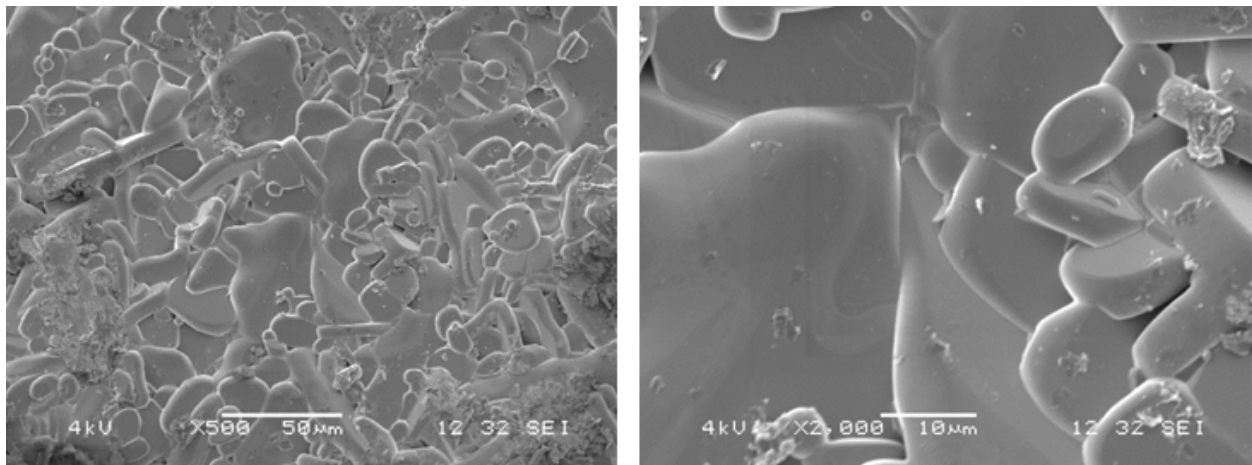
Figure 3-18 SEM image of LLT ceramic pellets which was sintered at 1350 °C for 6 hours

Figure 3-16, 3-17 and 3-18 are the SEM images of LLT ceramic pellets which were sintered at 1150 °C, 1250 °C and 1350 °C for 6 hours respectively. From the SEM pictures of LATP and LLT material, we can find the distinct difference between those different ceramic materials. The grain size of LATP and LLT are about 10 µm and 3 µm respectively. Sintering temperature and also cooling down rate both have major effects on the crystalline structure of the ceramic samples. Those differences in structure may further affect the electrochemical performance of the materials.

3.3.2　Relative Density Measurement of LATP

There is previous research about the relative density variation of LATP material [127, 199]. However, the LATP material they used was synthesized through sol-gel method. In our research, we investigated the variation of the relative density and weight loss of LATP material which was prepared through solid state method.

Table 3-2 Data for different sintering temperature on the weight of the LATP sample pellets

Fabrication method	Sintering Temperature (°C)	Weight Loss (%)	Relative Density (%)
Dry pressing	850	0.86	92.45
	950	0.94	91.95
	1050	1.74	88.71
	1150	3.13	87.06
Tape casting	1050	14.18	87.88

Table 3-2 is the experimental data set which reflects the influence of different sintering temperature on the weight loss and relative density of the LATP sample pellets.
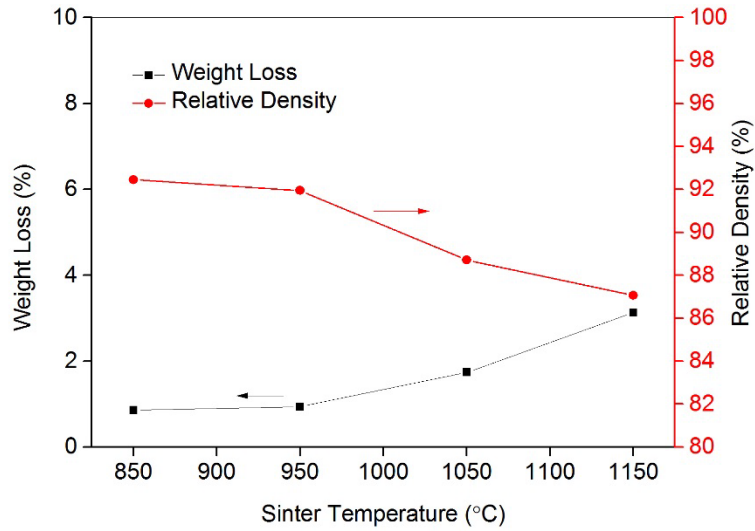
Figure 3-19 Relative density and weight loss variation under different sintering temperature

From Figure 3-19, we can see the trend that the weight loss increases and the relative density decreases when the sintering temperature was increased. The highest relative density of 92.45% was found at the sintering temperature of 850 ˚C. This is consistent with the SEM observation which demonstrated that the samples sintered at 850 ˚C have smaller crystalline size and higher density compared with other sintered samples. The weight loss may be resulting from the evaporation of lithium at elevated temperature. It is also not hard to understand that the tape casting sample has a significant weight loss since there are organic materials in the green tape.

3.3.3 Conductivity of Prepared Ceramic Electrolytes

3.3.3.1 Effect of Temperature to Ionic Conductivity
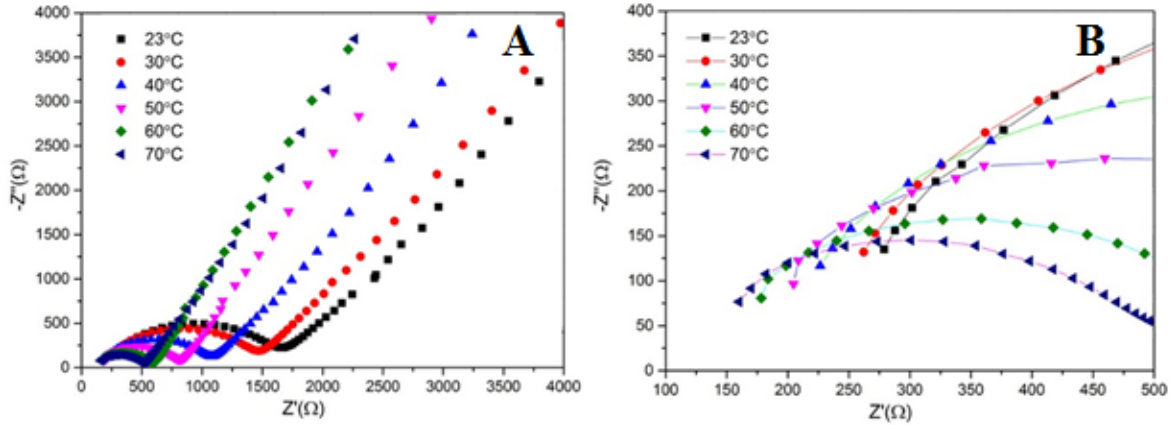
Figure 3-20 A) Nyquist plot of Pt/LATP/Pt at 23˚C, 30 ˚C, 40 ˚C, 50 ˚C, 60 ˚C, 70 ˚C; B) Zoom-in at the high frequency region
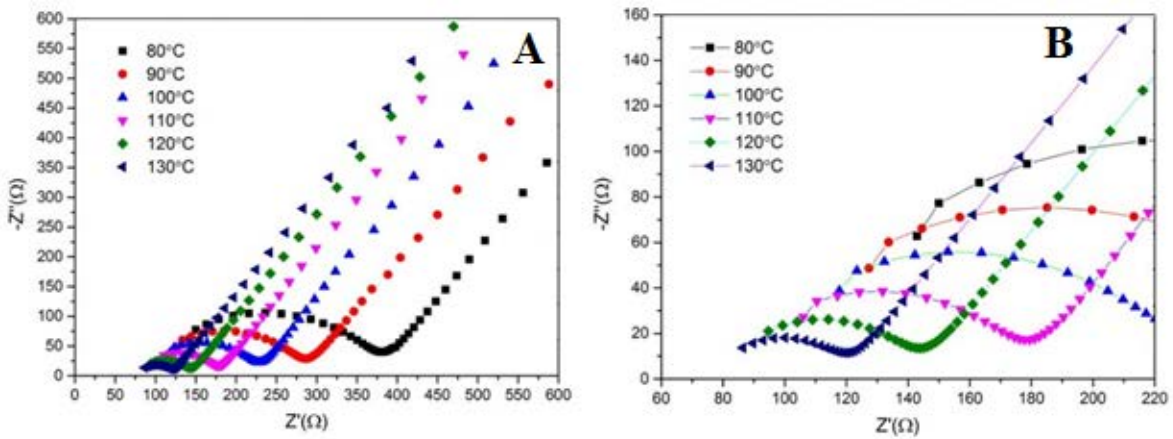
Figure 3-21 A) Nyquist plot of Pt/LATP/Pt at 80 ˚C, 90 ˚C, 100 ˚C, 110 ˚C, 120 ˚C, 130 ˚C; B) Zoom-in at the high frequency region

The conductivity of ceramic electrolyte was significantly affected by temperature. The impedance spectroscopy of Pt/LATP/Pt was measured at 23 ˚C-130 ˚C with the LATP sample sintered at different temperature. The pressure exerted on the stainless steel rod is ~0.045 MPa. Figure 3-20 is the Nyquist plot of LATP ceramic (sintered at 1050 ˚C) at different temperatures of 23 ˚C, 30 ˚C, 40 ˚C, 50 ˚C, 60 ˚C, 70 ˚C. Figure 3-21 is the Nyquist plot of LATP ceramic (sintered at 1050 ˚C) at 80 ˚C, 90 ˚C, 100 ˚C, 110 ˚C, 120 ˚C and 130 ˚C. The range of frequency is 10^6 Hz to 0.1 Hz.

The intercept of the semi-circle at high frequency represents the bulk resistance R_b. The size of the semi-circle reflects the grain boundary resistance R_{gb}. The grain boundary resistance is dominantly large compared to bulk resistance. We can see the obvious decreasing tendency of both the bulk resistance and grain boundary resistance when temperature was increased from room temperature of 23 ˚C to 110 ˚C.

The conductivity was calculated by

$$\sigma = h/R_t\, A = h/(R_b + R_{gb})\, A \qquad\qquad \text{Eq. (3-2)}$$

σ is ionic conductivity, h is the thickness of the sample, R_t is the total resistance, and A is the electrode contact area. For LATP ceramic, $R_t = R_b + R_{gb}$, R_b is bulk resistance, R_{gb} is grain boundary resistance.
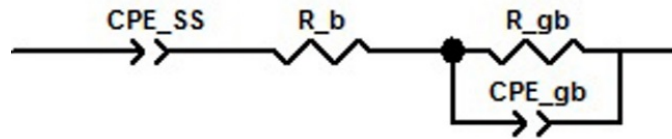
Figure 3-22 Equivalent circuit of LATP ceramic conductor

Figure 3-22 is the equivalent circuit for the EIS modeling of LATP material. R_b represents the bulk resistance of the crystalline grain, R_gb represents the resistance between the crystalline grains. CPE_SS represents the constant phase element at the interface of the LATP material and the stainless steel blocking electrode, CPE_gb represents the constant phase element at the interface between grains.
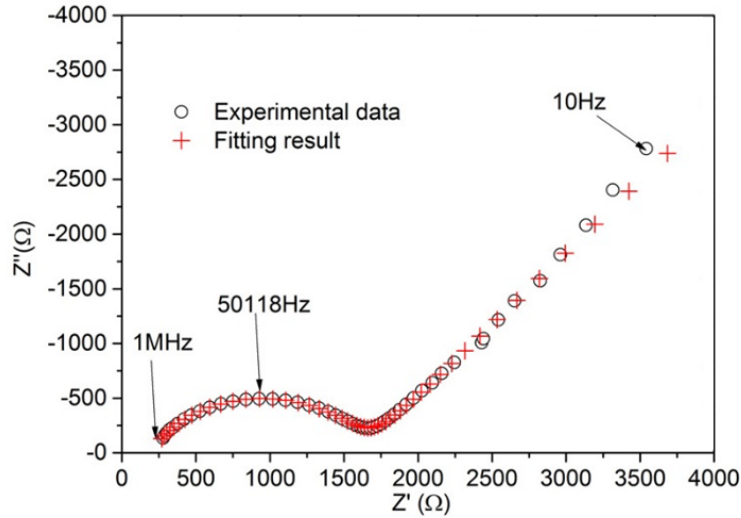
Figure 3-23 Comparison of the experimental data with the fitting result

Figure 3-23 is the Nyquist plot of LATP fitted by the equivalent circuit. We can see that this equivalent circuit can model the behavior of the electrochemical lithium transportation in LATP material with good simulation effect.

Table 3-3 the values of the elements in the equivalent circuit by data fitting

T (°C)	CPE_SS_T (F)	CPE_SS_P	R_b (Ω)	R_gb (Ω)	CPE_gb_T (F)	CPE_gb_p
23	2.5489E-5	0.58881	200.9	1422	5.0347E-8	0.75353
30	2.2475E-5	0.61156	186.9	1249	4.222E-8	0.7655
40	2.7517E-5	0.61801	155.6	906.3	4.3491E-8	0.76759
50	1.5862E-5	0.7183	123.8	698.7	6.0668E-8	0.74551
60	1.7326E-5	0.73161	117.9	476.4	4.6501E-8	0.77611
70	2.4053E-5	0.67525	106.2	395.1	3.9739E-8	0.79067
80	2.7168E-5	0.67235	90.63	289.9	4.4622E-8	0.7891
90	3.1407E-5	0.67224	88.17	199	4.43E-8	0.80527
100	2.8677E-5	0.67783	85.87	140.5	4.0427E-8	0.82502

110	3.3095E-5	0.67497	81.95	95.41	5.3802E-8	0.82495
120	3.5363E-5	0.67542	75.24	68.82	1.1122E-7	0.79046
130	3.2861E-5	0.67905	72.78	48.48	2.6392E-7	0.7574

Table 3-3 shows the values from the fitting results. From the table 3-3, we can see that the value of CPE_SS_T was about $\sim 10^{-5}$ of order magnitude, CPE_SS_P ranges from 0.58-0.73. CPE_gb_T was about $\sim 10^{-8}$ of order magnitude, CPE_gb_P ranges from 0.75-0.83. No obvious pattern of variation of those parameters was found when the temperature was increased.
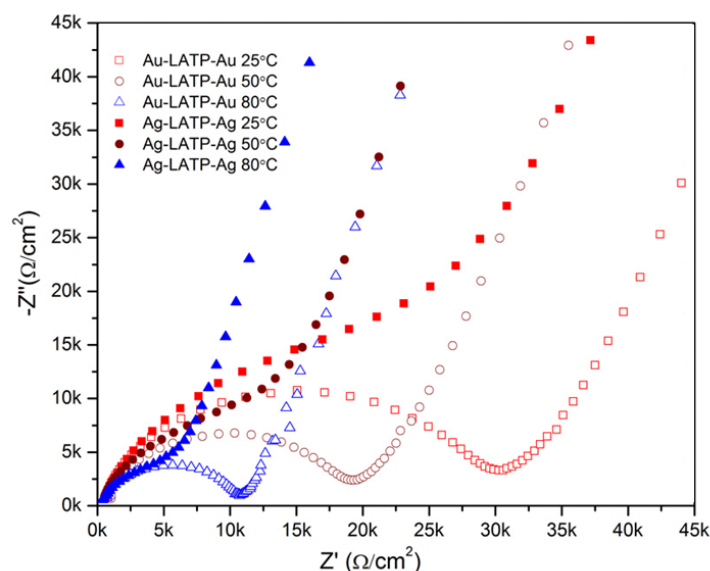
Figure 3-24 Nyquist plot by different blocking electrode

As part of the EIS measurement, we also demonstrated the effect on Nyquist plot by different blocking electrode of silver paste and gold sputtering respectively, as shown in figure 3-24. The sample with gold sputtering has a more complete semi-circle and the sample with silver paste shows an earlier transit to vertical lines at the medium to low frequency range. Although the plots using different blocking electrode show very different plots, we can still recognize the magnitude of the grain boundary and bulk resistance from the graph. It is clear that the gold sputtering plot was easier to read from the plot.
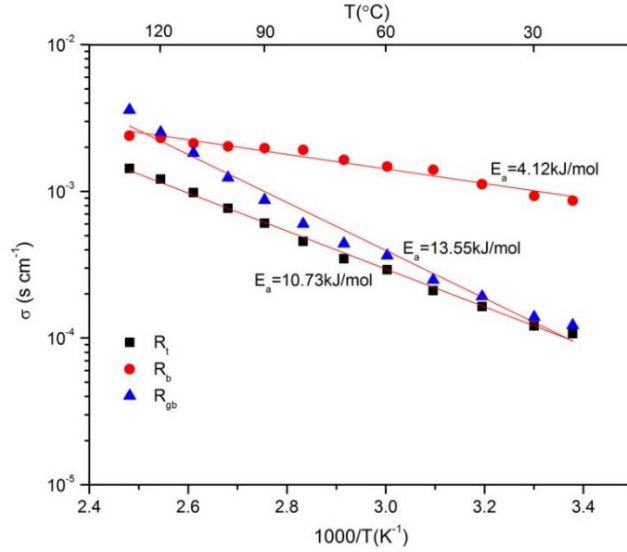
Figure 3-25 Arrhenius plot of LATP sintered at 1050 ˚C

Figure 3-25 is the Arrhenius plot of total conductivity, bulk and boundary conductivity of LATP at different temperature. The activation energy was calculated by

$$\sigma = \sigma_0 exp(-\frac{E_a}{k_b T}) \qquad \text{Eq. (3-2)}$$

$$k_b = 1.3806 \times 10^{-23} \ (J/K)$$

σ_0 is the pre-exponential factor, E_a is the activation energy, k_b is the Boltzmann constant, and **T** is the absolute temperature.

The equation 3.1 can be transformed as:

$$ln\sigma = ln\sigma_0 - \frac{1}{K_b}\frac{E_a}{1000}\frac{1000}{T} \qquad \text{Eq. (3-3)}$$

From Equation 3-3, we can see $ln\sigma$ and $\frac{1000}{T}$ has a linear relationship. By method of least square fitting the experimental data, we can find the value of E_a and σ_0. The activation energies for bulk and grain boundary resistances of LATP were calculated as 11.09 kJ/mol (0.11eV) and 28.45 kJ/mol (0.29eV) respectively.
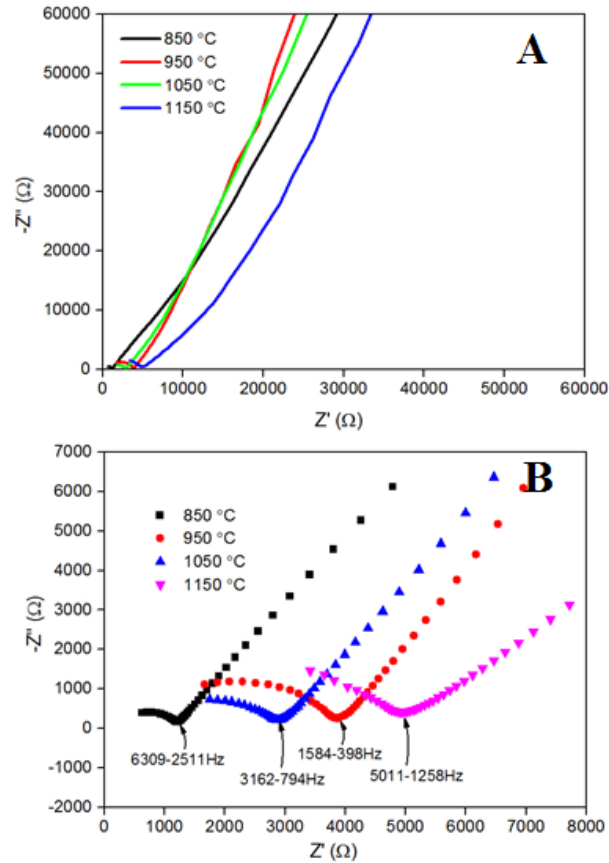
Figure 3-26 A) Nyquist plot of LATP sintered at 850 ˚C, 950 ˚C, 1050 ˚C, 1150 ˚C; B) Zoom-in

at the high frequency region

Figure 3-26A show the different Nyquist plot of LATP sintered with different temperature. Figure 3-26B is the zoom-in detail at high frequency. We can see that all the samples have similar pattern at the whole frequency range. The characteristic frequency for the semi-circle interception with the real axis may have subtle differences as we can see from figure 3-26B.
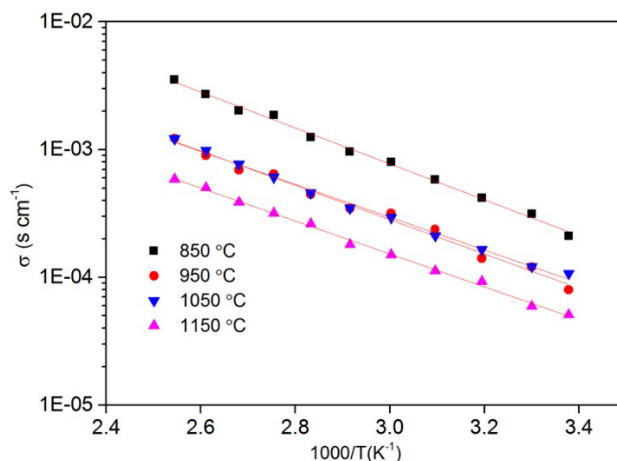
Figure 3-27 Arrhenius plot of LATP sintered at 850 ˚C, 950 ˚C, 1050 ˚C, 1150 ˚C

Table 3-4 Variation of E_a and σ_0 with sinter temperature

Sinter Temperature (˚C)	E_a	σ_0
850	11.56	1.027
950	11.14	1.047
1050	10.68	1.029
1150	10.73	1.024

We have also measured the Arrhenius plot of LLTP ceramic which was sintered at different temperatures of 850 ˚C, 950 ˚C, 1050 ˚C, 1150 ˚C. Figure 3-27 is the Arrhenius plot of LATP material synthesis at different temperature. The highest sintering temperature in our experiments was 1150 ˚C, since at this temperature, the samples have a tendency of cracking. The samples sintered at 850 ˚C was found to be most ionic-conductive, even though most literatures using the 1050 ˚C as the sintering temperature. We also found the sample sintered at 850 ˚C has best mechanical strength (MS), the order is $MS^{LATP850} \gg MS^{LATP950} \approx MS^{LATP1050} > MS^{LATP1150}$.
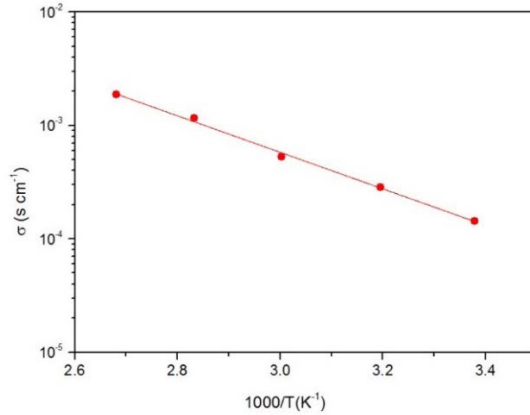
Figure 3-28 Arrhenius plot of LLZO synthesized by solid state reaction

Figure 3-28 is the Arrhenius plot of LLZO material synthesized by solid-state reaction. We can see LLZO has comparable conductivity with LATP material, which is greater than LLT material. However, compares with LATP, LLZO consumes much more time for synthesis and fabrication.
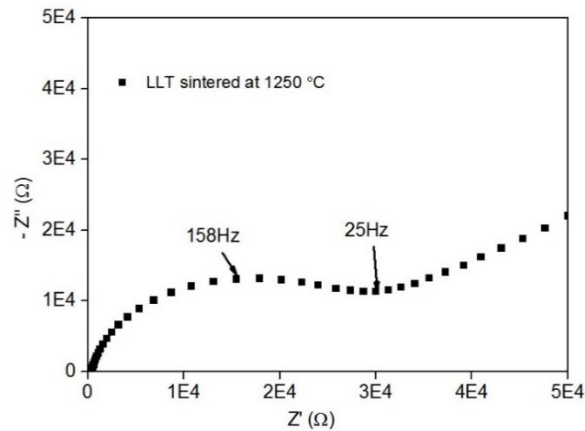
Figure 3-29 Nyquist plot of Au/LLT (sintered at 1250 ˚C)/Au at temperature of 23 ˚C

Figure 3-29 is the Nyquist plot of Au/LLT (sintered at 1250 ˚C)//Au from temperature of 23 ˚C. The Arrhenius plot of LLT material sintered at different temperature was presented in figure 3-30. The LLT sintered at 1050 ˚C and 1150 ˚C has much lower conductivity compares with LLT sintered at 1250 ˚C. The order of the mechanical strength is $MS^{LLT1350} > MS^{LLT1250} > MS^{LLT1150} > MS^{LLT1050}$. Due to the reason that LLT sintered at 1350 ˚C has adhered on the ceramic aluminum

plates, we did not measure its conductivity. Compared with LATP, the conductivity of LLT material is about one order less.
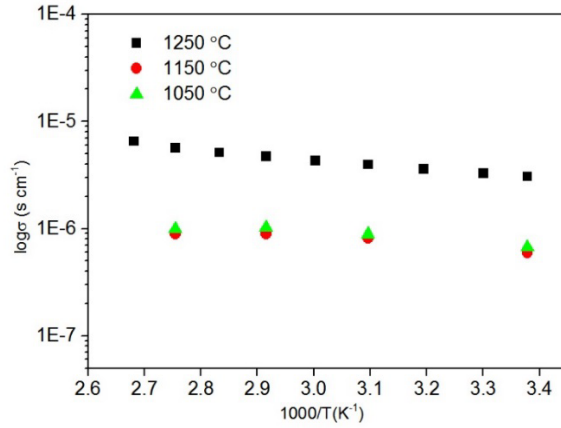
Figure 3-30 Arrhenius plot of conductivity of LLT material sintered at different temperature

3.3.3.2 Effect of Pressure to Ionic Conductivity
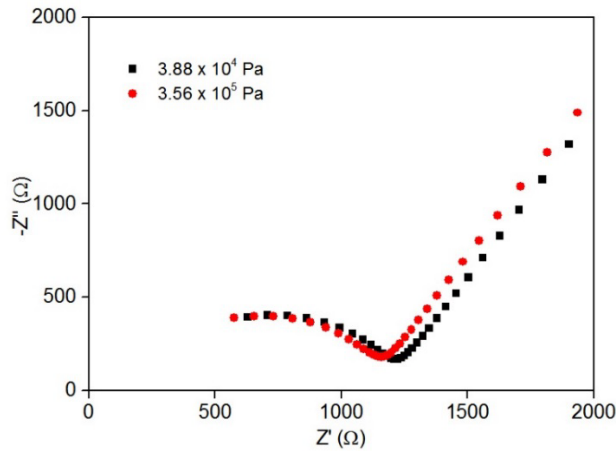
Figure 3-31 Nyquist plot of Au/LATP (sintered at 850 ˚C)/Au under different pressure

Figure 3-31 is the Nyquist plot of Au/LATP/Au under different pressure, the LATP material was sintered at 850 ˚C for 6 hours. The pressure exerted on the sample is 3.88×10^4 Pa and 3.56×10^5 Pa respectively. From the figure, we can see the conductivity was increased subtly. The higher pressure may improve the contact of the grains, and therefore, the grain boundary resistance was decreased slightly.
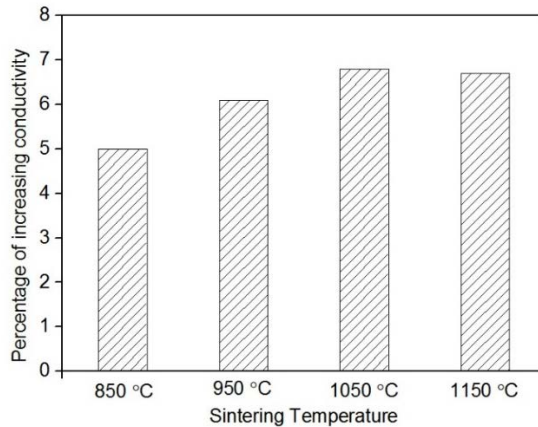
Figure 3-32 Pressure dependence of the conductivity of LATP material sintered at different

temperature

Figure 3-32 is the pressure dependence of the LATP material sintered at different temperature of 850 ˚C, 950 ˚C, 1050 ˚C and 1150 ˚C. It was suggested that the pressure has limited effect to improve the conductivity. Only subtle difference exist between the samples.

3.3.4 Stability of Prepared Ceramic Electrolytes
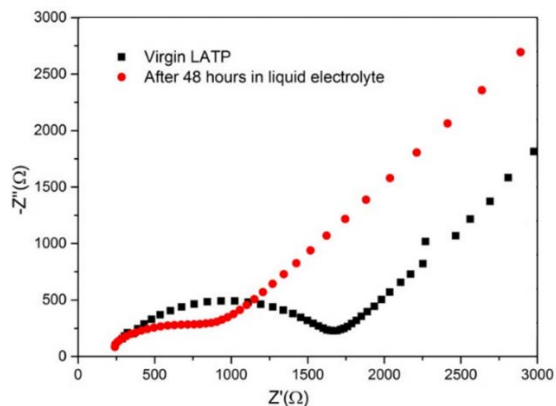
Figure 3-33 Nyquist plot of the LATP pellets A) before and B) after immersed in organic

solution of DMC+EC+LiTFST
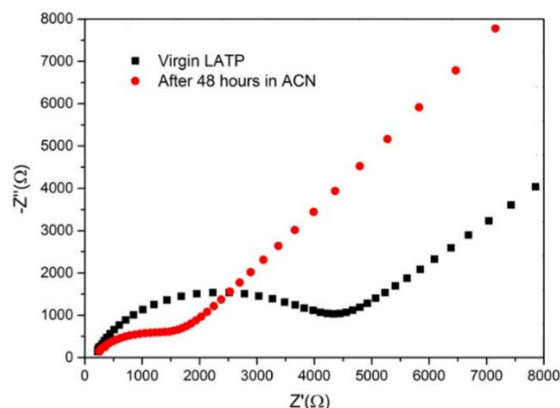
Figure 3-34 Nyquist plot of the LATP pellets A) before and B) after immersed in ACN solution

The stability of LATP materials to different organic solvents was investigated through EIS method. From observation by naked eye, the integrity of the sample was not affected after long time soakage. It is interesting to find after soaking in ACN solution and liquid electrolyte for 48 hours, the conductivities of LATP samples were not decreased but increased as shown in figure 3-33 and figure 3-34. This may be related to the residue organic still existing in LATP pores, those ions also have attributed to the total conductivity. However, this may also decrease the lithium ion transference number. Those treatments of exposure to liquid electrolyte may enhance the lithium ion conductivities, but the characterization of lithium ion transference number to be need further investigated.

3.4   Conclusion

We have experimentally explored the properties of different types of ceramic electrolytes, including: material synthesis, sample fabrication, conductivity measurement at different temperature and pressure, and stability versus organic solvents and liquid electrolyte, etc. From the data we obtained, we can compare the comprehensive performance of LATP, LLT, LLZO material as electrolyte in ASSLIBs.

We evaluated the different sintering temperature on LATP conductivity and relative density. Higher sintering temperature can result in higher weight loss and may create higher thermos stress on dry pressed samples, and result in cracks or internal defect in the pellets. The relative density decreases with increasing sintering temperature, which is contradictory with the previous research where LATP was synthesized using sol-gel method [199]. Our work also demonstrated that the sample sintered at 850 ˚C has the highest mechanical strength and also ionic conductivity.

Table 3-5 Comprehensive comparison of different ceramic electrolytes

Ceramic type	Ease of synthesis	Conductivity at R.T.	Mechanical strength	Stability *vs* Li	Ease of fabrication
LATP	Easy	High	Normal	Normal	Easy
LLZO	Hard	High	Normal	High	Medium
LLT	Normal	Low	High	Normal	Hard

Table 3-5 is the comprehensive comparison of different ceramic electrolytes. The ease of synthesis, fabrication, the conductivity, mechanical strength, stability *vs* Li metal and also expense of synthesis was compared. Through this comparison, the LATP material, due to its high conductivity, ease of fabrication and synthesis, and lower economy expense, is the most optimal candidate for fabricating a multilayer electrolyte with SPE. While LLZO can be used as the ceramic stabilizer at the interface of Li metal and polymer electrolyte, since its high conductivity and high stability with lithium metal. LLT material has excellent mechanical strength, however, its conductivity is too low in R.T. compared with LATP and LLZO.

Chapter 4 Polymeric Electrolyte Fabrication and Characterization

4.1   Introduction

In our work, we choose PEO-LiN(CF$_3$SO$_2$)$_2$ (LiTFSI) as the solid polymer electrolyte. LiTFSI was chosen as the lithium salt due to its high its high conductivity, high stability against hydrolysis [45], and also high stability on lithium anode surface [200]. The bulky imide-based anions TFSI$^-$ could lower the melting point of PEO polymer host, enhance the conductivity by greater plasticization of the PEO-LiX system [46]. The copolymer poly(vinylidene fluorideco-hexafluoropropylene) (PVdF-HFP) is selected as the gel-type electrolyte host material. The copolymer PVdF-HFP has been widely investigated due to its appealing comprehensive properties. For example, it provides greater ionization of salt, liquid electrolyte entrapping abilities, and good mechanical strength [151, 156].

There is previous work on the SPE and GPE synthesis and characterization, but the measured conductivities by different researchers are not consistent [46, 55]. Before the multi-layer electrolyte was fabricated, the SPE and GPE must be synthesized, fabricated and characterized in different route. The conductivity, impedance profile, transference number was measured. Their other properties, for example, mechanical strength, ease of fabrication were also evaluated and discussed.

4.2   Experimental Methods

4.2.1   Material Synthesis and Fabrication

PEO$_{10}$-LiTFSI electrolyte can be fabricated by two methods, hot-pressing and solvent-casting. Compared with the hot-pressing fabrication method, the solvent-casting can fabricate a more uniform, thoroughly mixed, shape-flexible, and most important, thinner electrolyte layer. As we know, the key to minimizing the resistance of the solid electrolyte is to decrease the thickness of

the electrolyte. And solvent-casting is more efficient than hot-pressing too, which is important for massive production. Hot-pressing, on the other hand, was reported to be able to maintain more stable interface with lithium metal, since it eliminates the presence of rudimental solvent component [6].

In our experiments, both solvent-casting and hot-pressing methods were applied. The details of experimental fabrication procedures are as follows:

For hot-pressing method, PEO (MW 1,000,000g/mol) and LiTFSI(Sigma-Aldrich) were dried inside the vacuum oven for at least 48 hours, at 50 °C and 150 °C respectively. PEO and LiTFSI were then weighted for the ratio (EO: Li = 10:1) and thoroughly mixed. The mixture was placed inside a heating die. The die was heated to about 100 °C at a rate of 10 °C /min. The heating die was then pressed using the hydraulic press machine. The pellet was pressed under ~80 MPa for 30 mins. The inner diameter of the heated die is 13 mm.

To fabricate a solvent-casting type plate, firstly, PEO and LiTFSI were dried inside the vacuum oven for at least 48 hours, at 50 °C and 150 °C, respectively. PEO and LiTFSI were then weighed at the ratio (EO: Li = 10:1) and then dispersed in anhydrous acetonitrile (ACN) solution. Subsequently, the mixture was magnetically stirred for 24 hours at room temperature. Then the slurry was coated on the stainless steel plates. After the slow evaporation process of ACN, the product film is further dried in a vacuum oven at 50 °C for 48 hours.

The PVdF-HFP based GPE was prepared by a solvent casting method. First, PVdF-HFP, LiTFSI were stored in a vacuum oven and de-moisturized at 70 °C for 48 hours before use. Then, PVdF-HFP, LiTFSI, ethylene carbonate (EC), propylene carbonate (PC) were dissolved under specific weight ratios in N-Methyl-2-pyrrolidone (NMP) and anhydrous tetrahydrofuran (THF). The slurry was poured on the flat glass surface, and THF and NMP were allowed to evaporate at

room temperature. After the evaporation of THF, the mechanically stable self-standing GPE films with uniform thickness can be obtained.

4.2.2   Lithium Ion and Electronic Transference Number Measurement

The lithium ion transference number for the polymer electrolyte was determined by D.C polarization technique using Solartron 1287/1860 electrochemical testing platform. The prepared SPE and GPE were assembled in a coin cell with Li | SPE/GPE | Li structure. The testing parameters were controlled by the CorrWare. The bias voltage applied was 0.3V. The testing was carried out at room temperature (23 °C).

The value of lithium ion transference number T_{Li^+} was calculated from the normalized polarization current versus time plot using the equation [201-203]:

$$T_{Li^+} = \frac{I_S(\Delta V - I_0 R_0)}{I_0(\Delta V - I_S R_S)} \qquad \text{Eq. (4-1)}$$

$$T_{Li^+} = \frac{I_S}{I_0} \qquad \text{Eq. (4-2)}$$

Where I_0 is the initial current, I_s is the residual steady current, ΔV is the bias voltage applied, R_0 is the film resistance before polarization, R_S is the film resistance after polarization, Eq. (4-2) was also used for calculate the lithium ion transference number when only a negligible small bias voltage (< 10 mv) was applied [202].

The electronic transference number was measured using D.C polarization with Solartron 1287/1860 electrochemical testing platform. The test sample of SPE or GPE was stacked between two stainless steel electrodes and D.C voltage of 0.3V was applied between the samples. The testing was carried out at room temperature (23 °C). The electronic conductivity can be calculated by

$$\sigma_e = \frac{I_S}{V} \qquad \text{Eq. (4-3)}$$

The electronic transference number T_{e^-} can be calculated by

$$T_{e^-} = \frac{I_S}{I_0} = \frac{\sigma_e}{\sigma_t}$$

Where σ_e is electronic conductivity, σ_t is the total conductivity measured by impedance measurement.

4.2.3 Stability and Degradation

The degradation phenomenon of SPE under high temperature (80 ˚C) was investigated. The hot-pressed SPE was sealed in a coin cell case of CR2025, and then the cell was placed in an oven. The impedance was measured each 5 hours.

4.3   Results and Discussion

4.3.1 Appearance and Morphology
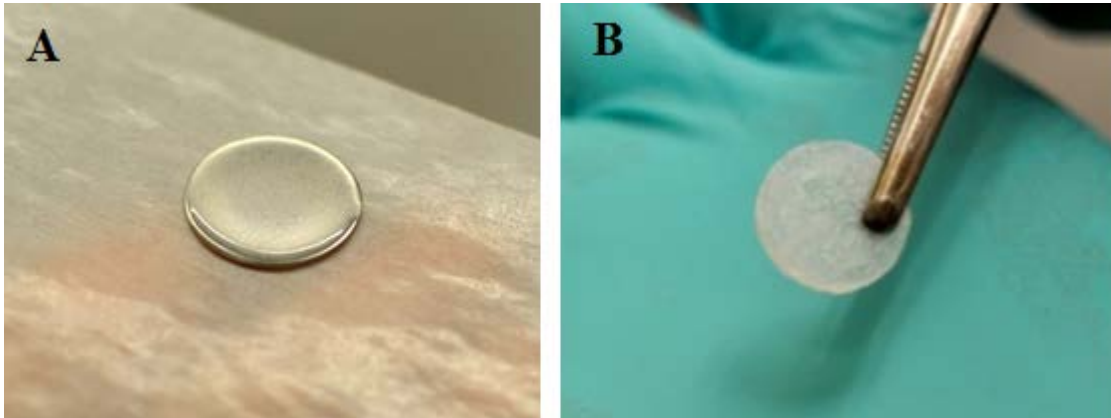
Figure 4-1 SPE fabricated by A) solvent casted on a stainless steel plate, B) hot pressing

Figure 4-1 shows the pictures of A) solvent casting SPE on a Teflon disk. B) hot-pressed SPE. From the picture, we can see the hot-pressed SPE can be fabricated as thin film with free-standing mechanical strength. The solvent casting SPE was a very thin, sticky and adhesive on the surface of the stainless steel disk. The hot pressed electrolyte was an opacified pellet, where the white dots through the pellets are the enriched region of LiTFSI salt. The solvent-casting SPE is transparent without the lithium salt agglomeration.
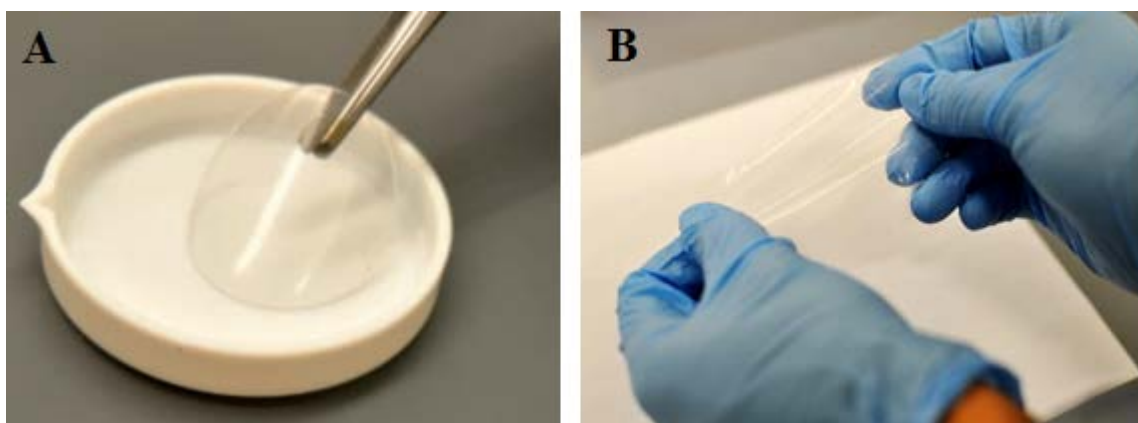
Figure 4-2 As-prepared GPE. A) Thick film (~1mm). B) thin film (~100µm)

Figure 4-2 shows the as-prepared GPE with A) thickness of 1 mm, and B) thickness of ~100 µm. By controlling the viscosity of the slurry, we can fabricate the GPE with different thickness. Those self-standing and elastic films can be cut with different sizes and shapes.

4.3.2 Lithium Ion and Electronic Transference Number
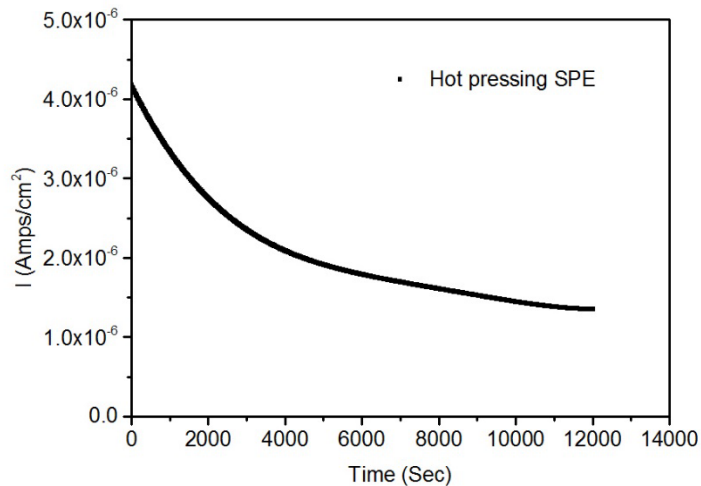
Figure 4-3 Polarization current versus time for Li | hot-pressed SPE | Li symmetric cell at 23 ˚C
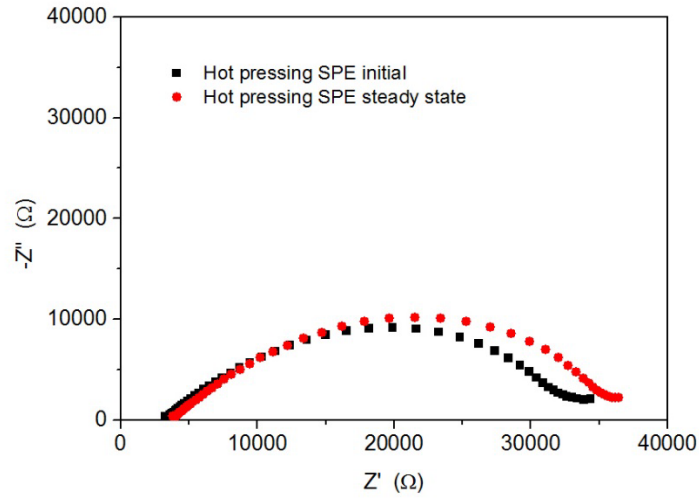
Figure 4-4 Impedance scans of Li | hot-pressed SPE | Li sample before and after potentiostatic

measurements at 23 ˚C

Figure 4-3 is the polarization current versus time for Li | hot-pressed SPE | Li symmetric cell

at 23 ˚C. Figure 4-4 is the Nyquist plot of Li | hot-pressed SPE | Li sample before and after

potentiostatic measurements at 23 ˚C. Using the equation 4-1, we can calculate that the T_{Li^+} is

~0.35 at 23 ˚C.
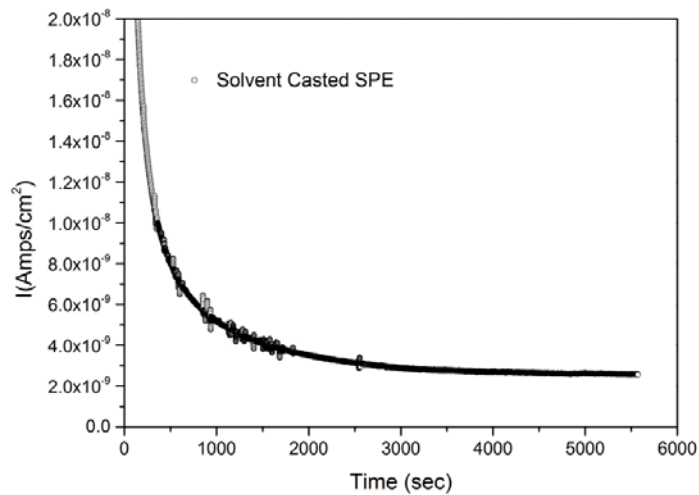
Figure 4-5 Polarization current versus time for SS | solvent casted SPE | SS symmetric cell at 23

˚C
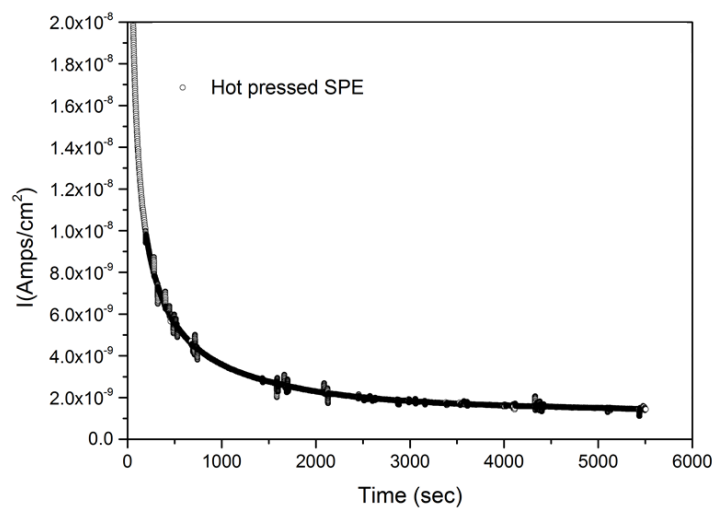
Figure 4-6 Polarization current versus time for SS | hot pressed SPE | SS symmetric cell at 23 ˚C
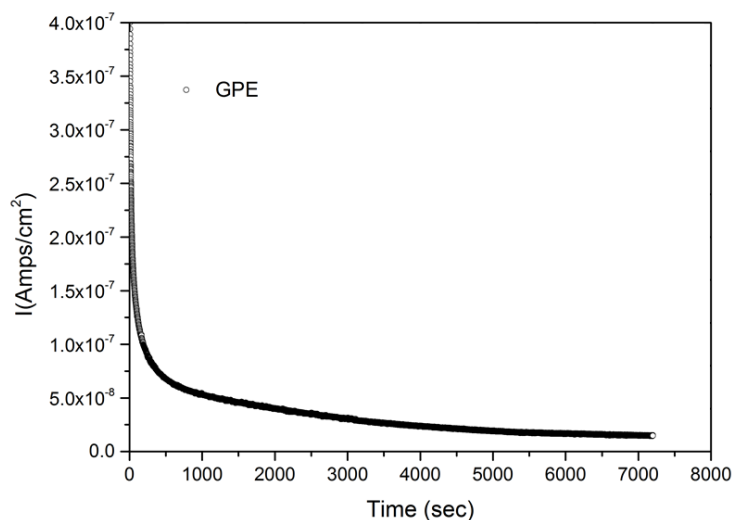
Figure 4-7 Polarization current versus time for SS | GPE | SS symmetric cell at 23 ˚C

Figure 4-5, 4-6, 4-7 are the plots of polarization current versus time for SS | solvent casted SPE/ hot pressed SPE/ GPE | SS symmetric dummy cell at 23 ˚C respectively. From the plots, we can calculate the electron conductivity of hot solvent casted SPE/pressed SPE/GPE are 6.67E-9, 1.05E-8 and 5E-8 respectively. This indicates the as-prepared polymer electrolyte has negligible electron conductivity, however, the usage of liquid organic components during fabrication may induce impurities, thus increase the electron conductivity.

4.3.3   Electrochemical Impedance Spectroscopy Characterization
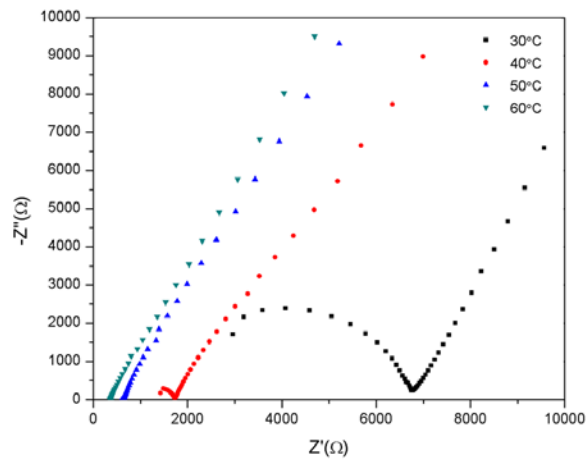
Figure 4-8 Nyquist plot of SS/ PEO10-LiTFSI/SS at 30 ˚C,40 ˚C, 50 ˚C, 60 ˚C
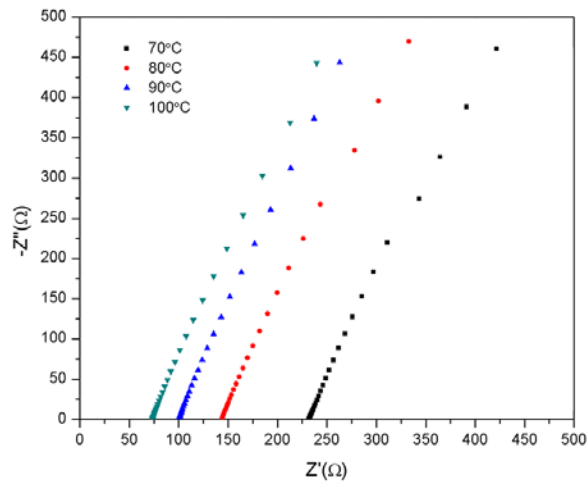
Figure 4-9 Nyquist plot of SS/ PEO_{10}-LiTFSI/SS at 70˚C, 80 ˚C, 90 ˚C, 100 ˚C
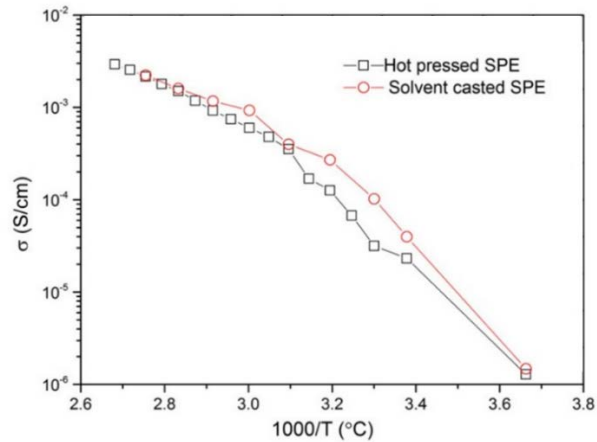
Figure 4-10 Temperature dependence of ionic conductivity of hot-pressed and solvent casted

SPE

Figure 4-8 and figure 4-9 are the Nyquist plot of SS/hot-pressed SPE/SS at 25 ˚C, 30 ˚C, 40 ˚C, 50 ˚C, 60 ˚C and 70 ˚C, 80 ˚C, 90 ˚C, 100 ˚C respectively. The temperature has significant impact on the conductivity of SPE materials. We also observed that the semi-circle at high frequency region disappeared at temperature higher than 45 ˚C.

The solvent casted SPE was also characterized with EIS method, and its conductivity was compared with hot-pressed SPE. The temperature dependence of ionic conductivity of hot-pressed and solvent casted SPE is shown in figure 4-10. We can see that the ionic conductivity was increased when temperature was increased. The melting point of hot-pressed SPE was about 45 ˚C. The activation energy of PEO_{10}-LiTFSI solid electrolyte was evaluated as 84.23 kJ/mol (0.87eV) and 42.69 kJ/mol (0.44eV) above and below melting point respectively.
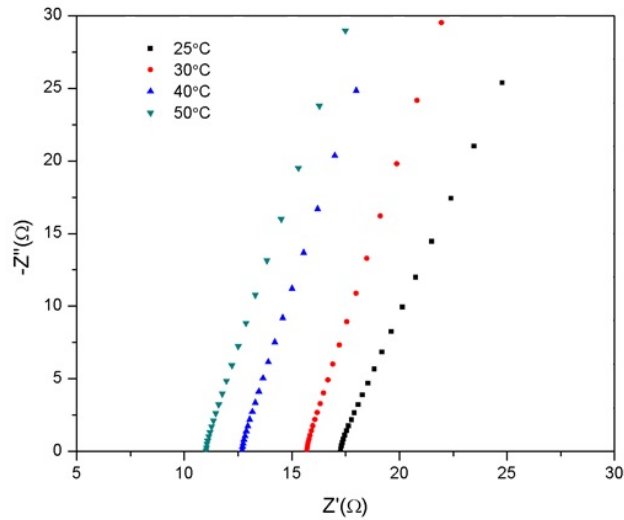
Figure 4-11 Nyquist plot of SS/ PVdF-HFP:LiTFSI/SS at 30 ˚C,40 ˚C, 50 ˚C, 60 ˚C
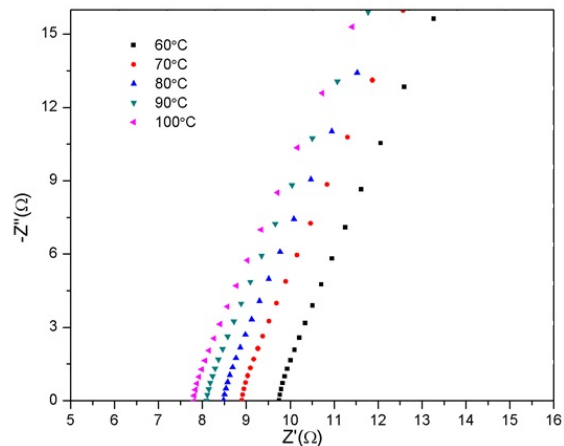
Figure 4-12 Nyquist plot of SS/ PVdF-HFP: LiTFSI/SS at 70˚C, 80 ˚C, 90 ˚C, 100 ˚C
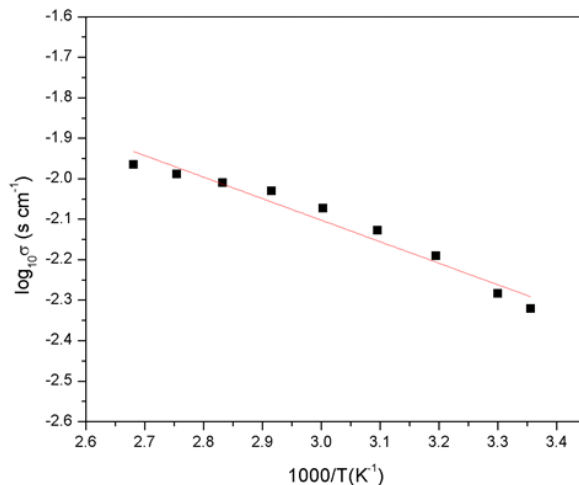
Figure 4-13 Temperature dependence of ionic conductivity of PVdF-HFP/LiTFSI gel-polymer

electrolyte

Similarly, the ionic conductivity of PVdF-HFP based gel-polymer electrolyte was also measured at different temperature. The Nyquist plot of ionic conductivity of PVdF- HFP/LiTFSI gel-polymer electrolyte is presented at figure 4-11 and figure 4-12. The temperature dependence of ionic conductivity of PVdF- HFP/LiTFSI gel-polymer electrolyte is presented at figure 4-13. The activation energy was calculated as 10.14 kJ/mol (0.10 eV).

4.3.4　Stability of the Polymer Electrolyte at High Temperature
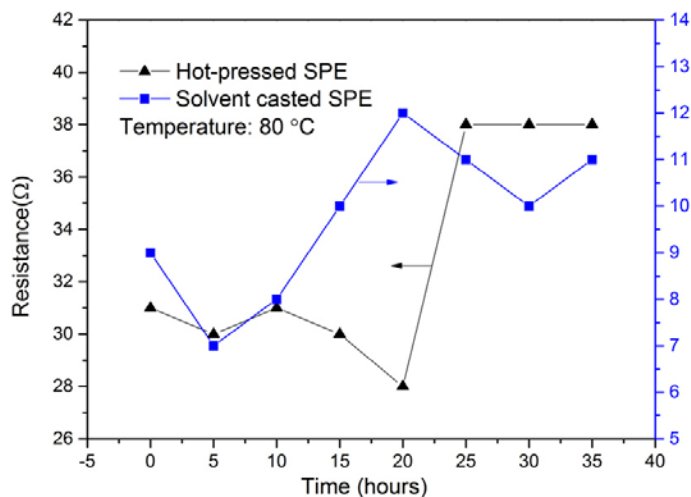
Figure 4-14 Variations of hot-pressed and solvent casted SPE conductivity with time at 80 ˚C

The variations of conductivity of hot-pressed and solvent casted SPE was presented in figure 4-14. We did not find obvious degradation of those materials even if they were stored at 80 ˚C for 35 hours. Especially for solvent casted SPE, the increased resistance was negligible compared to the LATP's resistance in a bilayer system.

4.4　Conclusion

Since our primary goal is to focus on the interfacial characterization on polymeric and inorganic ceramic electrolyte, our objective is to first characterize the single type of polymer electrolyte of SPEs and GPEs. So in this chapter, we have experimentally characterized the ionic conductivity under different temperature and fabrication methods. We also characterize the lithium ion transference number and electronic conductivities of hot-pressed SPE, solvent casted SPE and GPE. All samples have negligible magnitude to electronic conductivity, and hot-pressed SPE has the lowest one. It was proven that the addition of any liquid solvent may introduce electron conductivity. The thermos stability of those polymeric materials under high temperature of 80 ˚C

was investigated. The resistance was increased several ohms after long storage of 35 hours. We think this increase of resistance is negligible compared to the resistance of LATP in a bilayer electrolyte system.

Chapter 5. Bilayer Electrolyte Fabrication and Characterization

5.1   Introduction

Compared to the vast array of research on single types of solid electrolytes, which include ceramic/glass, ceramic, and polymeric electrolytes, research about bilayer solid electrolytes is very limited. To fabricate all-solid-state lithium ion batteries (ASSLIBs) with multi-layered solid electrolytes, the critical problem is in addressing: 1) how to fabricate the multi-layered electrolyte, and 2) how the interfacial resistance affect the conductivity of the system.

Unfortunately, the existence and the magnitude of the interfacial resistance still remains a controversial issue [17, 191]. It seems the material selection and lamination protocol have effects on the interfacial properties and interfacial impedance. So in this chapter, we explore the interface impedance with the electrochemical impedance spectroscopy (EIS) method, and through setting up the equivalent circuit, we evaluated the value of interfacial resistance. The influence of the material selection, temperature, and also the use of the lamination method was also investigated through series of experiments.

Also, we fabricated the composite SPE+ceramic fillers to investigate the transport mechanism at the polymer/ceramic grain interface. A multilayer electrolyte of LLZO sprayed on the surface of SPE was also fabricated and characterized using SEM and EIS methods.

5.2   Experimental Methods

To minimize the deviation that can be introduced by the variation of different samples, during the impedance test, all of the ceramic and polymer samples used were sintered or fabricated from the same batch.

To evaluate the material selection on the interfacial resistance, all of the ceramic materials, including LATP, LLT, and LLZO, that we synthesized were used. And different polymeric electrolytes, including hot-pressed SPE, solvent-casting SPE, and gel-type polymer electrolytes, were also used. The bilayer electrolyte was fabricated with various combination. The lamination methods include direct stacking, dip coating, and spray coating, which will be discussed next, in order.

We directly stacked the ceramic electrolyte with SPE of PEO_{10}-LiTFSI or GPE of PVdF-HFP-LiTFSI together to form a bilayer structure. The SPE and GPE was fabricated as we discussed in chapter 4. The ceramic material and pellets were synthesized/fabricated as we described in chapter 3. The bilayer electrolyte was stored at different temperatures for at least 5 hours before the AC impedance measurement.

Using dip coating, the solvent based electrolyte of PEO_{10}-LiTFSI was coated onto the surface of the ceramic electrolyte of LATP. First, LiTFSI and PEO were stored in a vacuum oven at 120 ˚C for 24 hours to remove any moisture. Then, anhydrous acetonitrile (Sigma Aldrich, 99.8%) was used to dissolve the mixture and was stirred for at least 12 hours to form a homogeneous, translucent slurry. The slurry was then de-aired with a vacuum oven for 5 mins. Then, the slurry was coated on the surface of the ceramic electrolytes to form a bilayer system. The bilayer electrolyte was placed in a dry room for at least 12 hours to allow the acetonitrile to evaporate.

The LATP and LLT ceramic powder was added as fillers to the hot-pressed SPE. The ceramic powder, PEO powder and lithium salt was placed in vacuumed oven for 24 hour to remove moisture. Before hot-pressing, those powder materials was mixed thoroughly by shaking 10 mins in a glass bottle.

We used the spray coating method to spray the ceramic particles of LLZO onto the surface of the solvent-cased electrolytes, which involved the following steps. First, a solvent-casted SPE was fabricated on the surface of a stainless steel chip. Then, the ceramic powders were dissolved in the acetonitrile solvent to form a suspension solution. We used a handgun sprayer to spray the ceramic particles on the surface of the SPE to get the bilayer structure. The bilayer electrolyte was stored in vacuum oven overnight to remove the volatile acetonitrile.

5.3 Results and Discussion

5.3.1 Morphology
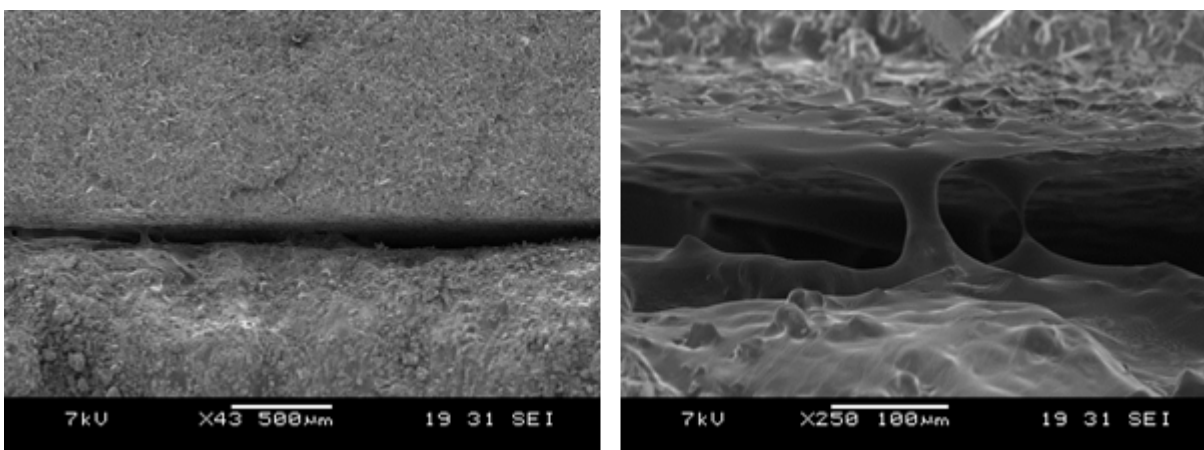
Figure 5-1 SEM image of interface between hot-pressed SPE and LATP ceramic pellets
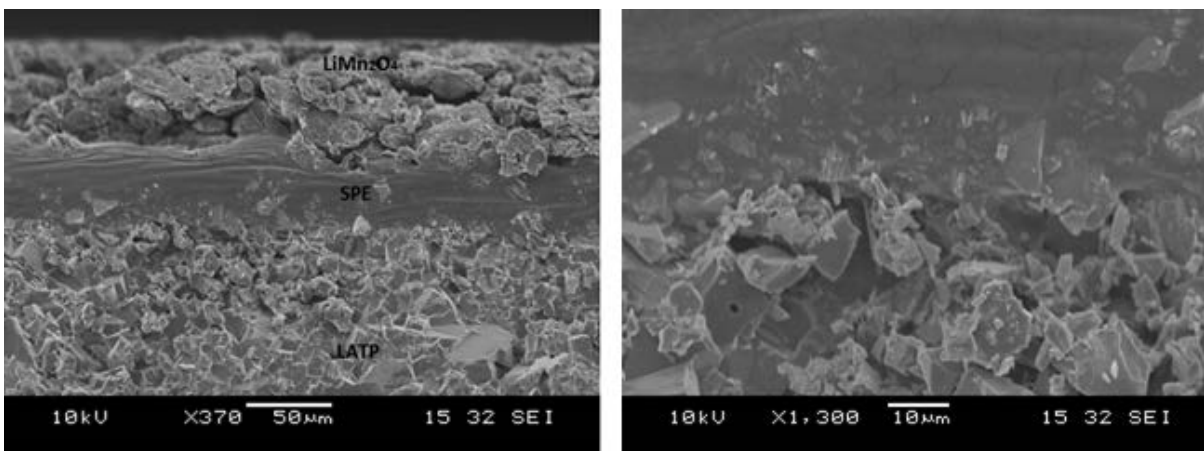
Figure 5-2 SEM image of interface between solvent-casted SPE and LATP ceramic pellets

Figure 5-1 and figure 5-2 are the SEM images of interfaces between LATP ceramic pellets with hot-pressed SPE and solvent-casted SPE respectively. From figure 5-1, we observed that the polymeric sticky SPE was barely adhered on LATP surface. There were obvious gaps existing at the verge of interface between hot-pressed SPE and LATP pellets. Due to surface tension effect, the elastic SPE body cannot maintain a sharp edge like ceramic material, so this gap at the verge of interface was enlarged. We may expect to improve the contact condition by 1) maintaining/increasing the external pressure on bilayer electrolyte, and 2) increasing the 'flexibility' of the SPE materials.

From figure 5-2, we can see a thin solvent casted SPE layer with ~30 µm thickness between $LiMn_2O_4$ cathode and LATP ceramic layer. Though it was expected that there were holes or bumps on the rugged surface of LATP or cathode material, the solvent casted SPE seems 'infiltrated' into the solid material and created a composite region, thus an intimate contact with both cathode and LATP ceramic material was achieved, and also the contact area has been augmented.
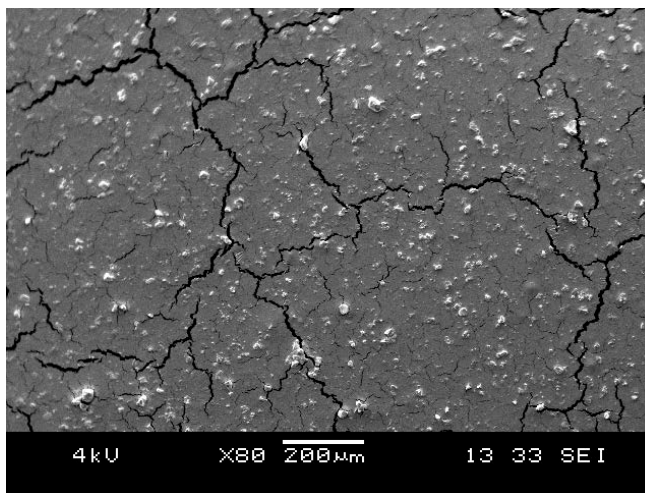
Figure 5-3 SEM image of LLZO sprayed on surface of solvent-casted SPE

Figure 5-3 is the SEM image of LLZO sprayed on the solvent-casted SPE surface. It shows that spray coating can effectively distribute the ceramic particles on the polymer surface. We can

increase the spray time for better covering the polymer surface, so as to create an ultra-thin flexible layer of ceramic stabilizer.
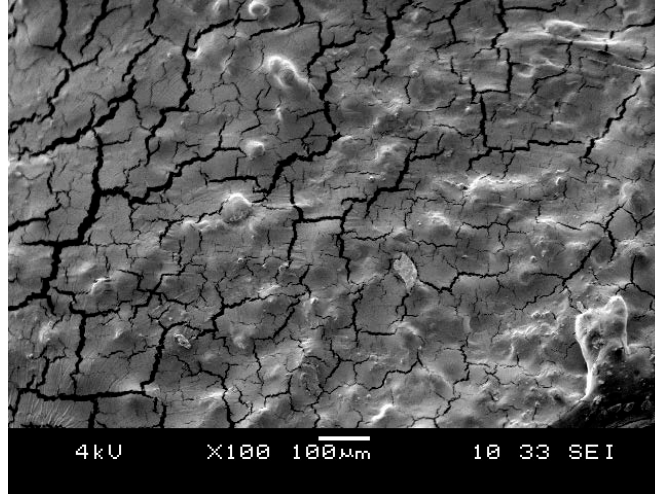
Figure 5-4 SEM image of morphology of composite SE of SPE with LATP filler

Figure 5-4 is the surface morphology of the composite SPE with LATP ceramic filler. It was demonstrated that the ceramic particles was wrapped by SPE. If using composite electrolyte as-shown directly, we doubt that it is able to isolate the contact of polymer material with lithium metal.

5.3.2   Interfacial Impedance Characterization of SPE and LATP
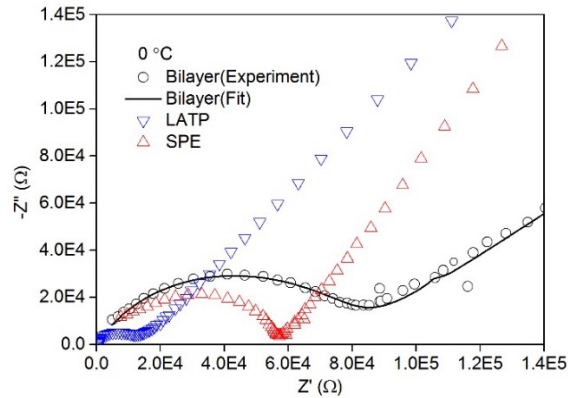
Figure 5-5 Nyquist plot of a single electrolyte of LATP, hot-pressed SPE, the experimental and fitting results of the bilayer electrolyte of LATP + hot-pressed SPE at 0 ˚C
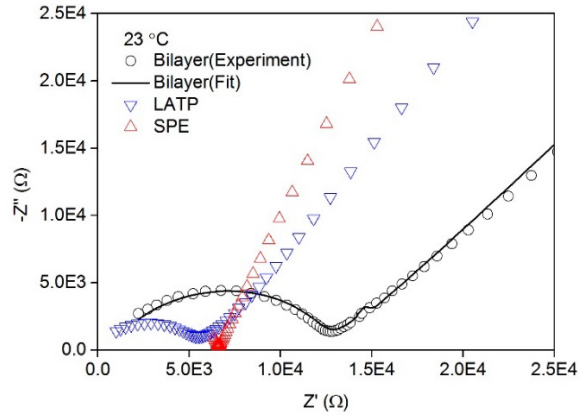
Figure 5-6 Nyquist plot of a single electrolyte of LATP, hot-pressed SPE, the experimental and

fitting results of the bilayer electrolyte of LATP + hot-pressed SPE at 23 ˚C
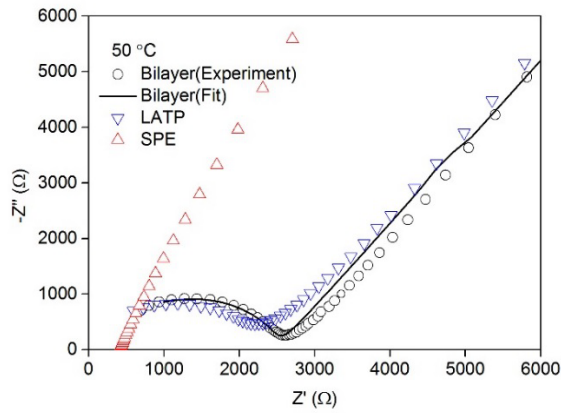
Figure 5-7 Nyquist plot of a single electrolyte of LATP, hot-pressed SPE, the experimental and

fitting results of the bilayer electrolyte of LATP + hot-pressed SPE at 50 ˚C
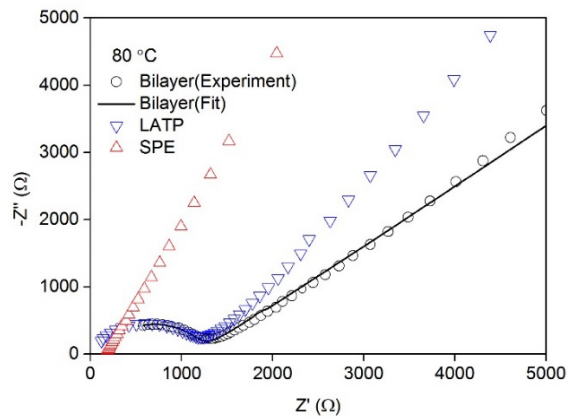
Figure 5-8 Nyquist plot of a single electrolyte of LATP, hot-pressed SPE, the experimental and

fitting results of the bilayer electrolyte of LATP + hot-pressed SPE at 80 ˚C
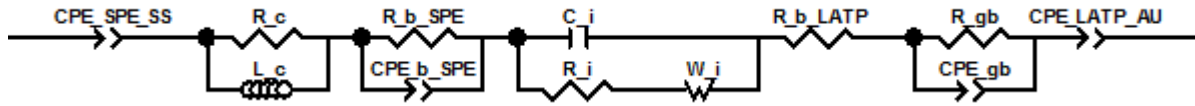
Figure 5-9 Equivalent circuit for bilayer of LATP + solid polymer electroltye electrochemical

system

Table 5-1 Elements in equivalent circuit and electrochemical representation

Element	Electrochemical representation
C_i	Electrode and electrolyte interfacial capacitance
R_i	Interfacial resistance
W_i	Warburg impedance
R_b_LATP	Bulk resistance of the LATP grain
CPE_b_LATP	Sub-diffusive ion transport in the grains
R_gb	Resistance at the grain boundaries
CPE_gb	Constant phase element at grain boundary
CPE_LATP_AU	Constant phase element of LATP sample with sputtered Au
CPE_SPE_SS	Constant phase element of SPE sample with stainless steel rod
R_c	Electric resistance from outer circuit
L_c	Inductor introduced by outer circuit
R_b_SPE	Bulk resistance of the SPE electrolyte
CPE_b_SPE	Constant phase element of SPE electrolyte

Figure 5-5, 5-6, 5-7 and 5-8 are the Nyquist plots of a single electrolyte of LATP which was sintered at 1050 ˚C, hot-pressed SPE, the experimental and fitting results of the bilayer electrolyte of LATP + hot-pressed SPE at 0 ˚C, 23 ˚C, 50 ˚C and 80 ˚C respectively. The ion transportation in the bilayer electrolyte was modeled using the equivalent circuit in figure 5-9. Table 5-1 listed all the electrochemical representations of the elements in the equivalent circuit. Through comparisons of the experimental data with fitting results, goodness of fit was found with the proposed equivalent circuit.
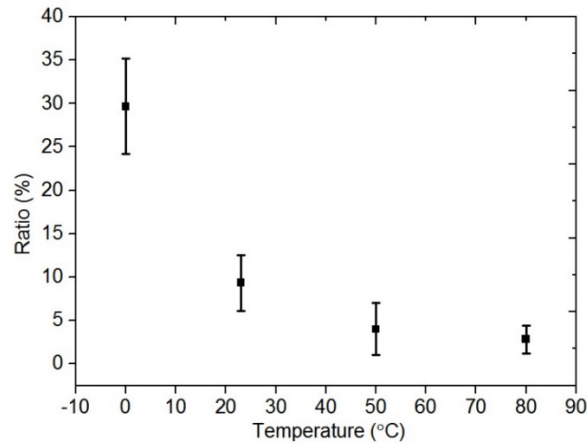
Figure 5-10 Ratio of interface resistance to total resistance of hot-pressed SPE and LATP

electrolytes

Further analysis, using the graph of the ratio of the interface resistance to the total resistance of the hot-pressed SPE and LATP electrolytes, can be seen in figure 5-10, where:

$$Ratio = \frac{R\_i}{R\_b\_SPE + R\_b\_LATP + R\_gb\_LATP} \times 100\% \qquad \text{Eq. (5-1)}$$

As we can see, the relative interfacial resistance had a decreasing trendency while the temperature was increased. At a temperature of 0 ˚C, the interfacial resistance was about 30% of the total resistance. By our observation, the SPE under 0 ˚C become stiff solid pellets. With a raising temperature, the SPE become more flexible and soft. At temperature of 80 ˚C, the

90

interfacial resistance only account for about ~3% of the total resistance. We conclude that: 1) the interface resistance may be mainly due to incomplete contact between the LATP and SPE electrolyte, and 2) higher temperatures can result in higher flexibility of the SPE material, thus improving the contact condition at the interface.

As we can see, the morphology structure of LATP varies with different sintering temperature. To see the interfacial resistance's dependence on the morphology structure, the interfacial impedance was also characterized using different LATP sample sintered at 850 ˚C, 950 ˚C and 1150 ˚C. Figure 5-11 displays the relationship between interfacial resistance and the sintering temperature of LATP ceramic sample. We did not find obvious dependence of the interfacial resistances on morphology structure of LATP.
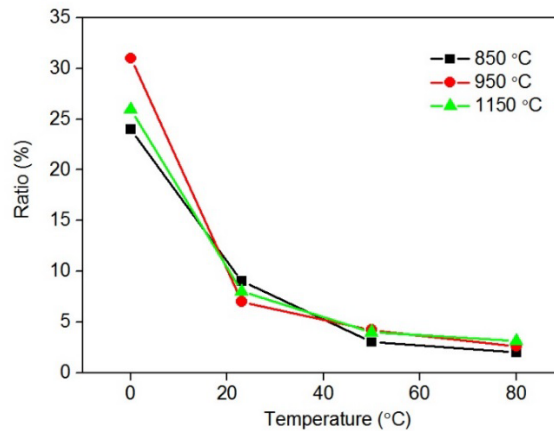
Figure 5-11 Ratio of interface resistance to total resistance of hot-pressed SPE and LATP electrolytes sintered at different temperature
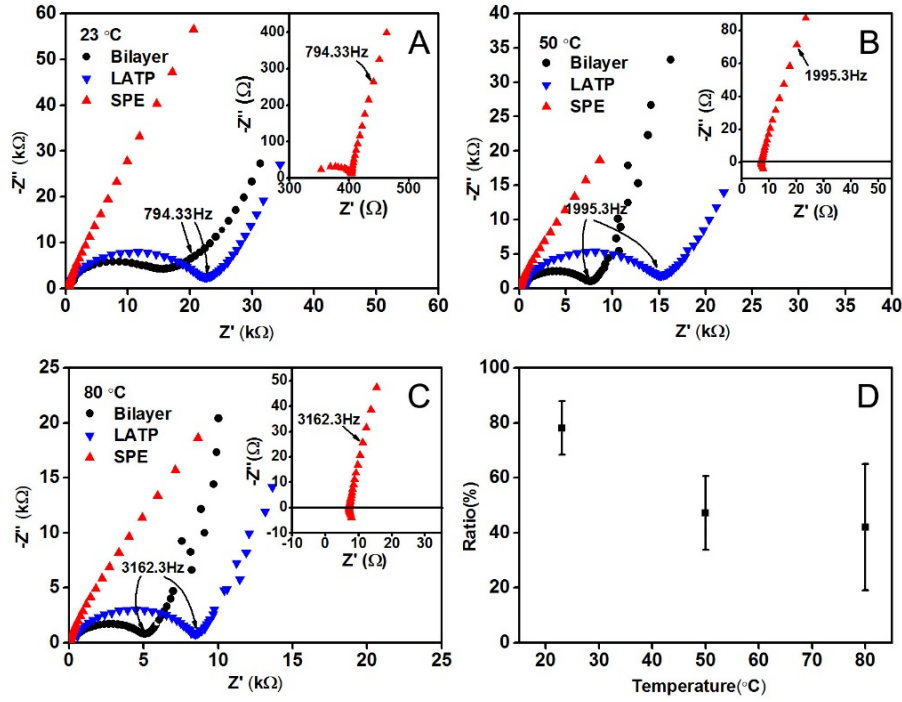
Figure 5-12 Nyquist plot of single electrolyte of Au/LATP/Au, SS (stainless steel)/solvent casted

SPE/SS and Au/LATP + solvent casted SPE/SS at A) 23 ˚C, B) 50 ˚C, C) 80 ˚C and D) ratio of

resistance of bilayer electrolyte to total resistance of SPE+LATP

Figure 5-12 A), B), C) are the Nyquist plot of single electrolyte of Au/LATP/Au, SS(stainless

steel)/solvent casted SPE/SS and Au/LATP + solvent casted SPE/SS at 23 ˚C , 50 ˚C , 80 ˚C,

respectively. The pressure exerted on the samples by the stainless steel rod was 3.88×10^4 Pa. The

thickness of the LATP pellets is ~2.7 mm. Compared with the resistance from the LATP material,

resistance of solvent casted SPE was almost negligible. One of the significant results is that the

bilayer electrolyte has lower resistance compared to the single layer of LATP. Figure 5-12D) is

the ratio of resistance of the bilayer electrolyte to the total resistance of solvent casted SPE and

LATP, which is calculated as follows,

$$Ratio = \frac{R\_bilayer}{R\_SPE+R\_LATP} \times 100\%$$ Eq. (5-1)

Rather than resulting in extra resistance at the contact interface of LATP and solvent casted SPE, the ion transfer was enhanced compared to the single layer of LATP. As the temperature increases, this enhancement effect becomes more obvious.
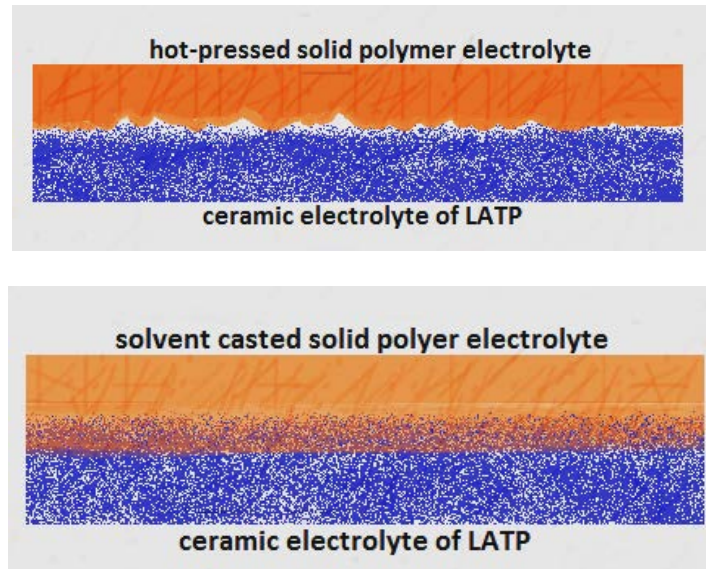
Figure 5-13 Schematic diagram of the interface of LATP and SPE

This may suggest that there is no ion transport barrier that exists at the interface between the LATP and solvent-casted SPE material, or the ion transfer at the interface was enhanced. The schematic diagram in figure 5-13 represents the interfacial condition at the interface. This diagram illustrates our presumption that: 1) the incomplete contact conditions result in the interface resistance between the hot-pressed SPE and LATP, and 2) at the interface of the solvent casted SPE and LATP, the polymer and ceramic phase form a composite or hybrid electrolyte region, which has an enhanced transportation effect.

5.3.3 Interfacial Impedance Characterization of SPE and LLT
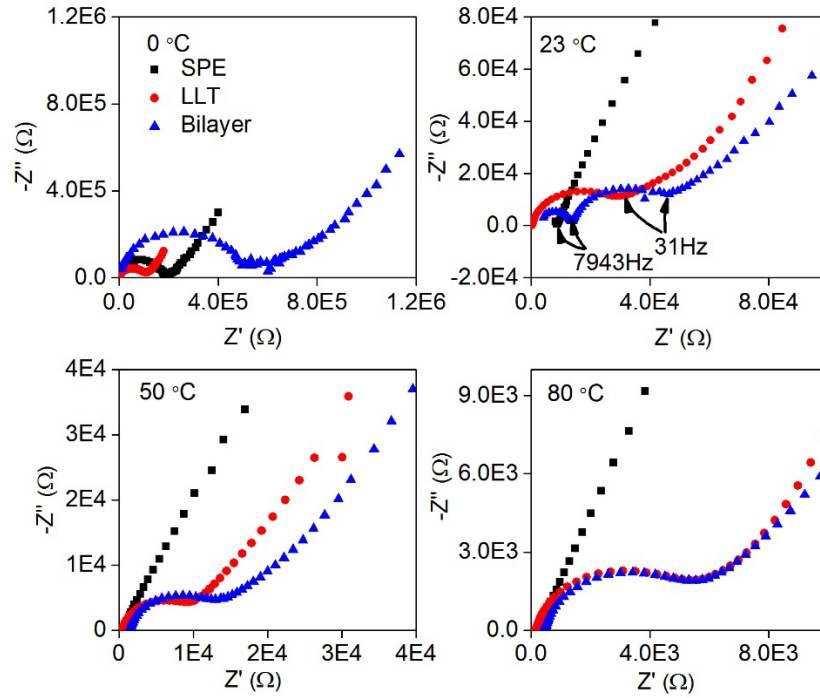
Figure 5-14 Nyquist diagram for hot-pressed SPE, ceramic LLT and the bilayer of the hot-pressed SPE and LLT at various temperature

When we use the LLT and hot-pressed SPE to construct the bilayer electrolyte, we found that there was a negligible interface resistance that exists. Figure 5-14 presents the Nyquist diagram for hot-pressed SPE, ceramic LLT and the bilayer of the hot-pressed SPE and LLT at various temperature. This result indicated the type of lithium salt may play an important role.

5.3.4 Impedance Characterization of composite SE of SPE with LATP/LLT fillers
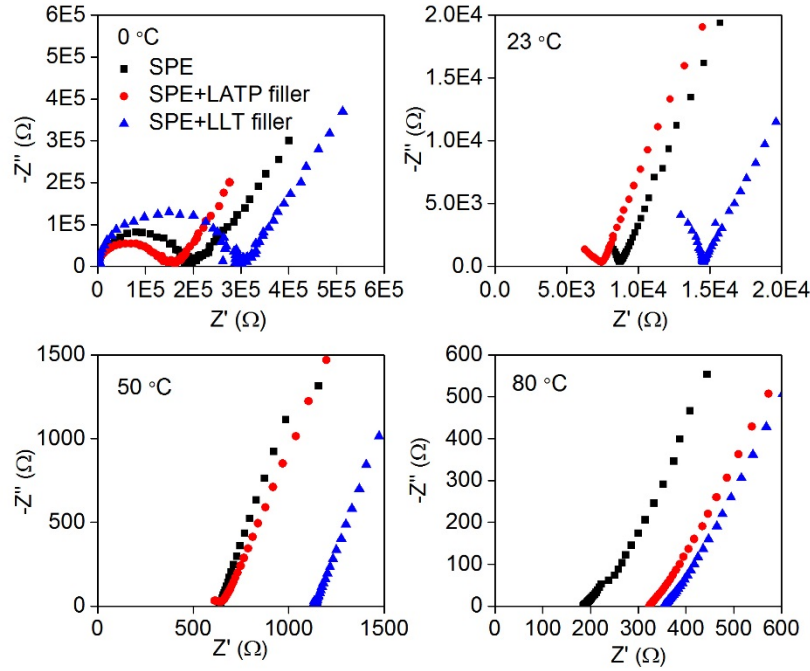
Figure 5-15 Nyquist plot of composite SE of SPE+ LATP/LLT fillers at various temperature

Figure 5-15 shows the Nyquist plot of composite SE of SPE+ LATP/LLT fillers. The weight

ratio of ceramic fillers are fixed at 20%. We found that the conductivity of SPE can be enhanced

by LATP powder filler, and decreased by LLT powder filler at different temperatures from 0 ˚C

to 80 ˚C. This indicates that the LATP filler can enhance the ion transportation in SPE, no matter

the SPE was in the state of crystalline or amorphous domination. This may suggested that there

existing enhanced transportation at the LATP filler/SPE interface.

5.3.5 Interfacial Impedance Characterization using LLZO and GPE
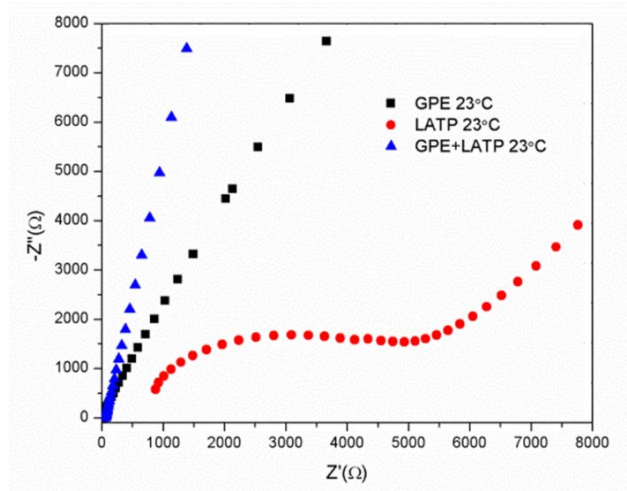
Figure 5-16 Nyquist plot of single LATP, GPE and multi-layer of GPE + LATP + GPE

Figure 5-16 is the EIS plot of the bilayer of LATP ceramic electrolyte with PVdF-HFP/LiTFSI. Compared with the resistance of LATP, the resistance of GPE was negligible. We observed that the impedance of GPE+LATP bilayer was greatly decreased compared with the single material of LATP. This interesting phenomenon may result from the fact that the liquid leakage from the gel-polymer substrate may infiltrate into the micro pores of the ceramic pellets. The presence of liquid electrolyte not only eliminated the interfacial resistance, but it also effectively enhanced the total ionic conductivity.
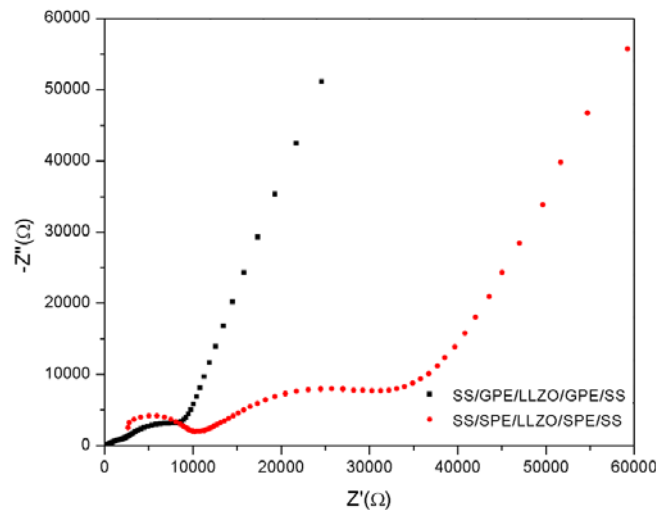
Figure 5-17 Nyquist plot of SS/GPE/LLZO/GEP/SS and SS/SPE/LLZO/SPE/SS

Figure 5-17 is the EIS plot of the bilayer of the LLZO ceramic electrolyte with GPE of PVdF-HFP/LiTFSI. The bilayer has lower resistance, however, when compared with the bilayer of the LATP + GPE; the decrease effect was not significant. This may be related to the different structures of the LATP and LLZO pellets. The LATP pellets have a more porous structure, thus the liquid electrolyte can filtrate more efficiently.
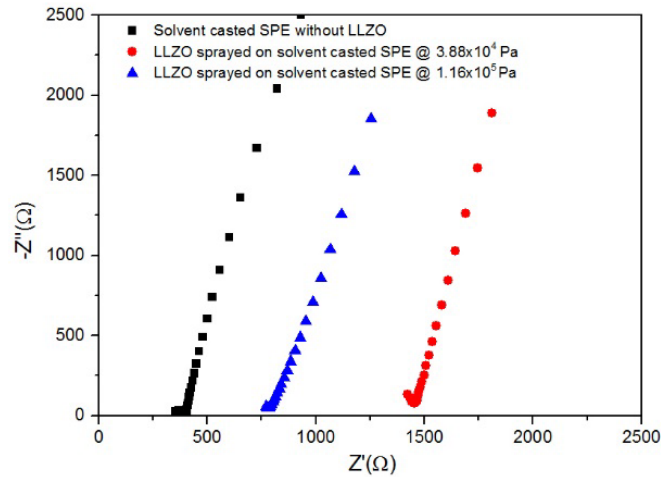
Figure 5-18 Nyquist plot of LLZO sprayed on solvent casted SPE

Figure 5-18 shows Nyquist plot of LLZO sprayed on solvent casted SPE. An additional thin layer of LLZO particles have increased the magnitude of the resistance by 2-3 times. We also found that a mildly increased pressure can effectively decrease the total resistance. This may be because the sprayed LLZO particles have a loose structure on the SPE surface, and since SPE has low modulus, pressure can improve the contact condition effectively.

5.4   Conclusion

Using the previously synthesized ceramic material of LATP, LLT and LLZO, polymeric electrolytes, including hot-pressed SPE, solvent casted SPE and GPE, we successfully fabricated different types of bilayer or multilayer electrolytes. Different fabrication or lamination protocols

were investigated, including direct stacking, spray coating, and dip coating, etc. Through SEM observation, we found an obvious difference of morphology at the contact interface using different lamination methods and materials. The dip coating of the solvent casted SPE has much more intimate contact with the LATP ceramic than the hot pressed SPE directly stacked with the LATP. This difference of contact condition at the interface may result in the different behavior of the existence and magnitude of the interfacial resistance.

By using the EIS technique, we characterized the impedance behavior of the bilayer and single layer of electrolytes at various temperatures. With the proposed equivalent circuit model of the bilayer electrolyte system, we modeled the bilayer impedance with goodness of fit and characterized the magnitude and the ratio of the bilayer resistance.

It was found that for the hot pressed SPE + LATP, the interfacial resistance takes about 30% of the sum resistance of the two independent layers at 0 ˚C. At increased temperatures, the interfacial resistance decreased rapidly. At 80 ˚C, the interfacial resistance was negligible compared with the LATP resistance. We suggest this phenomenon results from the fact that at a higher temperature, the hot pressed SPE become more flexible and shapeable, thus providing much better contact with the LATP ceramic.

The conclusion that better contacting conditions can decrease the interface resistance was further validated by the SEM image of the solvent casted SPE with the LATP. However, we found that this bilayer electrolyte has less resistance compared to a single LATP electrolyte. This indicates that the interfacial resistance was not only related with the interfacial contact condition, but also with other mechanisms that enhance the interfacial ionic transportation. We suspect that the solvent casted SPE can filtrate into the LATP ceramic, therefore a composite electrolyte was

formed. This might be similar to the "ceramic in polymer" or "polymer in ceramic" configuration with those two coexisting phase electrolytes.

It was also proved that the interfacial resistance was not obviously effected by sintering temperature of LATP pellets.

Further, we tested other types of bilayer configurations by stacking GPE and ceramic electrolyte. We also found significantly decreased impedance for the bilayer electrolyte. It was suggested that the residual liquid electrolyte may leak from the polymer matrix and infiltrate into the ceramic body. This conclusion was supported by the fact that the different porosity of the ceramic electrolyte has a different decreased magnitude of resistance.
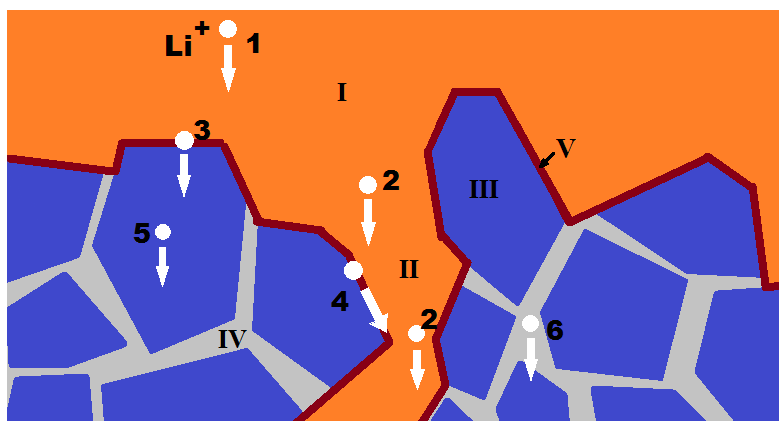
Figure 5-19 Schematic diagram of Li+ transport at the interface of the solvent casted SPE and LATP ceramic

Figure 5-19 is the schematic diagram of the Li+ ion transport at the interface of the solvent casted SPE and LATP ceramic. In this diagram, we have to consider various transport phases, which include: I) the bulk SPE phase, II) the SPE confined space, III) the bulk crystalline grain of LATP, IV) the boundary of grains of LATP, and V) the boundary interface of the SPE and LATP. The ionic transportation includes: 1) lithium ion transport in bulk SPE, 2) lithium ion transport in the confined space, 3) ion transport across the boundary of the SPE phase and LATP grains, 4) ion

transport along the boundary of the SPE and LATP grain, 5) transport in the buck grain, and 6) ion transport in the grain boundary.

This decreased resistance may result from 1) interaction of the rugged surface of LATP with solvent casted SPE can stabilize (or decrease) the amorphous region of SPE, 2) the SPE material has enhanced conductivity in the confined space at region II, 3) the transportation pathway along the SPE and LATP grains boundary at region V was established, and 4) SPE material with higher conductivity infiltrated into the body of LATP pellets via the tunnels or interspace between the LATP grains, shorten the total transport path of lithium ion, Since the resistance from solvent casted SPE only takes negligible part of the total resistance, so we assume the conductivity enhancement may contributes to the last two reason.
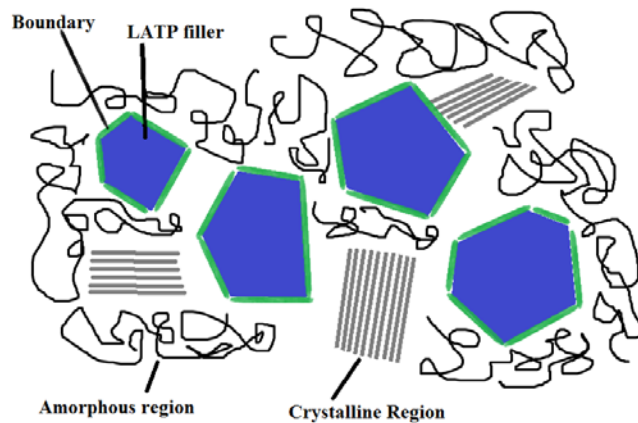
Figure 5-20 Schematic diagram of composite SPE+LATP filler
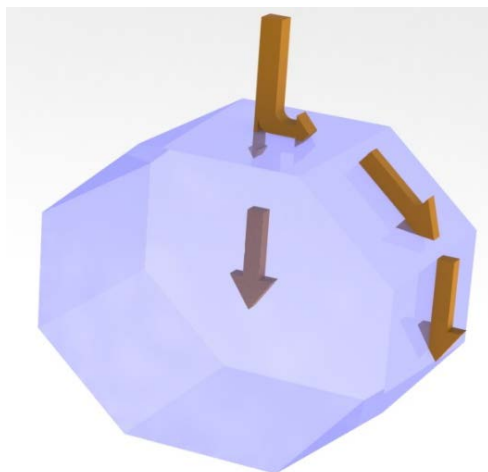
Figure 5-21 Schematic diagram of ion tranportation pathway around single LATP grain/particle

Figure 5-20 is a schematic diagram which depicts the composite solid electrolyte of SPE with LATP filler. Considering the fact that LATP filler can increase the conductivity from 0 ˚C (SPE is in crystalline state) to 80 ˚C (SPE is in amorphous state), we suggested that the LATP/SPE boundary can facilitate the ion transfer due to some reason. Figure 5-21 is schematic diagram of lithium ion transportation pathway around a single LATP grain or particle, where in the perpendicular boundary direction, subtle resistance may exist, and in the lateral boundary, ion mobility was enhanced.

Through the bilayer electrolyte fabrication and interfacial resistance characterization, we proved the feasibility of constructing the whole ASSLIBs with the as-prepared multi-layer structure electrolyte. This multi-layered electrolyte was designed to address the lithium dendrite penetration problem and also the volume change problem of the lithium metal electrode. The experimental research was also carried out and the result is presented in Chapter 6.

Chapter 6. All-Solid-State Lithium Ion Battery Assembly and Characterization

6.1 Introduction

The as-prepared multilayered electrolyte was used in a whole coin cell to test its performance. Lithium metal chip was used as an anode and spinel $Li_xMn_2O_4$ (LMO) was synthesized as cathode material. Spinel LMO is one of the most widely used cathode materials in today's commercial lithium ion batteries. Spinel LMO has a theoretical (practical) capacity of 148 (~120) mAh/g and average potential (vs. Li^0 / Li^+) ~4.1V [204].

An all-solid-state lithium ion coin cell was fabricated using the multilayer electrolyte of SPE coated on LATP. The charge/discharge properties, the cycling performance and the impedance evolvement versus cycle times were measured and evaluated, and the results will be discussed in this chapter.

6.2 Experimental Methods

6.2.1 Cathode Electrode Preparation

The cathode electrode was prepared by using $LiMn_2O_4$ as the active material, Super P carbon black as the conductive carbon, PVdF-HFP as a binder and NMP as the solvent. Before use, the Super P carbon black and PVdF-HFP binder were dried in a convection oven at 120 °C for 6 hours to remove any moisture. The preparation method was as follows: first, the binder material was dissolved in an NMP solvent. The ratio of the NMP solvent to the PVdF-HFP binder is 100 mL: 1 g. Since PVdF-HFP is hard to dissolve in NMP, the PVdF-HFP was added multiple times, while the NMP was continually stirred on a magnetic stirrer at a temperature of ~60 °C. The beaker was covered by Plastic wrap to prevent the fast evaporation of the NMP solution. After a uniform transparent solution was obtained, the active material of the $LiMn_2O_4$ powder and the Super P

carbon black was added. The mixture continued to be stirred for another 8 hours to completely mix the components. The components and weight ratio was listed in table 6-1.

Table 6-1 Components and weight ratio for cathode electrolyte

Component	Material	Ratio (wt %)
Active material	$LiMn_2O_4$ (Sigma Aldrich, > 99%, spinel)	85
Conductive Carbon	Super P carbon black (Alfa Aesar, > 99%)	8
Binder	PVdF-HFP (Sigma Aldrich, MW ~400,000)	7

The black slurry was then vacuumed in a vacuum oven for 5 mins to remove any bubbles. A little amount of the NMP was spread on the surface of a clean glass, and then the current collector of aluminum foil was spread on the dampened glass without bubbles. Then, a doctor blade was used to tape-cast the slurry onto the surface of the aluminum foil. The height of the doctor blade was ~ 150 µm. The foil was placed in a convection oven and dried at 80 °C for 8hours, then placed in the vacuum oven and dried at 120 °C for 12 hours to further remove the NMP residues. Then, the foil was pressed using the hydraulic pressing machine under the pressure of 15 MPa for 2 minutes. At last, the foil was cut using a punch cutter with a diameter of ~13mm to get cathode chips. Each cathode chip has a thickness of ~100 µm, and the load of material was ~0.0226 g/cm^2.

6.2.2 Electrolyte Preparation

The all-solid-state multilayer electrolyte was prepared. First, the solvent-casted SPE was prepared with the method we introduced in chapter 4. Before use, the SPE was de-aired using the vacuum oven to remove any air bubbles. Then, the SPE was coated on the cathode chip using a glass stick and placed in a dry room to let the volatile ACN solvent evaporate.
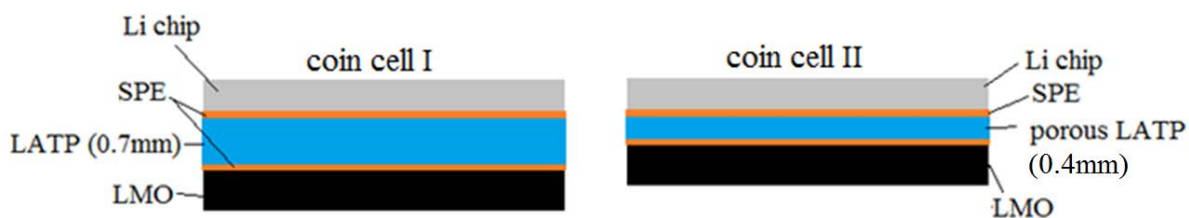
Figure 6-1 Schematic structure of two types of coin cell with different LATP chip

Using sandpaper to control the thickness of the LATP chips. To investigate the influence of total thickness/porosity of LATP on the overall performance of the battery, two types of LATP chips was prepared for the multilayer electrolyte construction: 1) LATP pellets without adding pore-maker, with the average thickness of ~0.7 mm; 2) LATP pellets sintered with pore-maker of PMMA, with the average thickness of ~0.4 mm. Before dip-coating, the LATP chips were cleaned using compressed air. The porous LATP chips were immersed in the SPE solution for 1 hour in vacuum, which may facilitate the filtration of SPE into the pores.

After slow evaporation of the CAN solution, the LATP pellets, which were coated with SPE on both sides, were carefully placed on the center of the cathode chip. Figure 6-1 depicts the schematic structure of coin cell I and coin cell II.

6.2.3 Whole Coin Cell Assembly

The coin cell was assembled in a glove box with argon as protective gas. The glove box was vacuumed first, and then flushed with argon gas. This process was repeated two times to maximally lower the concentration of oxygen and moisture. Silica gel was place inside the glovebox to further absorb any residual moisture.
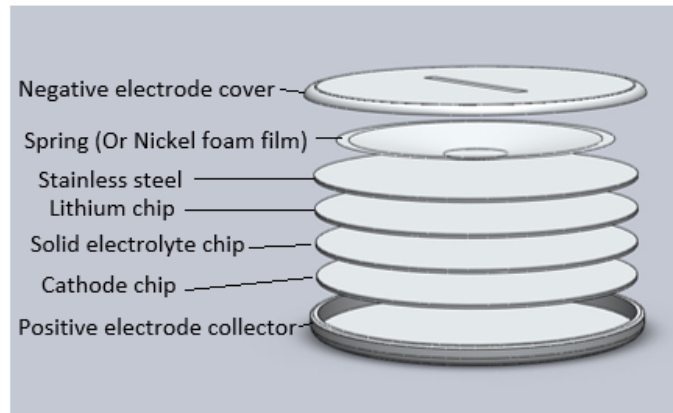
Figure 6-2 Configuration of prepared coin cell

Figure 6-3 Picture of cathode chip and LATP ceramic electrolyte inside the coin cell case

Figure 6-2 is the structure of a coin cell. The cathode chip, solid electrolyte chip and lithium chip were stacked layer by layer as in the figure. A CR2016/CR2025/CR2032 coin cell case was used, based on the total thickness of the solid electrolyte layer. After all of the components were placed in each of the coin cell cases, the cases were then placed in a zipper bag inside of the glovebox. Then the coin cells cases were taken out and pressed by a hydraulic pressing machine to be sealed. Figure 6-3 is a picture of cathode chip and LATP ceramic electrolyte chip placed inside a coin cell case before assembly.

6.2.4 Coin Cell Testing

The impedance of the coin cells was measured by a Solartron 1260+1287, and the data file was processed with Zplot/Zview software. The charge/discharge and cycling performance were measured by Neware, and the data was processed with BSTDA software.

6.3 Results and Discussion

6.3.1 Charging and Discharging Properties of Coin Cell I
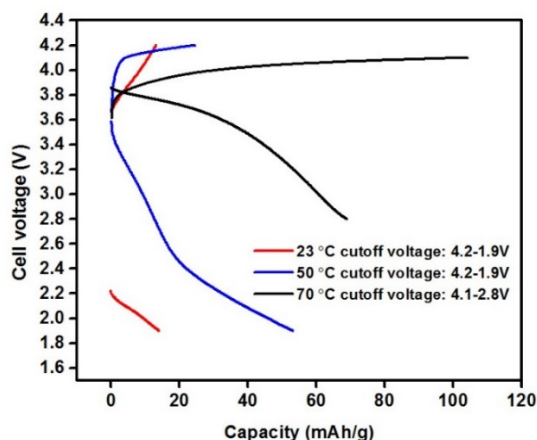
Figure 6-4 Charge/discharge voltage as a function of the specific capacity of the Li/multilayer electrolyte/ LMO coin cell at different temperatures at 1C discharge/charge rate and a different cutoff voltage

Figure 6-4 is the curve of the charge/discharge voltage as a function of the specific capacity of the Li/multilayer electrolyte/ LMO coin cell at different temperatures of 23 °C, 50 °C and 70 °C. The discharge/charge rate was 1C, and the cutoff voltage was 4.2 V to 1.9 V for tests at 23 °C, 50 °C, and 4.1 V to 2.8 V for tests at 70 °C. Thus, the charge/discharge capacity was greatly affected by temperature. This is mainly due to the fact that the solid electrolytes have a high resistance at lower temperatures.
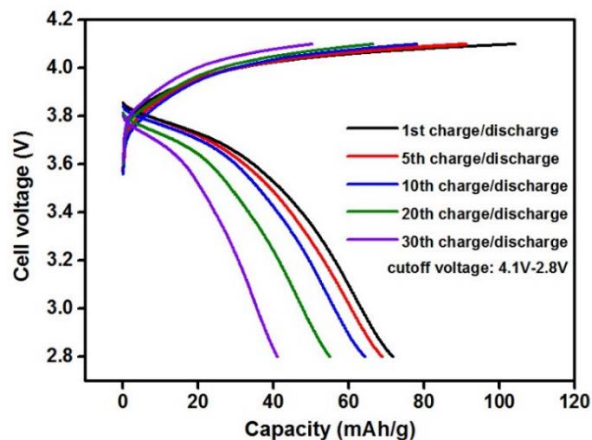
Figure 6-5 Charge/discharge voltage curve as function of specific capacity of Li/multilayer electrolyte/ LMO coin cell at different cycle times at 70 °C and 1 C discharge/charge rate

Figure 6-5 is the charge/discharge voltage curve as a function of the specific capacity of the Li/multilayer electrolyte/ LMO coin cell at different cycle times, specifically at 70 °C and a 1C discharge/charge rate. The cutoff voltage is 4.1 V to 2.8 V. The highest specific charge capacity of 104.2mAh/g and discharge capacity of 73 mAh/g was achieved at the first and second cycles, respectively.
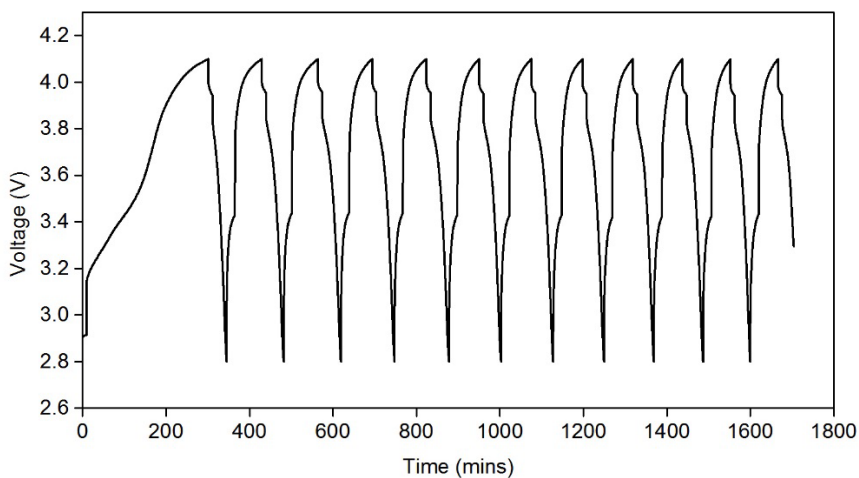
Figure 6-6 The variation of cell voltage versus time

Figure 6-6 is the plot of voltage variation versus time. We can see the cell has stable charge and discharge curve. We can also observed that the first charge last much longer than the following charge cycle. This is because the formation of SEI layer at the first time consumes more lithium ion. One thing deserve to mention is that the charge/discharge strategy we use was 1) charge at 1C, then 2) standing in open circuit for 10 mins 3) discharge at 1C and 4) standing for 10 mins again, thus a cycle was finished. We can see during the standing time, the cell's voltage was increased/decrease at charge/discharge stage. We ascribe this phenomenon to the electrode polarization.
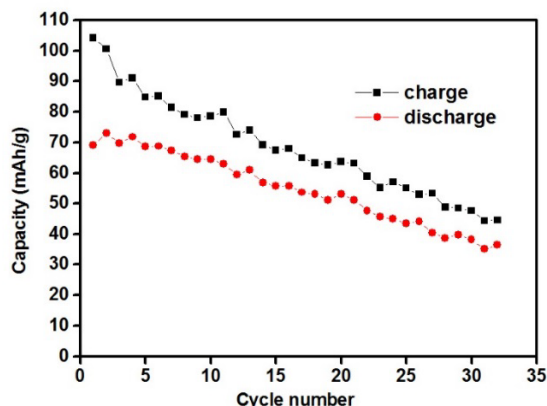
Figure 6-7 Charge/discharge-specific capacities as a function of the cycle number of the

Li/multilayer electrolyte/ LMO coin cell at 70 °C and a 1C discharge/charge rate

Figure 6-7 shows the charge/discharge-specific capacities as a function of the cycle number of the Li/multilayer electrolyte/ LMO coin cell at 70 °C, the discharge/charge rate was 1C. Both the charge and discharge capacity decayed with the cycle number. This may be related to the unstable interface of lithium metal with the solvent casted SPE. The residue existence of the ACN or other organic impurities in solvent casted SPE can react to the lithium metal irreversibly, and the high temperature of 70 °C accelerates this reaction. This reaction formed an SEI (solid-electrolyte interphase) layer on the lithium anode. The thickness of SEI grows with the cycle

number and operation time. The high voltage may also contribute to the decomposition of the organic components, thus facilitating the development of an SEI layer. This phenomenon is also the main reason for capacity fade for the commercial liquid electrolyte LIBs, for which the SEI layer exists at the negative electrode [205]. A composite electrolyte of solvent casted SPE with inert ceramic fillers can help to stabilize this electrolyte/electrolyte interface. Or, we proposed that to spray another thin layer of LLZO ceramic particles onto the surface of the SPE may also help. The LLZO ceramic particles can 1) provide a transport path because of the LLZO's high conductivity, and 2) decrease the extent of the exposure of the lithium metal to the SPE solvent. Another reason for a decreasing charge/discharge capability may be related to the transference number of SPE, the bulk anions of organic residue can disrupt the structure of LMO during the intercalate/deintercalate process. Ceramic fillers may also improve the transference number and thus alleviate this issue.
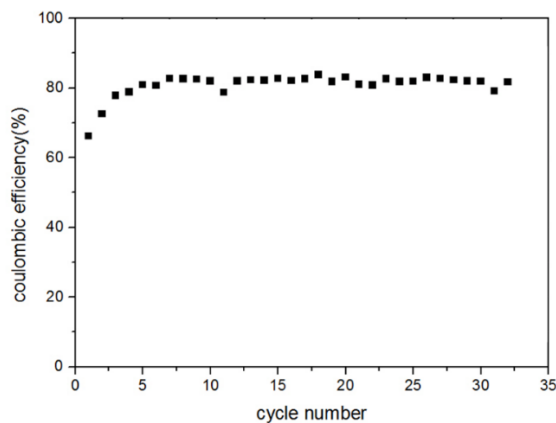
Figure 6-8 Coulombic efficiency as a function of the cycle number of the Li/multilayer electrolyte/ LMO coin cell at 70 °C and a 1C discharge/charge rate

The as-prepared coin cell's coulombic efficiency as a function of the cycle number at 70 °C and a 1C discharge/charge rate is plotted in figure 6-7. After a period of stabilization process during the initial cycles, the coulombic efficiency was stabilized at ~82 %.

6.3.2 Impedance Characterization of Coin Cell I
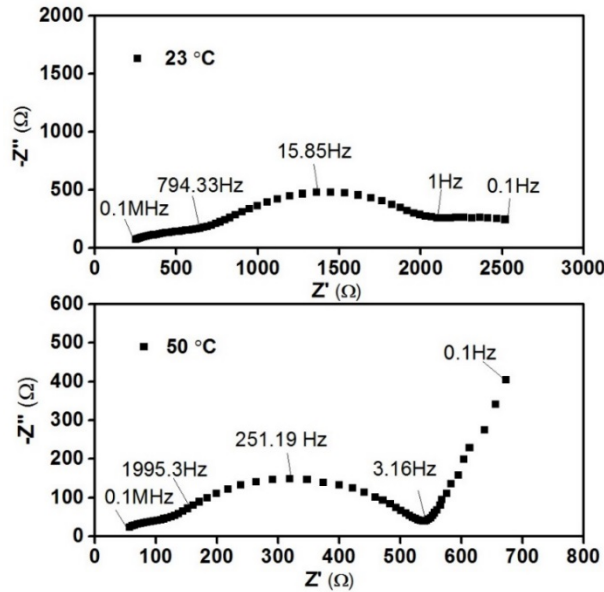
Figure 6-9 Impedance of the Li/multilayer electrolyte/LMO coin cell at 23 °C and 50 °C
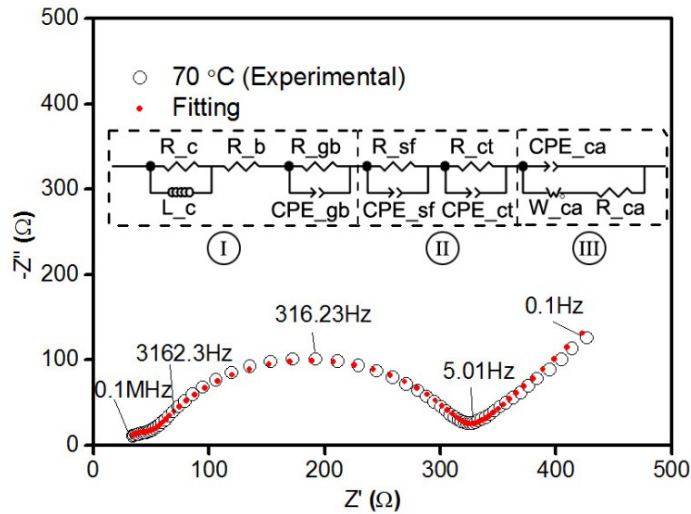
Figure 6-10 Experimental and fitting impedance of the Li/multilayer electrolyte/LMO coin cell at

70 °C, and the equivalent circuit model

The impedance of Li/multilayer electrolyte/LMO coin cell was measured at 23 °C and 50 °C

and is presented in figure 6-9. The impedance of the cell at 70 °C is shown in figure 6-9 and fitted

using the equivalent circuit model in the inset. The typical impedance response of the cell was

composed with a small semi-circle at high frequency, a large semi-circle at medium frequency, and an oblique straight line with slope of ~45° at low frequency. The impedance can be well fitted using the proposed equivalent circuit. Based on the comparison of the characteristic frequency from figure 5-10, we assume that the equivalent circuit was mainly composed of three corresponding parts, as shown in figure 6-10. From high frequency to low frequency, they represent 1) ion transfer in the multilayer electrolyte, 2) ion transport across interface of lithium/polymer electrolyte and 3) ion diffusion at cathode respectively. As shown, the main resistance was the charge transfer resistance between the lithium metal and SPE.

It is not surprising that the total resistance of the cell decreased with increasing temperature. We listed the electrochemical representation of elements in equivalent circuit and value in fitting in Table 6-2. The main resistance was the charge transfer resistance between the lithium metal and SPE.

Table 6-2 Electrochemical representation of elements in equivalent circuit and values

Element	Electrochemical representation	Value
R_c	Electric resistance from outer circuit	0.78 Ω
L_c	Inductor introduced by outer circuit	7.59E-7 F
R_b	Bulk resistance of multi-layered electrolyte	12 Ω
R_gb	Resistance at the grain boundaries of LATP	28 Ω
CPE_gb	Constant phase element at grain boundary	T = 2.31E-6 F
		P = 0.765
R_sf	Surface film resistance	10 Ω
CPE_sf	Surface film constant phase element	T = 8.60E-8 F
		P = 0.867

R_ct	Charge transfer resistance	266.4 Ω
CPE_ct	Charge transfer constant phase element	T = 1.02E-5 F
		P = 0.800
CPE_ca	Constant phase element at cathode interface	T = 1.34E-8 F
		P = 0.722
W_ca	Finite length Warburg impedance	R = 0.214 Ω
		T = 1.438E-5 F
		P = 0.286
R_ca	Resistance at cathode	2.85 Ω
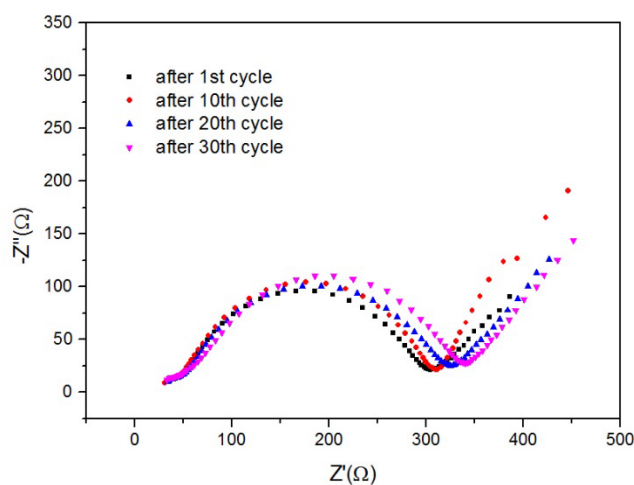
Figure 6-11 Impedance development versus cycling number at 70 °C, 1C charge/discharge rate

By measuring the EIS of the Li/multilayer electrolyte/ LMO coin cell after different cycle times at 70 °C and a 1C charge/discharge rate, we got the impedance development versus cycling number, as shown in Figure 6-11. The most distinguishable difference was a growing charge transfer impedance. Again, we attribute this to the growing resistive SEI layer, which was generated by the irreversible reaction of the lithium anode to the unstable solvent casted SPE. A

higher operating temperature and potential, and also the solvent residue or other organic impurities, may accelerate the SEI growth. While the SEI becomes thicker, it impedes the lithium transfer at the interface, as we can see from the Nyquist plot in figure 6-11. Also, the SEI growth consumes the lithium ions irreversibly, thus further degrading the charge/discharge capacity.

From the Nyquist plot, we can see the total resistance by multilayer electrolyte was much less significant compared with the charge transfer resistance. The unstable SEI layer at the lithium electrode seems to be the main thing that inhibits the performance of the total system. As we have mentioned, another multilayer electrolyte with a sprayed LLZO layer on the SPE surface may provide a solution to this problem.

6.3.3 SEM Image of Solid Multilayer Composite Electrolyte
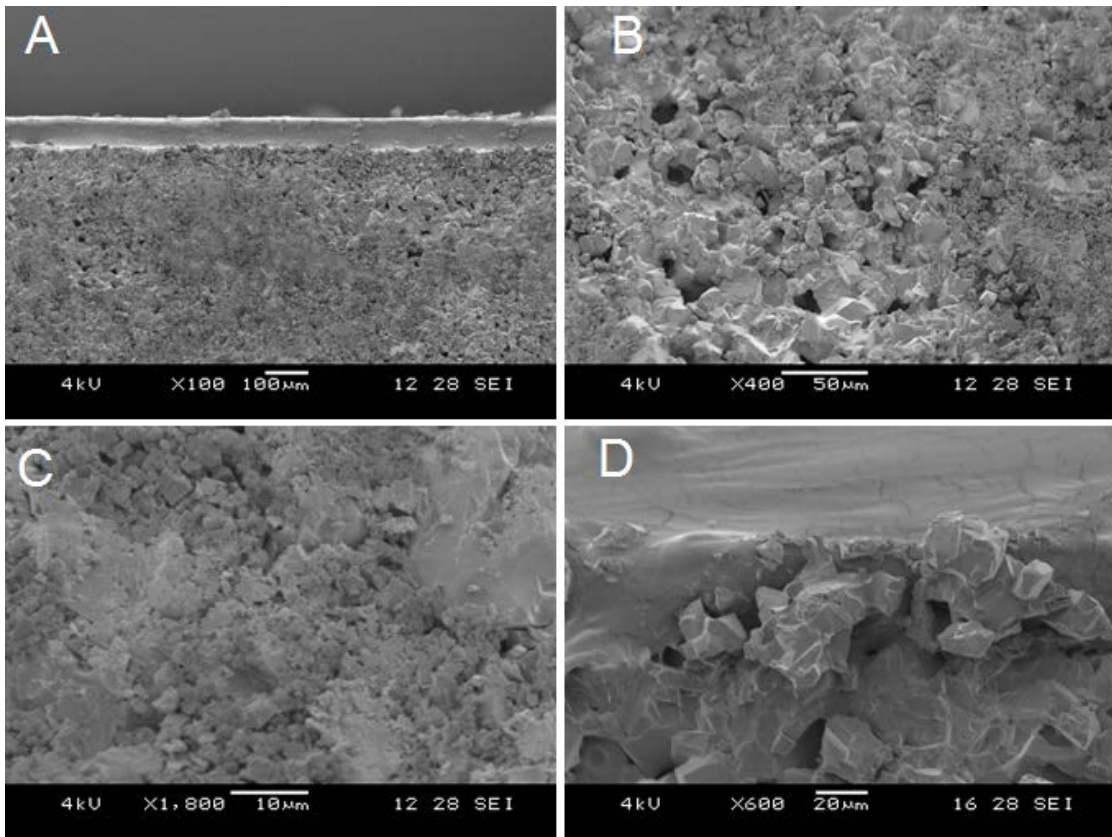
Figure 6-12 SEM image of the as-prepared multilayer composite electrolyte

Figure 6-12 is the SEM image of the as-prepared multilayer composite electrolyte. The microstructure of the electrolyte was presented at different magnification. From the image, we can observed that 1) the polymer electrolyte with uniform thinness ~50μm was formed on the ceramic electrolyte substrate (Figure 6-12 A), 2) the interface between the polymer and ceramic electrolyte has very intimate contact (Figure 6-12D), and 3) the porous LATP ceramic was partially filled with polymer electrolyte (Figure 6-12 B,C).

6.3.4 Charging and Discharging Properties of Coin Cell II
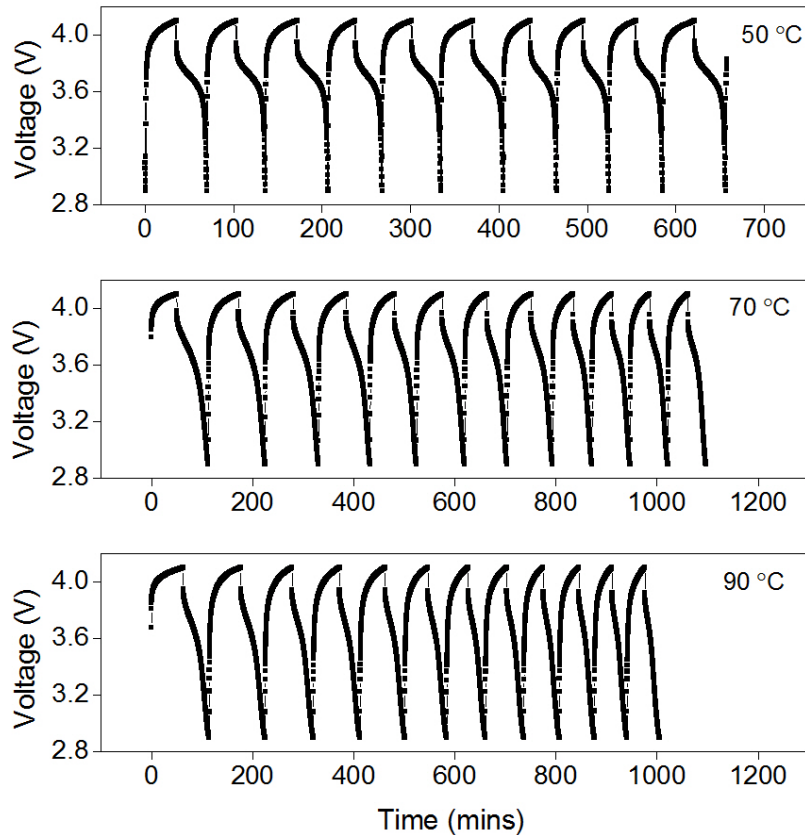
Figure 6-13 Variation of cell voltage versus time at different temperature and different cycles

Figure 6-13 demonstrated the variation of voltage versus time at different temperature and different cycles, the charging/discharging current was: 0.2 mA/cm^2 at 50 °C and 0.26 mA/cm^2 at 50 °C and 90 °C. It shows that the cell has stable voltage output during charging/discharging cycles.
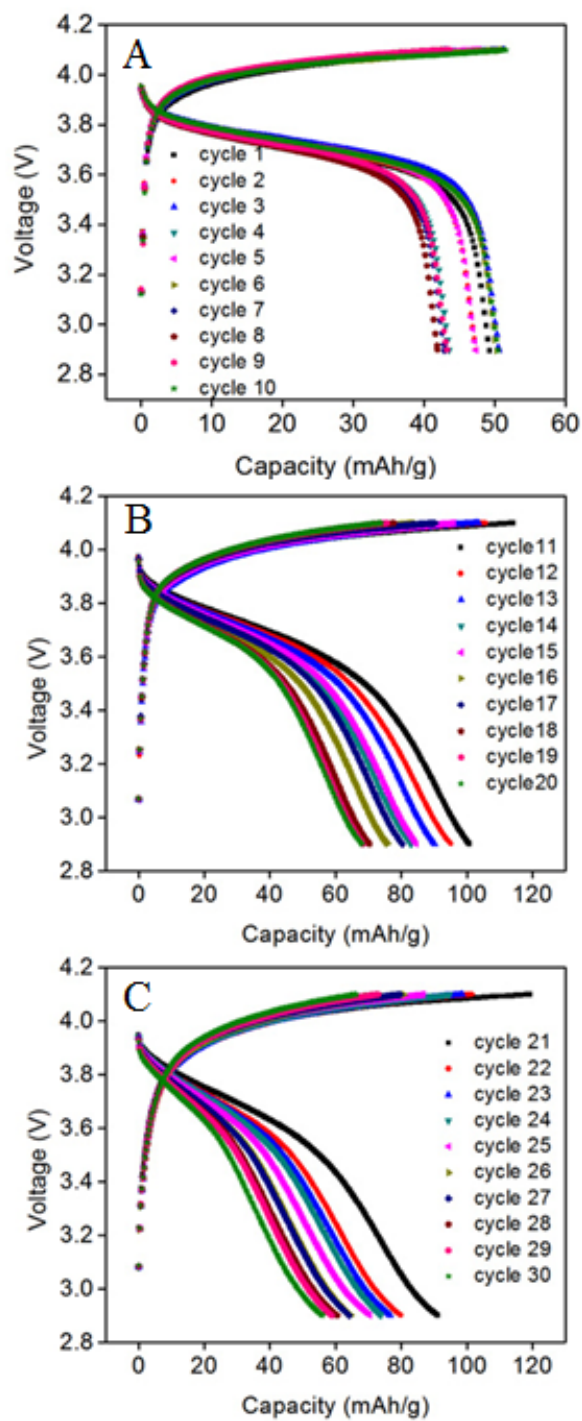
Figure 6-14 Variation of cell voltage versus capacity at different cycles and temperatures: A) 1-10 cycle (at 50 °C) and B) 11-20 cycle (at 70 °C) and C) 21-30 cycle (at 90 °C)

Figure 6-14 is the Variation of cell voltage versus capacity at different cycles/temperature: A) 1-10 cycle/50 °C and B) 11-20 cycle/70 °C and C) 21-30 cycle/90 °C. We can see the coin cell demonstrated good discharge properties with flat discharge plateau. The cell has higher discharge plateau at lower temperature, which is because the cell has higher electrode polarization at lower temperature.
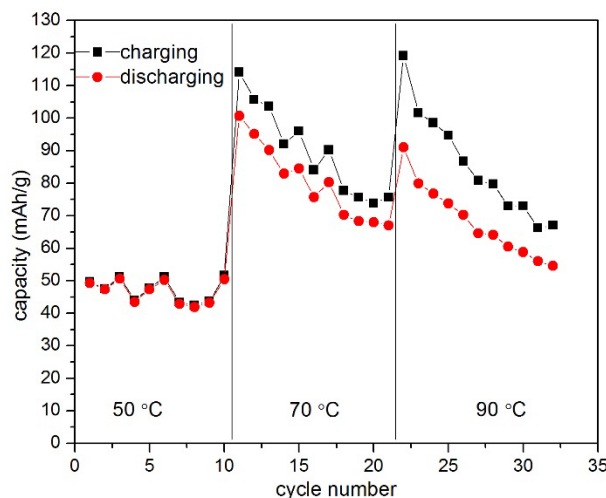
Figure 6-15 Charge/discharge capacity at different cycle numbers and temperatures

Figure 6-15 shows the charge/discharge capacity at different cycle numbers and different temperatures. We can see that at 50 °C, both charge and discharge capacity keeps a low value and oscillate at 50 mAh/g at the first 10 cycles. At the next 10 cycles at 70 °C, the charge/discharge capacity both was increased due to the lower internal resistance, but the charge/discharge capacity also decreased versus cycle number. This capacity fade becomes more obvious when the coin cell was operated at 90 °C. This phenomenon is related to the fact that the organic solvent may become more unstable at higher temperature, thus deteriorate the electrode/electrolyte interface and causes capacity loss.
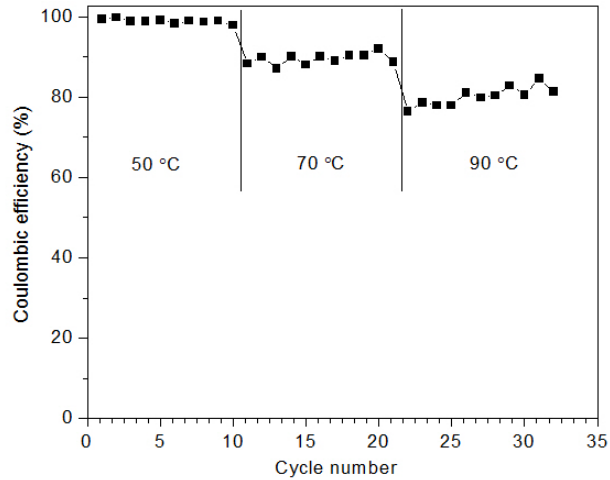
Figure 6-16 The Coulombic efficiency change at different cycle numbers and temperatures

Figure 6-16 shows the variation of Coulombic efficiency at different cycle numbers and temperatures. We found higher temperature causes lower Coulombic efficiency. This is because at higher temperature, the electrode polarization was decreased, and the conductivity of the electrolyte/electrode was increased.

6.3.5 Impedance Characterization of Coin Cell II
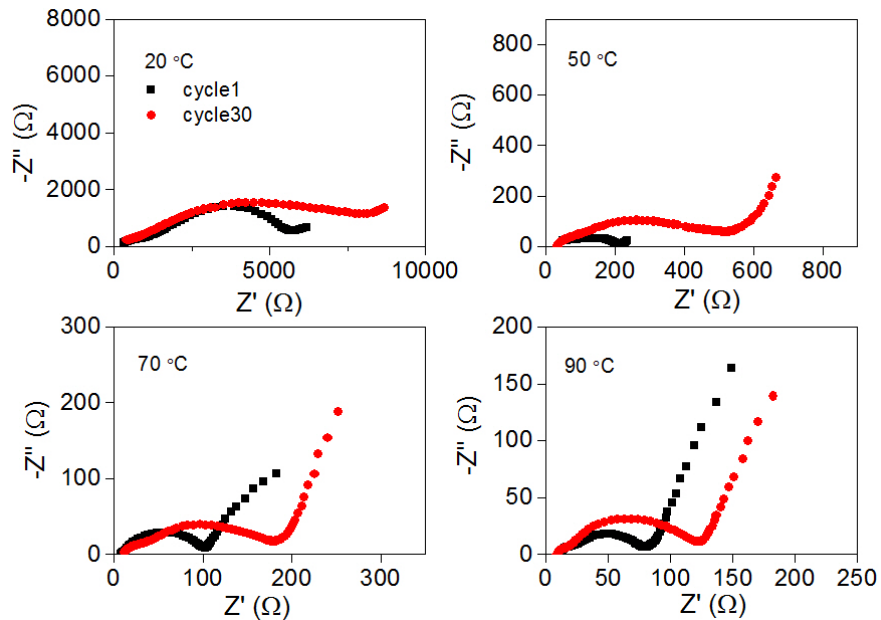
Figure 6-17 Impedance development of the cell after 30 times cycle

Figure 6-17 shows the impedance change before/after 30 times cycles. We can see the charge transfer resistance remains the dominant contribution to the overall internal resistance of the cell. Also, since the thickness of the multilayer electrolyte was decreased, the total resistance was decreased about 50% compares with the coin cell I.
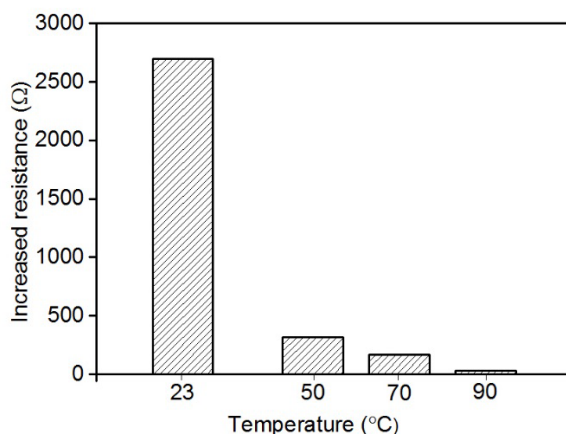
Figure 6-18 Value of increased resistance before/after 30 cycles in different temperature

Figure 6-18 shows the increased resistance before/after 30 cycles in various temperatures. We can see this increased resistance was also decreased when the temperature was increased. This increased resistance mainly comes from the SEI layer development.

6.4   Conclusion

The all-solid-state lithium ion coin cell was successfully fabricated using the multilayer electrolyte of the SPE coated on LATP. The charge/discharge properties, the cycling performance, and the EIS profiles were measured and presented in this chapter.

Two types of coin cell with different LATP chip was fabricated. The as-prepared lithium ion coin cell I with the all-solid-state electrolyte had a considerable performance, with up to 30 cycles at 70 °C and a 1C charge/discharge rate with a cutoff voltage of 4.1 V to 2.8 V. The coulombic efficiency was stabilized at ~82 %. The charge/discharge capacity decreases gradually with the cycle numbers. This battery's performance degradation may mainly result from the irreversible

reaction at the lithium electrode/solvent casted SPE interface. To investigate the reaction and transportation mechanism inside the battery, we set up an equivalent circuit to model the electrochemical processes involved during the cycling. The equivalent circuit can fit the experimental data well.

Through the EIS characterization and modeling analysis, the degradation of the battery was attributed to the unstable interface of the lithium electrode and the solvent casted SPE. The charge transfer resistance, resulting from the growth of the SEI layer, accounts for the main part in the total impedance of the system. The higher temperature of 70 °C, also the high voltage may cause SPE decomposing and may also accelerate the reaction of the vulnerable lithium with the SPE. Using a composite electrolyte with inert ceramic fillers was proven to be beneficial to stabilize the lithium/SPE interface. We suggest that using a multilayer stable LLZO conductor ceramic electrolyte sprayed onto the SPE surface may also help to create a favorable interface by lowering the exposure of the lithium electrode to the organic electrolytes.

For the coin cell II, we found thinner LATP chip with porous structure can enhance the overall performance, since the batteries exhibited good rechargeable capacity at 50 °C. In higher temperature condition, the capacity can be increased due to higher conductivity of electrolyte, however, the capacity fade is much obvious since the unstable electrolyte/electrode interface.

Chapter 7. Conclusions and Future Work

7.1   Conclusions and Summary

All-solid-state lithium ion batteries have great potential for their advantages, especially when compared with traditional lithium ion batteries that use liquid electrolytes; for example, they have improved safety in abused conditions and at high temperatures, improved capacity considering the lithium metal can be applied as an anode electrode, and shape design flexibility, etc. It was expected that all-solid-state batteries might be applied and used in the electrical vehicles industry or stationary power storage facilities in the future. However, there are still critical issues and challenges for those ASSLIBs before their application in practice. Those problems include the high resistance of the solid electrolytes, volume change problems during the charge/discharge cycling, and the degradation of the lithium metal when it comes in contact with the organic electrolytes, etc.

Based on previous research on the different types of organic polymer electrolytes and inorganic ceramic electrolytes, we proposed to investigate and develop a novel concept for a multilayer electrolyte that can combine the merits of those different types of electrolytes. Specifically, we aimed to address the volume change and poor solid-solid contact between electrodes and the electrolyte problem with an adhesive, flexible thin layer of solvent casted polymer electrolytes coated onto the ceramic electrolyte. This thin polymer electrolyte not only functions like "glue" to connect the electrolyte and electrode, but we also found that this thin layer can effectively decrease the total resistance of the multilayer electrolyte when we use LATP as the ceramic counterpart. Through SEM pictures and EIS characterization, we suggest that there may exist a composite multiphase layer at the interface, which has enhanced transportation of the lithium ions.

Based on the electrochemical and physiochemical characterization of single and bilayer electrolytes, we successfully fabricated and assembled the coin cell ASSLIB prototype with the multilayer all-solid-electrolytes. This ASSLIB prototype has demonstrated satisfactory performance at the high temperature of 50 °C, 70 °C and 90 °C, with high reliability, high voltage output and good enough cycling properties.

Through this series of experiments, we believe the construction of ASSLIBs with the multilayer electrolyte is feasible and promising. Before any practical batteries are assembled, however, several critical issues should be addressed. First, a lower ionic resistance multilayer electrolyte is required. We suggest future research that include 1) investigating new lithium ion conductors, 2) clarification of the conductivity enhancement mechanism of the solvent casted SPE and LATP ceramic and tries to understand the transport mechanism at the interface of polymer chains with ceramic grains, and 3) fabrication of thinner ceramic or glass-ceramic conductors. Second, a stable interface between the lithium electrode and polymer electrolyte is essential to retain good cycling performance and prolong battery life. This is especially critical for ASSLIBs operated at an elevated temperature, since higher temperatures accelerate the organic electrolyte components' decomposition, and thus, deteriorate the interfacial stability. A composite electrolyte with ceramic stabilizer was suggested to enhance the stability and lithium ion transference number. We proposed the use of a multilayer electrolyte with a high conductivity ceramic material of LLZO sprayed onto the SPE surface.

7.2   Recommendations for Future Work

We have fabricated the LATP ceramic pellets with a dry-pressing method with a die and hydraulic press machine; after sintering, the pellets were polished with sandpaper by hand. This fabrication method has many limitations: it cannot provide uniform equality of product samples

and the efficiency is very low. Besides, the samples' thickness is also limited. In future work, the glass-ceramic type LATP should be investigated. Compared to the ceramic electrolyte, a glass-ceramic LATP has a higher mechanical strength, and thus, thinner plates could be fabricated. We suggest the ceramic or glass-ceramic electrolyte should maintain a thinness below 100 µm, without losing the mechanical strength to suppress lithium dendrite growth. Such a thin solid electrolyte was expected to have a higher conductivity, more than 7 times better than the prototype we have fabricated, which may make it possible to make the battery practical. An ultra-thin ceramic or glass-ceramic could be fabricated to be flexible, which would be beneficial for a more flexible design of battery structure.
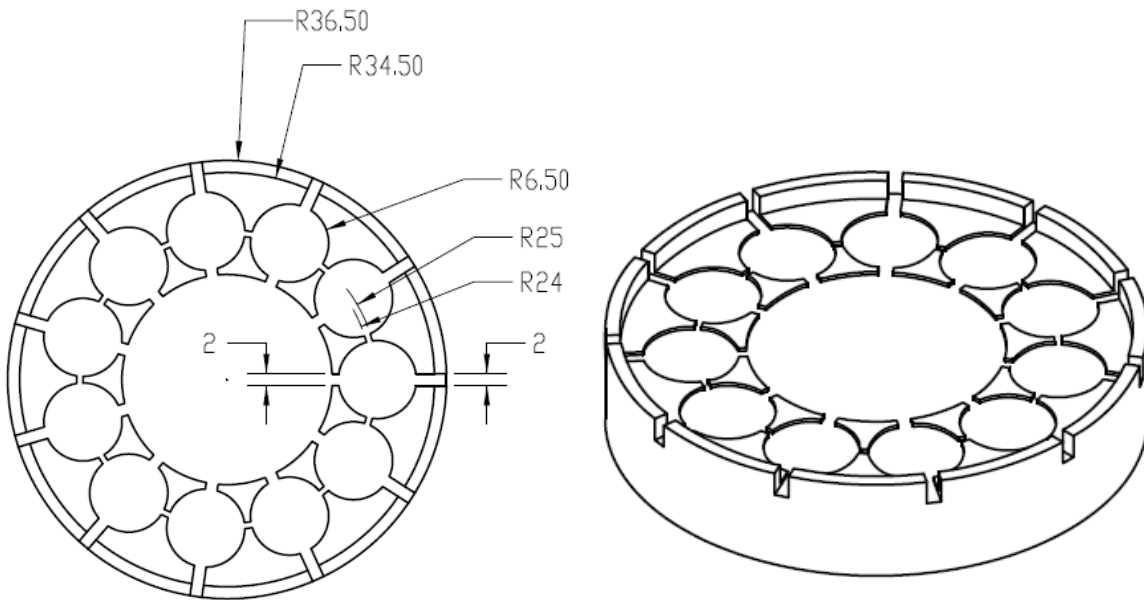
Figure 7-1 Design of brass mold for glass-ceramic LATP fabrication

A glass-ceramic LATP will be fabricated by melting LATP powder in a furnace at temperatures higher than 1450 °C. Then, this melted slurry will be poured on the preheated surface of a brass mold and pressed with another brass bar. The quenched plates will be annealed to relief the internal stress and allow the grain growth for several hours to get the glass-ceramic. Figure 7-

1 is the design for the brass mold for the glass-ceramic LATP fabrication. In this way, the glass-ceramic LATP electrolyte can be fabricated with more uniform quality and efficiency.

By making the glass-ceramic LATP thinner, its conductivity would be compensated. However, since the existence of interfacial resistance may be related to the morphology of the LATP surface, we need to characterize the bilayer of the solvent casting SPE and glass-ceramic LATP.

The ionic transport mechanism at the ceramic/polymer interface remains unclear. We suggest more experimental and theoretical research to be carried out at the interface of PEO-based polymer electrolyte with ceramic grains. From figure 5-19, we can see that the interface transportation happens in complex phases and conditions. We suspect that the ion transports along the boundary of the SPE and LATP, also in this confined region the SPE was enhanced. However, more experimental research is needed to provide proof.

More experimental research on fabricating the porous ceramic structure which possess good mechanical strength and high porosity is needed. Different sintering temperature, material selection and synthesis methods can be further explored.

The multilayers of the LLZO sprayed onto the SPE should be further investigated. With the lithium as an anode electrode, the LMO as a cathode electrode, the LLZO sprayed onto the SPE as a multilayer electrolyte can be assembled and characterized. The cyclability at elevated temperatures should be investigated experimentally.

Also, the bilayer constructed with GPE and a thin ceramic electrolyte should be further investigated. This involves the interface between the liquid with solid electrolytes. A multilayer structure with GPE + a ceramic electrolyte + GPE is promising as a bulky type of ASSLIB. Such multilayer electrolyte may provide high conductivity, considering that the liquid electrolyte can

penetrate the porous ceramic layer. Another advantage worth mentioning is that both the GPE and ceramic electrolyte can be fabricated through tape casting method, thus enables a more flexible ASSLIBs shape and dimension design. However, its capability of alleviating the volume change effect and the stability of GPE versus lithium metal at elevated temperature remains a question.

References

[1]   Tarascon J.-M. & Armand M. Issues and challenges facing rechargeable lithium batteries. *Nature* **414**, 359-367 (2001).

[2]   Goodenough J.B., & Kyu-Sung Park K.-S. The Li-Ion rechargeable battery: A perspective. *J. Am. Chem. Soc*. **135**, 1167-1176 (2013).

[3]   Armand M. & Tarascon J.-M. Building better batteries. *Nature* **451**, 652-657 (2008).

[4]   Scrosati B., & Garche J. Lithium batteries: Status, prospects and future. *J. Power Sources* **195**, 2419-2430 (2010).

[5]   Pillot G. The worldwide battery market 2011-2025. *Batteries 2012*, (2012).

[6]   Fergus J.W. Recent developments in cathode materials for lithium ion batteries. *J. Power Sources* **195**, 4554-4569 (2010).

[7]   Mohri M.,Yanagisawa N., Tajima Y., Tanaka H., Mitate T., Nakajima S., Yoshida M., Yoshimoto Y., Suzuki T. & Wada H. Rechargeable lithium battery based on pyrolytic carbon as a negative electrode. *J. Power Sources* **26**, 545-551 (1989).

[8]   Aurbach D., Talyosef Y., Markovsky B., Markevich E., Zinigrad, E., Asraf L., Gnanaraj J.S., & Kim H.-J. Design of electrolyte solutions for Li and Li-ion batteries: a review. *Electrochim. Acta* **50**, 247-254 (2004).

[9]   Howell D. U.S. DOE Perspective on Lithium-ion Battery Safety. *Technical symposium: Safety considerations for EVs powered by Li-ion batteries* (2011).

[10]   Wen J.W., Yu Y. & Chen C.H. A Review on lithium-Ion batteries safety issues: Existing problems and possible solutions. *Mater. Express* **2**, 197-212 (2012).

[11]   Golubkov A.W., Fuchs D., Wagner J., Wiltsche H., Stangl C., Fauler G., Voitic G., Thaler A. & Hacker V. Thermal-runaway experiments on consumer Li-ion batteries with metal-oxide and olivin-type cathodes. *RSC Adv.* **4**, 3633-3642 (2014).

[12]   Wang Q.S., Jinhua Sun J.H. & Chu G.Q. Lithium ion battery fire and explosion. *Fire Safety Science-Proceedings of the Eighth International Symposium*, 375-382 (2005).

[13]   Linden D. & Reddy T.B. *Handbook of batteries*. Third Edition, McGraw-Hill.

[14]   Goodenough J.B. & Kim Y. Challenges for rechargeable batteries. *J. Power Sources* **196**, 6688-6694 (2011).

[15]   Aurbach D., Zinigrad E., Cohen Y. & Teller H. A Short review of failure mechanisms of lithium metal and lithiated graphite anodes in liquid electrolyte solutions. *Solid State Ionics* **148**, 405-416 (2002).

[16]   Park M. S., Ma S. B., Lee D. J., Im D. M., Doo S. G. & Yamamoto O., A highly reversible lithium metal anode. *Scientific Reports* **4**, 3815 (2014).

[17]   Tenhaeff W. E., Yu X., Hong K., Perry K. A. & Dudney N. J. Ionic transport across interfaces of solid glass and polymer electrolytes for lithium ion batteries. *J. Electrochem. Soc.* **158 (10)**, A1143-A1149 (2011).

[18]   Knauth P. Inorganic solid Li ion conductors: An overview, *Solid State Ionics* **180**, 911-916 (2009).

[19]   Kotobuki M., Kanamura K., Sato Y. & Yoshida T. Fabrication of all-solid-state lithium battery with lithium metal anode using Al_2O_3-added $Li_7La_3Zr_2O_{12}$ solid electrolyte, *J. Power Sources* **196**, 7750-7754 (2011).

[20]   Luntz A.C., Voss J. & Reuter K. Interfacial challenges in solid-state Li ion batteries. *J. Phys. Chem. Lett.* **6**, 4599-4604 (2015).

[21]   Fergus J.W. Ceramic and polymeric solid electrolytes for lithium-ion batteries, *J. Power Sources* **195**, 4554-4569 (2010).

[22]   Song J.Y., Wang Y.Y. & Wan C.C. Review of gel-type polymer electrolytes for lithium-ion batteries. *J. Power Sources* 77. 183-197 (1999).

[23]   Rahman M.A., Wang X.J. & Wen C. A review of high energy density lithium-air battery technology. *J. Appl. Electrochem.* **44**, 5-22 (2014).

[24]   Jung H.-G., Hassoun J. & Park J.B. An improved high-performance lithium-air battery. *Nature Chem.* **4**, 579-585 (2012).

[25]   Asl N. M., Keith J., Lim C., Zhu, L. & Kim Y., Inorganic solid/organic liquid hybrid electrolyte for use in Li-ion battery, *Electrochim. Acta* **79**, 8-16 (2012).

[26]   Nakajima K., Katoh T., Inda Y. & Hoffman B. Lithium ion conductive glass ceramics: Properties and application in lithium metal batteries. *Symposium on Energy Storage beyond Lithium Ion* (2010).

[27]   Jeong E., Hong C., Tak Y., Nam S.C. & Cho S. Investigation of interfacial resistance between $LiCoO_2$ cathode and LiPON electrolyte in the thin film battery. *J. Power Sources* **159**, 223-226 (2006).

[28]   Takahashi K., Maekawa H. & Takamura H. Effects of intermediate layer on interfacial resistance for all-solid-state lithium batteries using lithium borohydride. *Solid State Ionics* **262**, 179-182 (2014)

[29]   Takahashi K., Hattori K., Yamazaki T. & Takada K. All-solid-state lithium battery with LiBH4 solid electrolyte. *J. Power Sources* **226**, 61-64 (2013)

[30]   Kim S., Hirayama M, Suzuki K. & Kanno R. Hetero-epitaxial growth of $Li_{0.17}La_{0.61}TiO_3$ solid electrolyte on $LiMn_2O_4$ electrode for all solid-state batteries. *Solid State Ionics* **262**, 578-581 (2014).

[31]   Takada K. Interfacial nano-architectonics for solid-state lithium batteries. *Langmuir* **29**, 7538-7541 (2013).

[32]   Zheng G.Y., Lee S.W., Liang Z., Lee H.-W., Yan K., Yao H.B., Wang H.T., Li W.Y., Chu S. & Cui. Y. Interconnected hollow carbon nanospheres for stable lithium metal anodes. *Nature Nanotech.* **9**, 618-623 (2014).

[33]   Fenton D.E., Parker J.M. &Wright P.V. Complexes of alkali metal ions with poly (ethylene oxide). *Polym.* **14**, 589, (1973).

[34]   Agrawal R.C. & Pandey G.P. Solid polymer electrolytes: materials designing and all-solid-state battery applications: An overview. *J. Phys. D: Appl. Phys.* **41**, 1-18 (2008).

[35]   Wright P.V. Electrical conductivity in ionic complexes of poly (ethylene oxide). *Br. Polym. J.* **7**, 319-327 (1975).

[36]   Armand M. The history of polymer electrolytes. *Solid State Ionics* **69**, 309-319 (1994).

[37]   Webber A. Conductivity and viscosity of solutions of $LiCF_3SO_3$, $Li(CF_3SO_2)_2N$ and their mixtures. *J. Electrochem. Soc.* **138 (9)**, 2586-2590 (1991).

[38]   Li W. & J. R. Dahn J.R. Lithium-ion cells with aqueous electrolytes. J. *Electrochem. Soc.* **142**, 1742-1746 (1995).

[39]   Wessells C., Ruff R. & Huggins R.A. & Cui.Y. Investigations of the electrochemical stability of aqueous electrolytes for lithium battery applications. *Electrochem. Solid-State Lett.* **13 (5)**, A59-A61 (2010).

[40]   Younesi R., Veith G.M., Johansson P., Edström K. & Vegge T. Lithium salts for advanced lithium batteries: Li-metal, Li-O$_2$, and Li-S. *Energy Environ. Sci.* **8**, 1905-1922 (2015).

[41]   Zhang S.S., Xu K. & Jow T.R. Study of LiBF4 as an electrolyte salt for a Li-ion battery. *J. Electrochem. Soc.* **149 (5)**, A586-A590 (2002).

[42]   Zhang S.S., Xu K. & Jow T.R. Low-temperature performance of Li-ion cells with a LiBF$_4$-based electrolyte. *J. Solid State Electrochem.* **7**, 147-151 (2003).

[43]   Xu K., Zhang S.S., T. Jow T.R., Xu W. & Angell C.A. LiBOB as salt for lithium-ion batteries: A possible solution for high temperature operation. *Electrochem. Solid-State Lett.* **5**, A26-A29 (2002).

[44]   Täubert C., Fleischhammer M., Wohlfahrt-Mehrens M., Wietelmann U. & Buhrmester T. LiBOB as electrolyte salt or additive for lithium-ion batteries based on LiNi$_{0.8}$Co$_{0.15}$Al$_{0.05}$O$_2$/graphite. *J. Electrochem. Soc.* **157 (6)**, A721-A728 (2010).

[45]   Suo L.M., Borodin O., Gao T., Olguin M., Ho J., Fan X.L., Luo C., Wang C.S. & Xu K. "Water-in-salt" electrolyte enables high-voltage aqueous lithium-ion chemistries. *Science* **350**, 938-943 (2015).

[46]   Tenhaeff W.E., Perry K.A. & Dudney N.J. Impedance characterization of Li ion transport at the interface between laminated ceramic and polymeric electrolytes, *J. Electrochem. Soc.* **159**, A2118-A2123 (2012).

[47]   Ye H., Huang J., Xu J.J. Khalfan A. & Greenbaum S.G. Li ion conducting polymer gel electrolytes based on ionic liquid/PVDF-HFP blends. *J. Electrochem. Soc.* **154** (11), A1048-A1057 (2007).

[48]   Murmann P., Niehoff P., Schmitz R., Nowak S., Gores H., Ignatiev N., Sartori P., Winter M. & Schmitz R. Lithium-cyclo-difluoromethane-1,1- bis(sulfonyl)imide as a stabilizing electrolyte additive for improved high voltage applications in lithium-ion batteries. *Phys. Chem. Chem. Phys.* **17**, 9352-9358 (2015).

[49]   Croce F., Appetecchi G. B., Persi L. & Scrosati B. Nanocomposite polymer electrolytes for lithium batteries, *Nature* **394**, 456-458 (1998).

[50]   Stephan A.M. & Nahm K. S., Review on composite polymer electrolytes for lithium batteries, *Polym. (Guildf)* **47**, 5952-5964 (2006).

[51]   Devaux D., Bouchet R., Glé D. & Denoyel R. Mechanism of ion transport in PEO/LiTFSI complexes: Effect of temperature, molecular weight and end groups. *Solid State Ionics* **227**, 119-127 (2012).

[52]   Pendzig P., Dieterich W. & Nitzan A. Monte Carlo study of diffusion in polymer electrolytes. *J. Non-Cryst. Solids* **235-237**, 748-752 (1998).

[53]   Bruce P.G. Structure and electrochemistry of polymer electrolytes. *Electrochim. Acta* **40**, 2077-2085 (1995).

[54]   Li Q., Itoh T., Imanishi N., Hirano A., Takeda Y., Yamamoto O. All solid lithium polymer batteries with a novel composite polymer electrolyte. *Solid State Ionics* **159**, 97-109 (2003).

[55]   Vallée A., Besner S. & Prud'homme J. Comparative study of poly (ethylene oxide) electrolytes made with $LiN(CF_3SO_3)_2$, $LiCF_3SO_3$, and $LiClO_4$: thermal properties and conductivity behavior. *Electrochim. Acta* **37**, 1579-1583 (1992).

[56]   MacGlashan G.S., Andreev Y.G. & Bruce P.G. Structure of the polymer electrolyte poly (ethylene oxide)$_6$: $LiAsF_6$. *Nature* **398**, 792-794 (1999).

[57]   Andreev Y.G. & Bruce P.G. Polymer electrolyte structure and its implications. *Electrochim. Acta* **45**, 1417-1423 (2000).

[58]   Gadjourova Z., Andreev Y.G., Tunstall D.P. & Bruce P.G. Ionic conductivity in crystalline polymer electrolytes. *Nature* **412**, 520-523 (2001).

[59]   Xu Q.Z. & Wan G.X. Rechargeable Li/LiMn2O4 batteries with a polymeric solid electrolyte. *J. Power Sources* **41**, 315-320 (1993).

[60]   Pehlivan I.B., Granqvist C.G., Marsal R., Georén P. & Niklasson G.A. [PEI-SiO$_2$]: [LiTFSI] nanocomposite polymer electrolytes: Ion conduction and optical properties. *Sol. Energy Mater. Sol. Cells* **98**, 465-471 (2012).

[61]   Ramesh S. & Ng H.M.   An investigation on PAN-PVC-LiTFSI based polymer electrolytes system. *Solid State Ionics* **192**, 2-5 (2011).

[62]   Rajendran S., Babu R.S. & Sivakumar P. Investigations on PVC/PAN composite polymer electrolytes. *J. Membrane Sci.* **315**, 67-73 (2008).

[63]   Wang Y.J., Pan Y., Wang L., Pang M. J, & Chen L.S. Characterization of (PEO) LiClO$_4$-Li$_{1.3}$Al$_{0.3}$Ti$_{1.7}$(PO$_4$)$_3$ composite polymer electrolytes with different molecular weights of PEO. *J. Appl. Polym. Sci.* **102**, 4269-4275 (2006).

[64]   Geiculescu O. E., Yang J., Zhou S., Shafer G., Xie Y., Albright J., Creager S. E., Pennington W. T. & DesMarteau D. D. Solid polymer electrolytes from polyanionic lithium salts based on the LiTFSI Anion Structure. *J. Electrochem. Soc.* **151 (9)**, A1363-A1368 (2004).

[65]   Ding L.M. Lithium ion conducting polymer electrolytes based on alternating maleic anhydride copolymer with oligo-oxyethylene side chains. *Chin. J. Polym. Sci.* **14 (3)**, 240-247 (1996).

[66]   Niitani T., Shimada M., Kawamura K. & Kanamura K. Characteristics of new-type solid polymer electrolyte controlling nano-structure. *J. Power Sources* **146**, 386-390 (2005).

[67]   Lobitz P., Fiillbier H., Reiche A. & Illner J.C. Ionic conductivity in poly (ethylene oxide)-poly (alkylmethacrylate)-block copolymer mixtures with LiI. *Solid State Ionics* **58**, 41-48 (1992).

[68]   Sadoway D.R. Block and graft copolymer electrolytes for high-performance, solid-state, lithium batteries. *J. Power Sources* **129**, 1-3 (2004).

[69]   Snyder J.F., Carter R.H. & Wetzel E.D. Electrochemical and mechanical behavior in mechanically robust solid polymer electrolytes for use in multifunctional structural batteries. *Chem. Mater.* **19**, 3793-3801 (2007).

[70]   Hou W.-H., Chen C.-Y., Wang C.-C. & Huang Y.-H. The effect of different lithium salts on conductivity of comb-like polymer electrolyte with chelating functional group. *Electrochim. Acta* **48**, 679-690 (2003).

[71]   Cha E.H., Macfarlane D.R., Forsyth M. & Lee C.W. Ionic conductivity studies of polymeric electrolytes containing lithium salt with plasticizer. *Electrochim. Acta* **50**, 335-338 (2004).

[72]   Morita M., Fujisaki T., Yoshimoto N. & Ishikawa M. Ionic conductance behavior of polymeric composite solid electrolytes containing lithium aluminate. *Electrochim. Acta* **46**, 1565-1569 (2001).

[73]   Shin J.-H., Henderson W.A. & Passerini S. PEO-based polymer electrolytes with ionic liquids and their use in lithium metal-polymer electrolyte batteries. *J. Electrochem. Soc.* **152 (5)**, A978-A983 (2005).

[74]   Borodin O. & Smith G.D. Mechanism of ion transport in amorphous poly(ethylene oxide)/LiTFSI from molecular dynamics simulations. *Macromol.* **39**, 1620-1629 (2006).

[75]   Diddens D., Heuer A. & Borodin O. Understanding the Lithium transport within a Rouse-based model for a PEO/LiTFSI polymer electrolyte. *Macromol.* **43**, 2028-2036 (2010).

[76]   Weston J.E. & Steele B.C.H. Effects of preparation method on properties of lithium salt-poly(ethylene oxide) polymer electrolytes. *Solid State Ionics* **7**, 81-88 (1982).

[77]   Sørensen P.R. & Jacobsen T. Conductivity, charge transfer and transport number- An AC investigation of the polymer electrolyte LiSCN-poly (ethylene oxide). *Electrochim. Acta* **27 (12)**, 1671-1675 (1982).

[78]   MacCallum J.R., Smith M.J. & Vincent C.A. The effects of radiation-induced crosslinking on the conductance of LiClO$_4$-PEO electrolytes. *Solid State Ionics* **11**, 307-312 (1984).

[79]   Chiodelli G., Ferloni P., Magistris A.& Sanesi M. Ionic conduction and thermal properties of poly(ethylene oxide)- lithium tetrafluoroborate films. *Solid State Ionic* **28-30**, 1009-1013 (1988).

[80]   Fontanella J.J., Wintersgill M.C., Calame J.P., Smith M.K. & Andeen C.G. DSC and high pressure conductivity and electrical relaxation measurements in PPO and PPO complex with lithium salts. *Solid State Ionics* **18-19**, 253-257 (1986).

[81]   Kim D.-W., Ryoo B.-K., Park J.-K., Maeng K.-S.& Hwang T.-S. Study on the ionic conductivity and mobility of liquid polymer electrolytes containing lithium salts. *Polym. J.* **24 (6)**, 509-518 (1992).

[82]   Berthier C., Gorecki W., & Minier M. Microscopic investigation of ionic conductivity in alkali metal salts-polymer (ethylene oxide) adducts. *Solid State Ionic* **11**, 91-95 (1983).

[83]   Caruso T., Capoleoni S., Cazzanelli E., Agostino R.G., Villano P. & Passerini S. Characterization of PEO-lithium triflate polymer electrolytes: conductivity, DSC and Raman Investigations. *Ionics* **8**, 36-43 (2002).

[84]   Yang L.-Y., Wei D.-X., Xu M., Yao Y.-F. & Chen Q. Transferring lithium ions in nanochannels: A PEO/Li+ solid polymer electrolyte design. *Angew. Chem. Int. Ed.* **53**, 3631-3635 (2014).

[85]   Mohd Noor S.A.b., Ahmad A., Rahman M.Y.b.A. & Talib I. A. Solid polymeric electrolyte of poly (ethylene) oxide-50% epoxidized natural rubber-lithium triflate (PEO-ENR$_{50}$-LiCF$_3$SO$_3$). *Natural Sci.* **2**, 190-196 (2010).

[86]   Golodnitsky D., Strauss E., Peled E., & Greenbaumd S. Review-On order and disorder in polymer electrolytes. *J. Electrochem. Soc.* **162 (14)**, A2551-A2566 (2015).

[87]   Angell C. A. Fast ion motion in glassy and amorphous materials. *Solid State Ionics* **9 & 10**, 3-16 (1983).

[88]   Druger S.D., Nitzan A. & Rather M.A. Dynamic bond percolation theory: A microscopic model for diffusion in dynamically disordered systems. I. Definition and one-dimensional case. *J. Chem. Phy.* **79**, 3133 (1983).

[89]   Druger S.D., Rather M.A. & Nitzan A. Polymeric solid electrolytes: dynamic bond percolation and free volume models for diffusion. *Solid State Ionics* **9 & 10,** 1115-1120 (1983).

[90]   Trevey J.E., Gilsdorf J.R., Miller S.W. & Lee S.-H. Li$_2$S-Li$_2$O-P$_2$S$_5$ solid electrolyte for all-solid-state lithium batteries. Solid State Ionics 214, 25-30 (2012).

[91]   O'Callaghan M.P., Lynham D.R., Cussen E.J. & Chen G.Z. Structure and ionic-transport properties of lithium-containing garnets Li$_3$Ln$_3$Te$_2$O$_{12}$ (Ln = Y, Pr, Nd, Sm-Lu). *Chem. Mater.* **18**, 4681-4689 (2006).

[92]   Bates J.B., Dudney N.J., Gruzalski G.R., Zuhr R.A., Choudhury A. & Luck C.F. Electrical properties of amorphous lithium electrolyte thin films. *Solid State Ionics* **53-56**, 647-654 (1992).

[93]   Aono. H., Sugimoto E., Sadaoka Y., Imanaka N. & Adachi G.Y. Ionic conductivity of the lithium titanium phosphate ($Li_{1+x}M_xTi_{2-x}(PO_4)_3$, M = Al, Sc, Y, and La) systems. *J. Electrochem. Soc.* **136 (2)**, 590-591 (1989).

[94]   Xu X.X., Wen Z.Y., Yang X.L., Zhang J.C. & Gu Z.H. High lithium ion conductivity glass-ceramics in Li_2O-Al_2O_3-TiO_2-P_2O_5 from nanoscaled glassy powders by mechanical milling. *Solid State Ionics* **177**, 2611-2615 (2006).

[95]   Fu J. Superionic conductivity of glass-ceramics in the system Al_2O_3-TiO_2-P_2O_5. *Solid State Ionics* **96**, 195-200 (1997).

[96]   Chowdari B.V.R., Subba Rao G.V., Lee G.Y.H. XPS and ionic conductivity studies on Li_2O-Al_2O_3 (TiO_2 or GeO_2)-P_2O_5 glass-ceramics. *Solid State Ionics* **136-137**, 1067-1075 (2000).

[97]   Kosova N.V., Devyatkina E.T., Stepanov A.P. & Buzlukov A.L. Lithium conductivity and lithium diffusion in NASICON-type $Li_{1+x}Ti_{2-x}Al_x(PO_4)_3$ (x=0; 0.3) prepared by mechanical activation. *Ionics* **14**, 303-311 (2008).

[98]   Orliukas A.F., Šalkus T., Kežionis A., Dindune A., Kanepe Z., Ronis J., Venckutė V., Kazlauskienė V., Miškinis J. & Lukauskas A. Structure and broadband impedance spectroscopy of $Li_{1.3}Al_yY_{x-y}Ti_{1.7}(PO_4)_3$ (x=0.3; y=0.1, 0.2) solid electrolyte ceramics. *Solid State Ionics* **225**, 620-625 (2012).

[99]   Thokchom J.S., Gupta N. & Kumar B. Superionic conductivity in a lithium aluminum germanium phosphate glass-ceramic. *J. Electrochem. Soc.* **155 (12)**, A915-A920 (2008).

[100] Xu X.X., Wen Z.Y., Gu Z.H., Xu X.H. &Lin Z.X. Lithium ion conductive glass ceramics in the system $Li_{1.4}Al_{0.4}(Ge_{1-x}Ti_x)_{1.6}(PO_4)_3$ (x = 0-1.0). *Solid State Ionics* **171**, 207-213 (2004).

[101] Inaguma Y., Liquan C., Itoh M., Nakamura T., Uchida T., Ikuta H. & Wakihara M. High ionic conductivity in lithium lanthanum titanate. *Solid State Commun.* **86 (10)**, 689-693 (1993).

[102] Ban C.W & Choi G.M. The effect of sintering on the grain boundary conductivity of lithium lanthanum titanates. *Solid State Ionics* **140**, 285-292 (2001).

[103] Kotobukin M. & Kanamura K. Fabrication of all-solid-state battery using $Li_5La_3Ta_2O_{12}$ ceramic electrolyte. *Ceram. Int.* **39**, 6481-6487 (2013).

[104] Furusawa S.-I., Tabuchi H., TSugiyama T., Tao S. W. & Irvine J.T.S. Ionic conductivity of amorphous lithium lanthanum titanate thin film. *Solid State Ionics* **176**, 553-558 (2005).

[105] Thangadurai V. & Weppner W. $Li_6Al_2Ta_2O_{12}$ (A=Sr, Ba): Novel garnet-like oxides for fast lithium ion conduction. *Adv. Funct. Mater.* **15**, 107-112 (2005).

[106] Murugan R., Weppner W., Schmid-Beurmann P. &Thangadurai V. Structure and lithium ion conductivity of bismuth containing lithium garnets $Li_5La_3Bi_2O_{12}$ and $Li_6SrLa_2Bi_2O_{12}$. *Mat. Sci. Engg. B* **143**, 14-20 (2007).

[107] Awaka J., Kijima N., Takahashi Y., Hayakawa H. & Akimoto J. Synthesis and crystallographic studies of garnet-related lithium-ion conductors $Li_6CaLa_2Ta_2O_{12}$ and $Li_6BaLa_2Ta_2O_{12}$. *Solid State Ionics* **180**, 602-606 (2009).

[108] Murugan R., Thangadurai V. &Weppner W. Fast lithium ion conduction in garnet-type $Li_7La_3Zr_2O_{12}$. *Angew. Chem. Int. Ed.* **46**, 7778-7781 (2007).

[109] Shimonishi Y., Toda A., Zhang T., Atsushi Hirano A., Imanishi N., Yamamoto O. & Takeda Y. Synthesis of garnet-type $Li_{7-x}La_3Zr_2O_{12-1/2x}$ and its stability in aqueous solutions. *Solid State Ionics* **183**, 48-53 (2011).

[110]   Awaka J., Kijima N., Hayakawa H., Akimoto J. Synthesis and structure analysis of tetragonal $Li_7La_3Zr_2O_{12}$ with the garnet-related type structure. *J. Solid State Chem.* **182**, 2046-2052 (2009).

[111]   Rosenkiewitz N., Schuhmacher J., Bockmeyer M. & Deubener J. Nitrogen-free sol-gel synthesis of Al-substituted cubic garnet $Li_7La_3Zr_2O_{12}$ (LLZO). *J. Power Sources* **278**, 104-108 (2015).

[112]   Tan J.J. & Ashutosh Tiwari A. Synthesis of cubic phase $Li_7La_3Zr_2O_{12}$ electrolyte for solid-state lithium-ion batteries. *Electrochem. Solid-State Lett.* **15 (3)**, A37-A39 (2012).

[113]   Chen R.J., Huang M., Huang W.Z., Yang Shen Y., Lin Y.H. & Nan C.-W. Sol-gel derived Li-La-Zr-O thin films as solid electrolytes for lithium-ion batteries. *J. Mater. Chem. A* **2**, 13277-13282 (2014).

[114]   Robertson A.D., West A.R. & Ritchie A.G. Review of crystalline lithium-ion conductors suitable for high temperature battery applications. *Solid State Ionics* **104**, 1-11 (1997).

[115]   Thangadurai V. & Weppner W. Effect of sintering on the ionic conductivity of garnet-related structure $Li_5La_3Nb_2O_{12}$ and In- and K-doped $Li_5La_3Nb_2O_{12}$. *J. Solid State Chem.* **179**, 974-984 (2006).

[116]   Maekawa H., Tanaka R., Sato T., Fujimakia Y. & Yamamura T. Size-dependent ionic conductivity observed for ordered mesoporous alumina-LiI composite. *Solid State Ionics* **175**, 281-285 (2004).

[117]   Trevey J.E., Jung Y.S. & Lee S.-H. High lithium ion conducting Li_2S-GeS_2-P_2S_5 glass-ceramic solid electrolyte with sulfur additive for all solid-state lithium secondary batteries. *Electrochim. Acta* **56**, 4243-4247 (2011).

[118]   Machida N., Yoneda Y. & Shigematsu T. Mechano-chemical synthesis of lithium ion conducting materials in the system Li_2O-Li_2S-P_2S_5. *J. Jpn. Soc. Powder Powder Metall.* **51 (2)**, 91-97 (2004).

[119]   Tatsumisago M., Mizuno F. & Hayashi A. All-solid-state lithium secondary batteries using sulfide-based glass-ceramic electrolytes. *J. Power Sources* **159**, 193-199 (2006).

[120]   Lang B., Ziebarth B. & Elsässer C. Lithium ion conduction in $LiTi_2(PO_4)_3$ and related compounds based on the NASICON structure: A first-principles study. *Chem. Mater.* **27**, 5040-5048 (2015).

[121]   Monchak M., Hupfer T., Senyshyn A., Boysen H., Chernyshov D., Hansen T., Schell K.G., Bucharsky E.C., Hoffmann M.J. & Ehrenberg H. Lithium diffusion pathway in $Li_{1.3}Al_{0.3}Ti_{1.7}(PO_4)_3$ (LATP) superionic conductor. *Inorg. Chem.* **55**, 2941-2945 (2016).

[122]   Arbi K., Rojo J.M. & Sanz J. Lithium mobility in titanium based Nasicon $Li_{1+x}Ti_{2-x}Al_x(PO_4)_3$ and $LiTi_{2-x}Zr_x(PO_4)_3$ materials followed by NMR and impedance spectroscopy. *J. Euro. Ceram. Soc.* **27**, 4215-4218 (2007).

[123]   Cretin M. & Fabry P. Comparative study of lithium ion conductors in the system $Li_{1+x}Al_xA_{2-x}^{IV}$ $(PO4)_3$ with A^{IV}=Ti or Ge and $0 \leq x \leq 0.7$ for use as Li sensitive membranes. *J. Euro. Ceram. Soc.* **19**, 2931-2940 (1999).

[124]   Jackman S.D. & Cutler R.A. Stability of NaSICON-type $Li_{1.3}Al_{0.3}Ti_{1.7}P_3O_{12}$ in aqueous solutions. *J. Power Sources* **230**, 251-260 (2013).

[125]   Jackman S.D. & Cutler R.A. Effect of microcracking on ionic conductivity in LATP. *J. Power Sources* **218**, 65-72 (2012).

[126]   Kotobuki M., Koishi K. Preparation of $Li_{1.5}Al_{0.5}Ti_{1.5}(PO_4)_3$ solid electrolyte via a sol-gel route using various Al sources. *Ceram. Int.* **39**, 4645-4649 (2013).

138

[127]   Duluard S., Paillassa A., Puech L., Vinatier P., Turq V., Rozier P., Lenormand P., Taberna P.-L., Simon P. & Ansart F. Lithium conducting solid electrolyte $Li_{1.3}Al_{0.3}Ti_{1.7}(PO_4)_3$ obtained via solution chemistry. *J. Euro. Ceram. Soc.* **33**, 1145-1153 (2013).

[128]   Huang L.Z., Wen Z. Y., Wu M.F., Wu X.W., Liu Y. & Wang X.Y. Electrochemical properties of $Li_{1.4}Al_{0.4}Ti_{1.6}(PO_4)_3$ synthesized by a co-precipitation method. *J. Power Sources* **196**, 6943-6946 (2011).

[129]   Schroeder M., Glatthaar S. & Binder J.R. Influence of spray granulation on the properties of wet chemically synthesized $Li_{1.3}Al_{0.3}Ti_{1.7}(PO_4)_3$ (LATP) powders. *Solid State Ionics* **201**, 49-53 (2011).

[130]   Jadhav H.S., Kalubarme R.S., Jang S.-Y., Jung K.-N., Shin K.-H. & Park G.-J. B_2O_3-added lithium aluminium germanium phosphate solid electrolyte for $Li-O_2$ rechargeable batteries. *Dalton Trans.* **43**, 11723-11727 (2014).

[131]   Leo C.J., Subba Rao G.V. & Chowdari B.V.R. Effect of MgO addition on the ionic conductivity of $LiGe_2(PO_4)_3$ ceramics. *Solid State Ionics* **159**, 357-367 (2003).

[132]   Leo. C.J., Chowdari B.V.R., Subba Rao G.V. & Souquet J.L. Lithium conducting glass ceramic with Nasicon structure. *Mater. Res. Bull.* **34**, 1419-1430 (2002).

[133]   Yamamoto H., Tabuchi M., Takeuchi T., Kageyama H. & Nakamura O. Ionic conductivity enhancement in $LiGe_2(PO_4)_3$ solid electrolyte. *J. Power Sources* **68**, 397-401 (1997).

[134]   Santosh KC, Longo R.C., Xiong K. & Cho K. Point defects in garnet-type solid electrolyte ($c-Li_7La_3Zr_2O_{12}$) for Li-ion batteries. *Solid State Ionics* **261**, 100-105 (2014).

[135]   Kotobuki M., Munakata H., Kanamura K., Sato Y. & Yoshida T. Compatibility of $Li_7La_3Zr_2O_{12}$ solid electrolyte to all-solid-state battery using Li metal anode. *J. Electrochem. Soc.* **157 (10)**, A1076-A1079 (2010).

[136]   Jin Y. & McGinn P. J. $Li_7La_3Zr_2O_{12}$ electrolyte stability in air and fabrication of a Li/$Li_7La_3Zr_2O_{12}$/$Cu_{0.1}V_2O_5$ solid-state battery. *J. Power Sources* **39**, 326-3312 (2013).

[137]   Sakamoto J., Rangasamy E., Kim H., Kim Y.S. & Wolfenstine J. Synthesis of nano-scale fast ion conducting cubic $Li_7La_3Zr_2O_{12}$. *Nanotechnology* **24**, 1-8 (2013).

[138]   Kokal I., Somer M., Notten P.H.L. & Hintzen H.T. Sol-gel synthesis and lithium ion conductivity of $Li_7La_3Zr_2O_{12}$ with garnet-related type structure. *Solid State Ionics* **185**, 42-46 (2011).

[139]   Bohnke O. The fast lithium-ion conducting oxides $Li_{3x}La_{2/3-x}TiO_3$ from fundamentals to application. *Solid State Ionics* **179**, 9-15 (2008).

[140]   Liao C.-L., Wen C.-H. & Fung K.-Z. The stability between perovskite $La_{2/3-x}Li_{3x\square1/3-2x}TiO_3$ (x = 0.3) electrolyte and LiMmOn (M = Mn, Ni and Co) cathodes. *J. Alloy. Compd.* **432**, L22-L25 (2007).

[141]   Mei A., Wang X.-L., Lan J.-L., Feng Y.-C., Geng H.-X., Lin Y.-H. & Nan C.-W. Role of amorphous boundary layer in enhancing ionic conductivity of lithium-lanthanum-titanate electrolyte. *Electrochim. Acta* **55**, 2958-2963(2010).

[142]   Deng Y, Shang S.-J., Mei A, Lin Y.-H., Liu L.-Y. & Nan. C.-W. The preparation and conductivity properties of $Li_{0.5}La_{0.5}TiO_3$/inactive second phase composites. *J. Alloy. Compd.* **472**, 456-460 (2009).

[143]   Ohtomo T., Hayashi, A., Tatsumisago M. & Kawamoto K. All-solid-state batteries with $Li_2O-Li_2S-P_2S_5$ glass electrolytes synthesized by two-step mechanical milling. *J. Solid State Electrochem.* **17**, 2551-2557 (2013).

[144]   [144] Heitjans P. & Indris S. Diffusion and ionic conduction in nanocrystalline ceramics. *J. Phys.: Condens. Matter* **15**, R1257-R1289 (2003).

[145]   [145] Aono H. & Sugimoto E. Ionic conductivity and sinterability of lithium titanium phosphate system. *Solid State Ionics* **40-41**, 38-42 (1990).

[146]   [146] Arbi K., Lazarraga M. G., Ben Hassen Chehimi D., Ayadi-Trabelsi M., Rojo J. M. & Sanz J. *Chem. Mater.* **16**, 255-262 (2004).

[147]   [147] Danilov D., Niessen R. A. H. & Nottena P. H. L. Modeling All-Solid-State Li-Ion Batteries. *J. Electrochem. Soc* **158 (3)**, A215-A222 (2011).

[148]   Jiang Z., Carroll B. & Abraham K.M. Studies of some poly(vinylidene fluoride) electrolytes. *Electrochim. Acta* **42**, 2667-2677 (1997).

[149]   Deepa M., Sharma N., Agnihotry S.A., Singh S., Lal T. & Chandra R. Conductivity and viscosity of liquid and gel electrolytes based on $LiClO_4$, $LiN(CF_3SO_2)_2$ and PMMA. *Solid State Ionics* **152-153**, 253-258 (2002).

[150]   Kim C.S. & Oh S.M. Spectroscopic and electrochemical studies of PMMA-based gel polymer electrolytes modified with interpenetrating networks. *J. Power Sources* **109**, 98-104 (2002).

[151]   Stephan A.M., Nahm K.S., Kulandainathan M.A., Ravi G. & Wilson J. Poly(vinylidene fluoride-hexafluoropropylene) (PVdF-HFP) based composite electrolytes for lithium batteries. *Euro. Polym. J.* **42**, 1728-1734 (2006).

[152] Cao J.-H., Zhu B.-K. & Xu Y.-Y. Structure and ionic conductivity of porous polymer electrolytes based on PVDF-HFP copolymer membranes. *J. Memb. Sci.* **281**, 446-453 (2006).

[153] Passerini S., Rosolen J.M. & Scrosati B. Plasticized carbon electrodes of interest for lithium rocking chair batteries. *J. Power Sources* **45**, 333-341 (1993).

[154] Choe H. S., Giaccai J., Alamgir M. & Abraham K. M. Preparation and characterization of poly(vinyl sulfone)- and poly(vinylidene fluoride)- based electrolytes. *Electrochim. Acta* **40** (**13-14**), 2289-2293 (1995).

[155] Muniyandi N., Kalaiselvi N., Periyasamy P., Thirunakaran R., Ramesh babu B., Gopukumar S., Premkumar T., Renganathan N.G. & Raghavan M. Optimization of PVdF-based polymer electroltyes. *J. Power Sources* **96**, 14-19 (2001).

[156] Stephan A.M., Kumar S.G., Renganathan N.G. & Kulandainathan M.A. Characterization of poly(vinylidene fluoride-hexafluoropropylene) (PVdF-HFP) electrolytes complexed with different lithium salts. *Euro. Polym. J.* **41**, 15-21 (2005).

[157] Deepa M., Sharma N., Agnihotry S.A., Chandra R. & Sekhon S.S. Effect of mixed salts on the properties of gel polymeric electrolytes. *Solid State Ionics* **148**, 451-455 (2002).

[158] Xu W. & Angell C.A. Polymer electrolytes from plasticized polyMOBs and their gel forms. *Electrochim. Acta* **48**, 2029-2035 (2003).

[159] Periasamy P., Tatsumi K., Shikano M., Fujieda T., Sakai T., Saito Y., Mizuhata M., Kajinami A. & Deki S. An electrochemical investigation on polyvinylidene fluoride-based gel polymer electrolytes. *Solid State Ionics* **126**, 285-292 (1999).

[160] Wang H.P., Huang H.T. & Wunder S.L. Novel microporous poly(vinylidene fluoride) blend electrolytes for lithium-ion batteries. *J. Electrochem. Soc.* **147 (8)**, 2853-2861 (2000).

[161]   Ferrari S., Quartarone E., Mustarelli P., Magistris A., Fagnoni M., Protti S., Gerbaldi C. & Spinella A. Lithium ion conducting PVdF-HFP composite gel electrolytes based on N-methoxyethyl-N-methylpyrrolidinium bis(trifluoromethanesulfonyl)-imide ionic liquid. *J. Power Sources* **195**, 559-566 (2010).

[162]   Lee K.-H., Jung-Ki Park J.-K. & Kim W.-J. Preparation and ion conductivities of the plasticized polymer electrolytes based on the poly(acrylonitrileco-lithium methacrylate). *J. Polym. Sci.: Part B: Polym. Phy.* **37**, 247-252 (1999).

[163]   Croce, F. & Scrosati, B. Interfacial phenomena in polymer electrolyte cells: lithium passivation and cyclability. *J. Power Sources* **43**, 9-19 (1993).

[164]   Croce F., Persi L., Scrosati B., Serraino-Fiory F., Plichta E. & Hendrickson M.A. Role of the ceramic fillers in enhancing the transport properties of composite polymer electrolytes. *Electrochim. Acta* **46**, 2457-2461 (2001).

[165]   Wang C.X., Xia Y.Y., Koumoto K. & Sakai T. All solid-state Li/Li$_x$MnO$_2$ polymer battery using ceramic modified polymer electrolytes. *J. Electrochem. Soc.* **149**, A967-A972 (2002).

[166]   Xi J.Y., Miao S.J. & Tang X.Z. Selective transporting of lithium ion by shape selective molecular sieves ZSM-5 in PEO-based composite polymer electrolyte. *Macromol.* **37**, 8592-8598 (2004).

[167]   Weston J.E. & Steele B.C.H. Effects of inert fillers on the mechanical and electrochemical properties of lithium salt-poly (ethylene oxide) polymer electrolytes. *Solid State Ionics* **7**, 75-79 (1982).

[168]   Croce F., Settimi L. & Scrosati B. Superacid ZrO2-added, composite polymer electrolytes with improved transport properties. *Electrochem. Communica.* **8**, 364-368 (2006).

[169]   Dey A., Karan S. & De S.K. Effect of nanoadditives on ionic conductivity of solid polymer electrolyte. *In. J. Pure & Appl. Phy.* **51**, 281-288 (2013).

[170]   Chu P.P. & Reddy M.J. Sm2O3 composite PEO solid polymer electrolyte. *J. Power Sources* **115**, 288-294 (2003).

[171]   Appetecchi G.B. & Passerini S. PEO-carbon composite lithium polymer electrolyte. *Electrochim. Acta* **45**, 2139-2145 (2000).

[172]   Yap Y.L., You A.H., Teo L.L. & Hanapei H. Inorganic filler sizes effect on ionic conductivity in polyethylene oxide (PEO) composite polymer electrolyte. *Int. J. Electrochem. Sci.* **8**, 2154-2163 (2013).

[173]   Vignarooban K., Dissanayake M.A.K.L., Albinsson I. & Mellander B.-E. Effect of TiO_2 nano-filler and EC plasticizer on electrical and thermal properties of poly(ethylene oxide) (PEO) based solid polymer electrolytes. *Solid State Ionics* **266**, 25-28 (2014).

[174]   Subramania A., Kalyana Sundaram N.T., Sathiya Priya A.R. & Vijaya Kumar G. Preparation of a novel composite micro-porous polymer electrolyte membrane for high performance Li-ion battery. *J. Memb. Sci.* **294**, 8-15 (2007).

[175]   Yang C.-M., Kim H.-S., Na B.-K., Kum K.-S. & Cho B.W. Gel-type polymer electrolytes with different types of ceramic fillers and lithium salts for lithium-ion polymer batteries. *J. Power Sources* **156***, 74-580 (2006).

[176]   Miao R.Y., Liu B., Zhu Z.Z., Liu Y., Li J.L., Wang X.D. & Li Q.F. PVDF-HFP-based porous polymer electrolyte membranes for lithium-ion batteries. *J. Power Sources* **184**, 420-426 (2008).

[177]   Appetecchi. G.B., Croce F., Hassoun J., Scrosati B., Salomon M. & Cassel F. Hot pressed, dry, composite, PEO-based electrolyte membranes. I. Ionic conductivity characterization. *J. Power Sources* **114**, 105-112 (2003).

[178]   Kumar B., Scanlon L., Marsh R., Mason R., Higgins R. & Baldwin R. Structural evolution and conductivity of PEO:LiBF$_4$-MgO composite electrolytes. *Electrochim. Acta* **46**, 1515-1521 (2001).

[179]   Wang Y.-J. & Pan Y. Li$_{1.3}$Al$_{0.3}$Ti$_{1.7}$(PO$_4$)$_3$ filler effect on (PEO)LiClO$_4$ solid polymer electrolyte. *J. Polym. Sci.: Part B: Polym. Phy.* **43**, 743-751 (2005).

[180]   Chung S.H., Wang Y., Persi L., Croce F., Greenbaum S.G., Scrosati B. & Plichta E. Enhancement of ion transport in polymer electrolytes by addition of nanoscale inorganic oxides. *J. Power Sources* **97-98**, 644-648 (2001).

[181]   Wieczorek W., Stevens J.R. & Florjańczyk Z. Composite polyether based solid electrolytes. The Lewis acid-base approach. *Solid State Ionics* **85**, 67-72(1996).

[182]   Kumar B. & Scanlon L.G. Polymer-ceramic composite electrolytes. *J. Power Sources* **52**, 261-268 (1994).

[183]   Borghini M.C., Mastragostino M., Passerini S. & Scrosati B. Electrochemical properties of polyethylene oxide-Li[(CF$_3$SO$_2$)$_2$N]-amma-LiAlO$_2$ composite polymer electrolytes. *J. Electrochem. Soc.* **142 (7)**, 2118-2121 (1995).

[184]   Best A.S., Ferry A., MacFarlane D.R. & Forsyt M. Conductivity in amorphous polyether nanocomposite material. *Solid State Ionics* **126**, 269-276 (1999).

[185]   Johansson P., Ratner M.A. & Shriver F. The Influence of inert oxide fillers on poly(ethylene oxide) and amorphous poly(ethylene oxide) based polymer electrolytes. *J. Phys. Chem. B.* **105**, 9016-9021 (2001).

[186]   MacCallum, J.R. & Seth, S. Conductivity of poly(ethylene oxide)/silica composite films containing lithium trifluorosulphonate. *Euro. Polym. J.* **36**, 2337-2341 (2000).

[187]   Syzdek J.S., Armand M.B., Falkowski P., Gizowska M., Karłowicz M., Łukaszuk Ł., Marcinek M.Ł., Zalewska A, Szafran M., Masquelier C., Tarascon J.M., Wieczorek W.G. & Zukowska Z.G. Reversed phase composite polymeric electrolytes based on poly(oxyethylene). *Chem. Mater.* **23**, 1785-1797 (2011).

[188]   Vorrey S. & Teeters D. Study of the ion conduction of polymer electrolytes confined in micro and nanopores. *Electrochim. Acta* **48**, 2137-2141 (2003).

[189]   Abudakka M., Decker D.S., Sutherlin L.T., DTeeters D. Ceramic/polymer interpenetrating networks exhibiting increased ionic conductivity with temperature control of ion conduction for thermal runaway protection. *Int. J. Hydro. Energy* **39**, 2988-2996 (2014).

[190]   Syzdek J., Armand M., Gizowska M., Marcinek M., Sasim E., Szafran M. & Wieczorek W. Ceramic-in-polymer versus polymer-in-ceramic polymeric electrolytes: A novel approach. *J. Power Sources* **194**, 66-72 (2009).

[191]   Abe T., Ohtsuka M., Sagane F., Iriyama Y. & Ogumi Z. Lithium ion transfer at the interface between lithium-ion-conductive solid crystalline electrolyte and polymer electrolyte. *J. Electrochem. Soc.* **151(11)**, A1950-A1953 (2004).

[192]   Morimoto H., Awano H., Terashima J., Shindo Y., Nakanishi S., Ito N., Ishikawa K. & Tobishima S. preparation of lithium ion conducting solid electrolyte of NASICON-type $Li_{1+x}Al_xTi_{2-x}(PO_4)_3$ (x = 0.3) obtained by using the mechanochemical method and its application as surface modification materials of $LiCoO_2$ cathode for lithium cell . *J. Power Sources* **240**, 636-643 (2013).

[193] Xu X.X., Wen Z.Y., Wu J.G. & Yang X.L. Preparation and electrical properties of NASICON-type structured $Li_{1.4}Al_{0.4}Ti_{1.6}(PO_4)_3$ glass-ceramics by the citric acid-assisted sol-gel method. *Solid State Ionics* **178**, 29-34 (2007).

[194] Ratnalnuonr B.V., Smart M.C. & Surampudi S. Electrochemiad impedance spectroscopy and its applications to lithium ion cells. *Battery Conference on Applications and Advances 17th Annual*, 273-277 (2002).

[195] Zhang S.S., Xu K. & Jow T.R. Electrochemical impedance study on the low temperature of Li-ion batteries. *Electrochim. Acta* **49**, 1057-1061 (2004).

[196] Dhirde A.M., Dale N.V., Salehfar H., Mann M.D. & Han T.-H. Equivalent electric circuit modeling and performance analysis of a PEM fuel cell stack using impedance spectroscopy. *IEEE T. Energy Conv.* **25 (3)**, 778-796 (2010).

[197] Nielsen J. & Hjelm J. Impedance of SOFC electrodes: A review and a comprehensive case study on the impedance of LSM: YSZ cathodes. *Electrochim. Acta* **115**, 31-45 (2014).

[198] Osaka T., Momma T., Mukoyama D. & Nara H. Proposal of novel equivalent circuit for electrochemical impedance analysis of commercially available lithium ion battery. *J. Power Sources* **205**, 483-486 (2012).

[199] Bucharsky E.C., Schell K.G., Hintennach A. & Hoffmann M.J. Preparation and characterization of sol-gel derived high lithium ion conductive NZP-type ceramics $Li_{1+x}Al_xTi_{2-x}(PO_4)_3$. *Solid State Ionics* **274**, 77-82 (2015).

[200] Kuratomi J., Iguchi T., Bando T., Aihara Y., Ono T. & Kuwana K. Development of solid polymer lithium secondary batteries. *J. Power Sources* **97-98**, 801-803 (2001).

[201] Munshi M.Z.A., Owens B.B. & Nguyen S. Measurement of Li^+ ion transport numbers in poly (ethylene oxide) - LiX complexes. *Polym. J.* **20 (7)**, 597-602 (1988).

[202]   Evans J. & Vincent C.A. Electrochemical measurement of transference numbers in polymer Electrolytes. *Polym.* **28**, 2324-2328 (1987).

[203]   Ghosh A., Wang C.S. & Kofinasb P. Block copolymer solid battery electrolyte with high Li-ion transference number. *J. Electrochem. Soc.* **157(7)**, A846-A849 (2010).

[204]   Julien C.M., Mauger A., Zaghib K. & Groult H. Comparative issues of cathode materials for Li-ion batteries. *Inorganics* **2**, 132-154 (2014).

[205]   Pinson M.B. & Bazant M.Z. Theory of SEI formation in rechargeable batteries: Capacity fade, accelerated aging and lifetime prediction. *J. Electrochem. Soc.* **160 (2)**, A243-A250 (2013).

Vita

Wei Liu received his Bachelor of Science degree in Thermal Energy and Power Engineering from Chongqing University (CQU) in June 2006. Following graduation, he was admitted to the Institute of Engineering Thermo-Physic at CQU with fellowship. He finished his research work for Master of Science degree in Transport Phenomena Laboratory with Professor Qiang Liao in March 2009. After graduation, he worked in China Nuclear Power Engineering Company as an engineer for 2 years. He was admitted to the PhD program in Syracuse University and joined Combustion & Energy Research Laborator (COMER) with Dr. Jeongmin Ahn. Wei Liu completed his research work for the Doctor of Philosophy degree in April 2016.